

1 LEVERAGING MULTI-MESSENGER ASTROPHYSICS FOR DARK MATTER SEARCHES

By

Daniel Nicholas Salazar-Gallegos

A DISSERTATION

Submitted to
Michigan State University
in partial fulfillment of the requirements
for the degree of

Physics—Doctor of Philosophy
Computational Mathematics in Science and Engineering—Dual Major

Today

ABSTRACT

3 I did Dark Matter with HAWC and IceCube. I also used Graph Neural Networks

⁴ Copyright by

⁵ DANIEL NICHOLAS SALAZAR-GALLEGOS

⁶ Today

ACKNOWLEDGMENTS

8 I love my friends. Thanks to everyone that helped me figure this out. Amazing thanks to the people
9 at LANL who supported me. Eames, etc Dinner Parties Jenny and her child Kaydince Kirsten, Pat,
10 Andrea Family. You're so far but so critical to my formation. Unconditional love. Roommate

TABLE OF CONTENTS

12	LIST OF TABLES	vii
13	LIST OF FIGURES	viii
14	LIST OF ABBREVIATIONS	xiv
15	CHAPTER 1 INTRODUCTION	1
16	CHAPTER 2 DARK MATTER IN THE COSMOS	2
17	2.1 Introduction	2
18	2.2 Dark Matter Basics	3
19	2.3 Evidence for Dark Matter	4
20	2.4 Searching for Dark Matter: Particle DM	11
21	2.5 Sources for Indirect Dark Matter Searches	16
22	2.6 Multi-Messenger Dark Matter	18
23	CHAPTER 3 MULTIMESSENGER ASTROPHYSICS: DETECTING HIGH EN-	
24	ERGY NEUTRAL MESSENGERS	21
25	3.1 Introduction	21
26	3.2 Charged Particles in a Medium	21
27	3.3 Photons (γ)	22
28	3.4 Neutrinos (ν)	22
29	3.5 Opportunities to Combine for Dark Matter	22
30	CHAPTER 4 HIGH ALTITUDE WATER CHERENKOV (HAWC) OBSERVATORY .	24
31	4.1 The Detector	24
32	4.2 Events Reconstruction and Data Acquisition	24
33	4.3 Remote Monitoring	24
34	CHAPTER 5 ICECUBE NEUTRINO OBSERVATORY	25
35	5.1 The Detector	25
36	5.2 Events Reconstruction and Data Acquisition	25
37	5.3 Northern Test Site	25
38	CHAPTER 6 GLORY DUCK: MULTI-WAVELENGTH SEARCH FOR DARK MATT-	
39	TER ANNIHILATION TOWARDS DWARF SPHEROIDAL GALAX-	
40	IES	26
41	6.1 Introduction	26
42	6.2 Dataset and Background	28
43	6.3 Analysis	29
44	6.4 Likelihood Methods	34
45	6.5 HAWC Results	40
46	6.6 Glory Duck Combined Results	43
47	6.7 HAWC Systematics	48

48	6.8 <i>J</i> -factor distributions	49
49	6.9 Discussion and Conclusions	55
50	CHAPTER 7 MULTITHREADING HAWC ANALYSES FOR DARK MATTER	
51	SEARCHES	59
52	7.1 Introduction	59
53	7.2 Dataset and Background	59
54	7.3 Analysis	60
55	7.4 Likelihood Methods	65
56	7.5 Computational Methods: Multithreading	65
57	CHAPTER 8 HEAVY DARK MATTER ANNIHILATION SEARCH WITH ICE-	
58	CUBE'S NORTH SKY TRACK DATA	72
59	CHAPTER 9 NU DUCK	73
60	APPENDIX A MULTI-EXPERIMENT SUPPLEMENTARY FIGURES	74
61	APPENDIX B MULTITHREADING SUPPLEMENTARY FIGURES	75
62	B.1 <code>mpu_analysis.py</code>	76
63	BIBLIOGRAPHY	85

LIST OF TABLES

<p>65 Table 6.1 Summary of the relevant properties of the dSphs used in the present work. 66 Column 1 lists the dSphs. Columns 2 and 3 present their heliocentric distance 67 and galactic coordinates, respectively. Columns 4 and 5 report the J-factors of 68 each source given from the \mathcal{GS} and \mathcal{B} independent studies and their estimated 69 $\pm 1\sigma$ uncertainties. The values $\log_{10} J$ (\mathcal{GS} set) [45] correspond to the mean 70 J-factor values for a source extension truncated at the outermost observed star. 71 The values $\log_{10} J$ (\mathcal{B} set) [47] are provided for a source extension at the tidal 72 radius of each dSph. Bolded sources are within HAWC's field of view and 73 provided to the Glory Duck analysis.</p> 34
<p>74 Table 6.2 Summary of dSph observations by each experiment used in this work. A 75 ‘-’ indicates the experiment did not observe the dSph for this study. For 76 Fermi-LAT, the exposure at 1 GeV is given. For HAWC, $\Delta\theta$ is the absolute 77 difference between the source declination and HAWC latitude. HAWC is more 78 sensitive to sources with smaller $\Delta\theta$. For IACTs, we show the zenith angle 79 range, the total exposure, the energy range, the angular radius θ of the signal or 80 ON region, the ratio of exposures between the background-control (OFF) and 81 signal (ON) regions (τ), and the significance of gamma-ray excess in standard 82 deviations, σ.</p> 35
<p>83 Table 7.1 Summary of the relevant properties of the dSphs used in the present work. 84 Column 1 lists the dSphs. Columns 2 and 3 present their heliocentric distance 85 and galactic coordinates, respectively. Column 4 reports the J-factors of each 86 source given from the \mathcal{LS} studies and estimated $\pm 1\sigma$ uncertainties. The 87 values $\log_{10} J$ (\mathcal{LS} set) [65] correspond to the mean J-factor values for a 88 source extension truncated at 0.5°.</p> 63
<p>89 Table 7.2 Timing summaries for analyses for serial and multithreaded processes. M tasks 90 is the number of functional-parallel tasks ran for the computation. $T_{p,c}$ is a 91 single run time in hours:minutes:seconds for runs utilizing p cores/processors 92 and c threads. Runs are run interactively on the same computer to maximize 93 consistency. Empty entries are indicated with ‘-’. (.) entries are estimated 94 entries extrapolated from data earlier in the column.</p> 69
<p>95 Table 7.3 Speed up summaries for analyses for serial and multithreaded processes. M 96 tasks is the number of functional-parallel tasks ran for the computation. $S_{p,c}$ 97 is a single speedup comparison for runs utilizing p cores/processors and c 98 threads. $[\cdot]$ are the estimated speedups calculated from Tab. 7.2, Eq. (7.10), 99 and Eq. (7.5). Empty entries are indicated with ‘-’. (.) entries are calculated 100 from estimated entries from data in Tab. 7.2.</p> 71
<p>101 Proof I know how to include</p>	

LIST OF FIGURES

103	Figure 2.1	Rotation curve fit to NGC 6503 from [7]. Dashed line is the contribution 104 from visible matter. Dotted curves are from gas. Dash-dot curves are from 105 dark matter (DM). Solid line is the composite contribution from all matter 106 and DM sources. Data are indicated with bold dots with error bars. Data 107 agree strongly with a matter + DM composite prediction.	5
108	Figure 2.2	Light from distant galaxy is bent in unique ways depending on the distribution 109 of mass between the galaxy and Earth. Yellow dashed lines indicate where 110 the light would have gone if the matter were not present [8].	7
111	Figure 2.3	(left) Optical image of galactic cluster 1E0657-558. (right) X-ray image of the 112 cluster with redder meaning hotter and higher baryon density. (both) Green 113 contours are reconstruction of gravity contours from weak lensing. White 114 rings are the best fit mass maxima at 68.3%, 95.5%, and 99.7% confidence. 115 The matter maxima of the clusters are clearly separated from x-ray maxima. [9]	8
116	Figure 2.4	Plank CMB sky. Sky map features small variations in temperature in primor- 117 dial light. These anisotropies are used to make inferences about the universe's 118 energy budget and developmental history. [10]	9
119	Figure 2.5	Observed Cosmic Microwave Background power spectrum as a function of 120 multipole moment from Plank [10]. Blue line is best fit model from Λ CDM. 121 Red points and lines are data and error, respectively.	10
122	Figure 2.6	Predicted power spectra of CMB for different $\Omega_m h^2$ values for fixed baryon 123 density from [11]. (left) Low $\Omega_m h^2$ increases the prominence of first and 124 second peaks. (middle) $\Omega_m h^2$ is most similar to the observed power spectrum. 125 The second and third peaks are similar in height. (right) $\Omega_m h^2$ is large which 126 suppresses the first peak and raises the prominence of the third peak.	10
127	Figure 2.7	The Standard Model (SM) of particle physics. Figure taken from http://www.quantumdiaries.org/2014/03/14/the-standard-model-a-beautiful-but-flawed-theory/	12
130	Figure 2.8	Simplified Feynman diagram demonstrating with different ways DM can 131 interact with SM particles. The 'X's refer to the DM particles whereas the 132 SM refer to fundamental particles in the SM. The large circle in the center 133 indicates the vertex of interaction and is purposely left vague. The colored 134 arrows refer to different directions of time as well as their respective labels. 135 The arrows indicate the initial and final state of the DM -SM interaction in time.	13

136	Figure 2.9 A single jet event in ATLAS detector from 2017 [16]. Jet momentum was 137 observed to be 1.9 TeV. Missing transverse momentum was observed to be 138 1.9 TeV compared to the initial transverse momentum of the event was 0. 139 Implied MET is traced by a red dashed line in event display.	14
140	Figure 2.10 More detailed pseudo-Feynman diagram of particle cascade from dark matter 141 annihilation into 2 quarks. The quarks hadronize and down to stable particles 142 like γ or the anti-proton (p^-). Diagram pulled from ICRC 2021 presentation 143 on DM annihilation search [17].	15
144	Figure 2.11 Dark Matter (DM) decay spectrum for $b\bar{b}$ initial state and γ final state. Redder 145 spectra are for larger DM masses. Bluer spectra are light DM masses. x is a 146 unitless factor defined as the ratio of the mass of DM, m_χ , and the final state 147 particle energy E_γ . Figure from [19].	17
148	Figure 2.12 Different dark matter density profiles compared. Some models produce ex- 149 ceptionally large densities at small r [20].	18
150	Figure 2.13 The Milky Way Galaxy in photons (γ) and neutrinos (ν) [22]. The Galactic 151 center is at $l=0^\circ$ and is the brightest region in all panels. (top) An Optical 152 color image of the Milky Way galaxy seen from Earth. Clouds of gas and dust 153 obscure some light from stars. (2nd down) Integrated flux of γ -rays observed 154 by the Fermi-LAT telescope [23]. (middle) Expected neutrino emission 155 that corresponds with Fermi-LAT observations. (2nd up) Expected neutrino 156 emission profile after considering detector systematics of IceCube. (bottom) 157 Observed neutrino emission from region of the galactic plane. Substantial 158 neutrino emission was detected.	19
159	Figure 2.14 Dark Matter annihilation spectra for different final state particle and standard 160 model annihilation channels [24]. Photons (red), e^\pm (green), \bar{p} (blue), ν (black).	20
161	Figure 3.1 TODO: Show a nuclear reactor with cherenkov radiation[NEEDS A SOURCE][FACT 162 CHECK THIS]	22
163	Figure 3.2 TODO: absorption spectrum of liquid and solid water[NEEDS A SOURCE][FACT 164 CHECK THIS]	23

165	Figure 6.1 Sensitivities of five gamma-ray experiments compared to percentages of the 166 Crab nebula's emission and dark matter annihilation. Solid lines present 167 estimated sensitivities to power law spectra [FACT CHECK THIS]for each 168 experiment. Green lines are Fermi-LAT sensitivities where lighter green is 169 the sensitivity to the galactic center and dark green is its sensitivity to higher 170 declinations. Orange, red, and purple solid lines represent the MAGIC, HESS, 171 and VERITAS 50 hour sensitivities respectively. The maroon and brown lines 172 are the HAWC 1 year and 5 year sensitivities. Across four decades of gamma- 173 ray energy, these experiments have similar sensitivities on the order 10^{-12} 174 erg cm $^{-2}$ s $^{-1}$. The dotted lines are estimated dark matter fluxes assuming 175 $m_\chi = 5$ TeV DM annihilating to bottom quarks (red), tau leptons (blue), 176 and W bosons (green). Faded gray lines outline percentage flux of the Crab 177 nebula. Figure is an augmented version of [25]	27
178	Figure 6.2 Effect of Electroweak (EW) corrections on expected DM annihilation spec- 179 trum for $\chi\chi \rightarrow W^-W^+$. Solid lines are spectral models that consider EW 180 corrections. Dash-dot lines are spectral models without EW corrections. Red 181 lines are models for $M_\chi = 1$ TeV. Blue lines represent models for $M_\chi = 100$ 182 TeV. All models are sourced from the PPPC4DMID [44].	31
183	Figure 6.3 $\frac{dJ}{d\Omega}$ maps for Segue1 (top) and Coma Berenices (bottom). Origin is centered 184 on the specific dwarf spheroidal galaxies (dSph). X and Y axes are the 185 angular separation from the center of the dwarf. Plots of the remaining 11 186 dSph HAWC studied are linked in Fig. A.1.	33
187	Figure 6.4 Illustration of the combination technique showing a comparison between 188 $-2 \ln \lambda$ provided by four instruments (colored lines) from the observation 189 of the same dSph without any J nuisance and their sum, <i>i.e.</i> the resulting 190 combined likelihood (thin black line). According to the test statistics of 191 Equation (6.6), the intersection of the likelihood profiles with the line $-2 \ln \lambda$ 192 = 2.71 indicates the 95% C.L. upper limit on $\langle \sigma v \rangle$. The combined likelihood 193 (thin black line) shows a smaller value of upper limit on $\langle \sigma v \rangle$ than those 194 derived by individual instruments. We also show how the uncertainties on 195 the J factor effects the combined likelihood and degrade the upper limit on 196 $\langle \sigma v \rangle$ (thick black line). All likelihood profiles are normalized so that the global 197 minimum $\widehat{\langle \sigma v \rangle}$ is 0. We note that each profile depends on the observational 198 conditions in which a target object was observed. The sensitivity of a given 199 instrument can be degraded and the upper limits less constraining if the 200 observations are performed in non-optimal conditions such as a high zenith 201 angle or a short exposure time.	38
202	Figure 6.5 HAWC upper limits at 95% confidence level on $\langle \sigma v \rangle$ versus DM mass for 203 seven annihilation channels, using the set of J -factors from Ref. [53] The 204 solid line represents the observed combined limit. Dashed lines represent 205 limits from individual dSphs.	41

206	Figure 6.6 HAWC TS values for best fit $\langle\sigma v\rangle$ versus m_χ for seven SM annihilation channels with J factors from \mathcal{GS} . The solid black line shows the combined best fit TS values. The colored, dashed lines are the TS values for each of the 13 sources HAWC studied.	42
210	Figure 6.7 HAWC Brazil bands at 95% confidence level on $\langle\sigma v\rangle$ versus DM mass for seven annihilation channels with J -factors from \mathcal{GS} [53]. The solid line represents the combined limit from 13 dSphs. The dashed line is the expected limit. The green band is the 68% containment. The yellow band is the 95% containment.	43
215	Figure 6.8 Upper limits at 95% confidence level on $\langle\sigma v\rangle$ in function of the DM mass for eight annihilation channels, using the set of J factors from Ref. [53] (\mathcal{GS} set in Table 6.1). The black solid line represents the observed combined limit, the black dashed line is the median of the null hypothesis corresponding to the expected limit, while the green and yellow bands show the 68% and 95% containment bands. Combined upper limits for each individual detector are also indicated as solid, colored lines. The value of the thermal relic cross-section in function of the DM mass is given as the red dotted-dashed line [54].	44
224	Figure 6.9 Same as Fig. 6.8, using the set of J factors from Ref. [47, 55] (\mathcal{B} set in Table 6.1).	45
225	Figure 6.10 Comparisons of the combined limits at 95% confidence level for each of the eight annihilation channels when using the J factors from Ref. [53] (\mathcal{GS} set in Table 6.1), plain lines, and the J factor from Ref. [47, 55] (\mathcal{B} set in Table 6.1), dashed lines. The cross-section given by the thermal relic is also indicated [54].	47
229	Figure 6.11 Comparisons of the combined limits at 95% confidence level for a point source analysis and extended source using [53] \mathcal{GS} J-factor distributions and PPPC [44] annihilation spectra. Shown are the limits for Segue1 which will have the most significant impact on the combined limit. 6 of the 7 DM annihilation channels are shown. Solid lines are extended source studies. Dashed lines are point source studies. Overall, the extended source analysis improves the limit by a factor of 2.	49
236	Figure 6.12 Same as Fig. 6.11 on Coma Berenices. This dSph also contributes significantly to the limit. The limits are identical in this case.	50
238	Figure 6.13 Comparison of combined limits when correcting for HAWC's pointing systematic. All DM annihilation channels are shown. The solid black line is the ratio between published limit to the declination corrected limit. The blue solid line or "Combined_og" represented the limits computed for Glory Duck. The solid orange line or "Combined_ad" represented the limits computed after correcting for the pointing systematic.	51

244	Figure 6.14 Differential map of dJ/Ω from model built in Section 6.8.1 and profiles provided directly from authors. (Top) Differential from Segue1. (bottom) Differential from Coma Berenices. Note that their scales are not the same. Segue1 shows the deepest discrepancies which is congruent with its large uncertainties. Both models show anuli where unique models become apparent.	52
249	Figure 6.15 HAWC limits for Coma Berenices (top) and Segue1 (bottom) for two different map sets. Blue lines are limits calculated on maps with poor model representation. Orange lines are limits calculated on spatial profiles provided by the authors of [45]. Black line is the ratio of the poor spatial model limits to the corrected spatial models. The left y-axis measures $\langle\sigma v\rangle$ for the blue and orange lines. The right y-axis measures the ratio and is unitless.	53
255	Figure 6.16 Comparisons between the J -factors versus the angular radius for the computation of J factors from Ref. [53] (\mathcal{GS} set in Table 6.1) in blue and for the computation from Ref. [47, 55] (\mathcal{B} set in Tab. 6.1) in orange. The solid lines represent the central value of the J -factors while the shaded regions correspond to the 1σ standard deviation.	56
260	Figure 6.17 Comparisons between the J -factors versus the angular radius for the computation of J factors from Ref. [53] (\mathcal{GS} set in Tab. 6.1) in blue and for the computation from Ref. [47, 55] (\mathcal{B} set in Tab. 6.1) in orange. The solid lines represent the central value of the J -factors while the shaded regions correspond to the 1σ standard deviation.	57
265	Figure 7.1 Difference between spectral hypotheses from PPPC [44] and HDM [64]. Shown is the expected DM annihilation spectrum for $\chi\chi \rightarrow W^-W^+$. Solid lines are spectral models with EW corrections from the PPPC. Dash-dot lines are spectral models from HDM. Red lines are models for $M_\chi = 1$ TeV. Blue lines represent models for $M_\chi = 100$ TeV.	62
270	Figure 7.2 Photon spectra for $\chi\chi \rightarrow \gamma\gamma$ (left) and $\chi\chi \rightarrow ZZ$ (right) after gaussian convolution of line features. Both spectra have δ -features at photon energies equal to the DM mass. Bluer lines are annihilation spectra with lower DM mass. Redder lines are spectra from larger DM mass. All Spectral models are sourced from the Heavy Dark Matter models [64]. Axes are drawn roughly according to the energy sensitivity of HAWC.	63
276	Figure 7.3 $\frac{dJ}{d\Omega}$ maps for Coma Berenices, Draco, Segue1, and Sextans. Columns are divided for the $\pm 1\sigma$ uncertainties in $dJ/d\Omega$ around the mean value from \mathcal{LS} [65]. Origin is centered on the specific dwarf spheroidal galaxies (dSph). θ and ϕ axes are the angular separation from the center of the dwarf	64

280	Figure 7.4	Infographic on how jobs and DM computation was organized in Section 6.3. Jobs were built for each permutation of CHANS and SOURCES shown by the left block in the figure. Each job, which took on the order 2 hrs to compute, had the following work flow: 1. Import HAWC analysis software, 2 min to run. 2. Load HAWC count maps, 5 min to run. 3. Load HAWC energy and spatial resolutions, 4 min. 5. Load DM spatial source templates and spectral models, less than 1 s. 6. Perform likelihood fit on data and model, about 8 min per DM mass. 7. Write results to file, less than 1s.	66
288	Figure 7.5	Graphic of Gustafson parallel coding pattern. f_s is the fraction of a program, in time, spent on serial computation. f_p is the fraction of computing time that is parallelizable. T_p is the total time for a parallel program to run. T_1 is the total time for a parallel program to run if only 1 processor is allocated. P_N is the N -th processor where it's row is the computation the processor performs. The Gustafson pattern is most similar to what is implemented for this analysis. Figure is pulled from [67].	67
295	Figure 7.6	Task chart for one multi-threaded job developed for this project. Green blocks indicate a shared resource across the threads AND computation performed serially. Red blocks indicate functional parallel processing within each thread. 3 threads are represented here, yet many more can be employed during the full analysis. Jobs are defined by the SOURCE as these require unique maps to be loaded into the likelihood estimator. The m_χ , CHAN, and $\langle\sigma v\rangle$ variables are entered into the thread pool and allocated as evenly as possible across the threads.	69
303	Figure A.1	Sister figure to Figure 6.3. Sources in the first row from left to right: Boötes I, Canes Venatici I, II. In second row: Draco, Hercules, Leo I. In the first row: Leo II, Leo IV, Sextans. In the final row: Ursa Major I, Ursa Major II.	74
306	Figure B.1	Sister figure to Figure 7.2 for remaining SM primary annihilation channels studied for this thesis. These did not require any post generation smoothing and so are directly pulled from [64] with a binning scheme most helpful for a HAWC analysis.	75

LIST OF ABBREVIATIONS

- 311 **MSU** Michigan State University
312 **LANL** Los Alamos National Laboratory
313 **DM** Dark Matter
314 **SM** Standard Model
315 **HAWC** High Altitude Water Cherenkov Observatory
316 **dSph** Dwarf Spheroidal Galaxy

CHAPTER 1

INTRODUCTION

318 Is the text not rendering right? Ah ok it knows im basically drafting the doc still

CHAPTER 2

319

DARK MATTER IN THE COSMOS

320 **2.1 Introduction**

321 The dark matter problem can be summarized in part by the following thought experiment.

322 Let us say you are the teacher for an elementary school classroom. You take them on a field
323 trip to your local science museum and among the exhibits is one for mass and weight. The exhibit
324 has a gigantic scale, and you come up with a fun problem for your class.

325 You ask your class, "What is the total weight of the classroom? Give your best estimation to
326 me in 30 minutes, and then we'll check your guess on the scale. If your guess is within 10% of the
327 right answer, we will stop for ice cream on the way back."

328 The students are ecstatic to hear this, and they get to work. The solution is some variation of
329 the following strategy. The students should give each other their weight or best guess if they do
330 not know. Then, all they must do is add each student's weight and get a grand total for the class.

331 The measurement on the giant scale should show the true weight of the class. When comparing
332 the measured weight to your estimation, multiply the measurement by 1.0 ± 0.1 to get the $\pm 10\%$
333 tolerances for your estimation.

334 Two of your students, Sandra and Mario, return to you with a solution.

335 They say, "We weren't sure of everyone's weight. We used 65 lbs. for the people we didn't
336 know and added everyone who does know. There are 30 of us, and we got 2,000 lbs.! That's a ton!"

337 You estimated 1,900 lbs. assuming the average weight of a student in your class was 60 lbs.
338 So, you are pleased with Sandra's and Mario's answer. You instruct your students to all gather on
339 the giant scale and read off the weight together. To all your surprise, the scale reads *10,000 lbs.*!
340 10,000 is significantly more than a 10% error from 2,000. In fact, it is approximately 5 times more
341 massive than either your or your students' estimates. You think to yourself and conclude there
342 must be something wrong with the scale. You ask an employee to check the scale and verify it is
343 well calibrated. They confirm that the scale is in working order. You weigh a couple of students
344 individually to assess that the scale is well calibrated. Sandra weighs 59 lbs., and Mario weighs

345 62 lbs., typical weights for their age. You then weigh each student individually and see that their
346 weights individually do not deviate greatly from 60 lbs. So, where does all the extra weight come
347 from?

348 This thought experiment serves as an analogy to the Dark Matter problem. The important
349 substitution to make however is to replace the students with stars and the classroom with a galaxy,
350 say the Milky Way. Individually the mass of stars is well measured and defined with the Sun as our
351 nearest test case. However, when we set out to measure the mass of a collection of stars as large as
352 galaxies, our well-motivated estimation is wildly incorrect. There simply is no way to account for
353 this discrepancy except without some unseen, or dark, contribution to mass and matter in galaxies.
354 I set out in my thesis to narrow the possibilities of what this Dark Matter could be.

355 This chapter is organized like the following... **TODO: Text should look like ... Chapter x has**
356 **blah blah blah.**

357 2.2 Dark Matter Basics

358 Presently, a more compelling theory of cosmology that includes Dark Matter (DM) in order
359 to explain a variety of observations is Λ Cold Dark Matter, or Λ CDM. I present the evidence
360 supporting Λ CDM in Section 2.3 yet discuss the conclusions of the Λ CDM model here. According
361 to Λ CDM fit to observations on the Cosmic Microwave Background (CMB), DM is 26.8% of the
362 universe's current energy budget. Baryonic matter, stuff like atoms, gas, and stars, contributes to
363 4.9% of the universe's current energy budget [1, 2, 3].

364 DM is dark; it does not interact readily with light at any wavelength. DM also does not interact
365 noticeably with the other standard model forces (Strong and Weak) at a rate that is readily observed
366 [3]. DM is cold, which is to say that the average velocity of DM is below relativistic speeds [1].
367 'Hot' DM would not likely manifest the dense structures we observe like galaxies, and instead
368 would produce much more diffuse galaxies than what is observed [3, 1]. DM is old; it played a
369 critical role in the formation of the universe and the structures within it [1, 2].

370 Observations of DM have so far been only gravitational. The parameter space available to what
371 DM could be therefore is extremely broad. The broad DM parameter space is iteratively tested in

372 DM searches by supposing a hypothesis that has not yet been ruled out and performing observations
373 to test them. When the observations yield a null result, the parameter space is constrained further.
374 I present some approaches for DM searches in Section 2.4.

375 **2.3 Evidence for Dark Matter**

376 Dark Matter (DM) has been a looming problem in physics for almost 100 years. Anomalies
377 have been observed by astrophysicists in galactic dynamics as early as 1933 when Fritz Zwicky
378 noticed unusually large velocity dispersion in the Coma cluster. Zwicky's measurement was the
379 first recorded to use the Virial theorem to measure the mass fraction of visible and invisible matter
380 in celestial bodies [4]. From Zwicky in [5], "*If this would be confirmed, we would get the surprising*
381 *result that dark matter is present in much greater amount than luminous matter.*" Zwicky's and
382 others' observation did not instigate a crisis in astrophysics because the measurements did not
383 entirely conflict with their understanding of galaxies [4]. In 1978, Rubin, Ford, and Norbert
384 measured rotation curves for ten spiral galaxies [6]. Rubin et al.'s 1978 publication presented a
385 major challenge to the conventional understanding of galaxies that could no longer be dismissed by
386 measurement uncertainties. Evidence has been mounting ever since for this exotic form of matter.
387 The following subsections provide three compelling pieces of evidence in support of the existence
388 of DM.

389 **2.3.1 First Clues: Stellar Velocities**

390 Zwicky, and later Rubin, measured the stellar velocities of various galaxies to estimate their
391 virial mass. The Virial Theorem upon which these observations are interpreted is written as

$$2T + V = 0. \quad (2.1)$$

392 Where T is the kinetic energy and V is the potential energy in a self-gravitating system. The
393 classical Newton's law of gravity from stars and gas was used for gravitational potential modeled in
394 the observed galaxies:

$$V = -\frac{1}{2} \sum_i \sum_{j \neq i} \frac{m_i m_j}{r_{ij}}. \quad (2.2)$$

395 Zwicky et al. measured just the velocities of stars apparent in optical wavelengths [5]. Rubin et al.
 396 added by measuring the velocity of the hydrogen gas via the 21 cm emission line of Hydrogen [6].
 397 The velocities of the stars and gas are used to infer the total mass of galaxies and galaxy clusters
 398 via Equation (2.1). An inferred mass is obtained from the luminosity of the selected sources. The
 399 two inferences are compared to each other as a luminosity to mass ratio which typically yielded [1]

$$\frac{M}{L} \sim 400 \frac{M_{\odot}}{L_{\odot}} \quad (2.3)$$

400 M_{\odot} and L_{\odot} referring to stellar mass and stellar luminosity, respectively. These ratios clearly indicate
 401 a discrepancy in apparent light and mass from stars and gas and their velocities.

402 Rubin et al. [6] demonstrated that the discrepancy was unlikely to be an underestimation of
 403 the mass of the stars and gas. The inferred "dark" mass was up to 5 times more than the luminous
 404 mass. This dark mass also needed to extend well beyond the extent of the luminous matter.

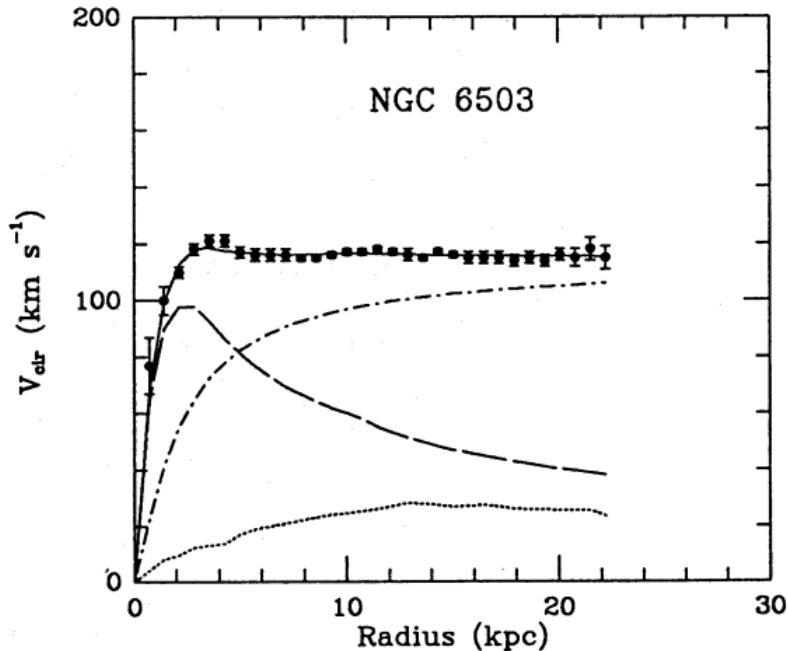


Figure 2.1 Rotation curve fit to NGC 6503 from [7]. Dashed line is the contribution from visible matter. Dotted curves are from gas. Dash-dot curves are from dark matter (DM). Solid line is the composite contribution from all matter and DM sources. Data are indicated with bold dots with error bars. Data agree strongly with a matter + DM composite prediction.

405 Figure 2.1 features one of many rotation curves plotted from the stellar velocities within galaxies.

406 The measured rotation curves mostly feature a flattening of velocities at higher radius which is not
407 expected if the gravity was only coming from gas and luminous matter. The extension of the
408 flat velocity region also indicates that the DM is distributed far from the center of the galaxy.
409 Modern velocity measurements include significantly larger objects, galactic clusters, and smaller
410 objects, dwarf galaxies. Yet, measurements along this regime are leveraging the Virial theorem
411 with Newtonian potential energies. We know Newtonian gravity is not a comprehensive description
412 of gravity. New observational techniques have been developed since 1978, and those are discussed
413 in the following sections.

414 **2.3.2 Evidence for Dark Matter: Gravitational Lensing**

415 Modern evidence for dark matter comes from new avenues beyond stellar velocities. Grav-
416 itational lensing from DM is a new channel from general relativity. General relativity predicts
417 aberrations in light caused by massive objects. In recent decades we have been able to measure the
418 lensing effects from compact objects and DM halos. Figure 2.2 shows how different massive ob-
419 jects change the final image of a faraway galaxy resulting from gravitational lensing. Gravitational
420 lensing developed our understanding of dark matter in two important ways.

421 Gravitational lensing provides additional compelling evidence for DM. The observation of two
422 merging galactic clusters in 2006, shown in Figure 2.3, provided a compelling argument for DM
423 outside the Standard Model. These clusters merged recently in astrophysical time scales. Galaxies
424 and star cluster have mostly passed by each other as the likelihood of their collision is low. Therefore,
425 these massive objects will mostly track the highest mass, dark and/or baryonic, density. Yet, the
426 intergalactic gas is responsible for the majority of the baryonic mass in the systems [4]. These gas
427 bodies will not phase through and will heat up as they collide together. The hot gas is located via
428 x-ray emission from the cluster. Two observations of the clusters were performed independently of
429 each other.

430 The first was the lensing of light around the galaxies due to their gravitational influences.
431 When celestial bodies are large enough, the gravity they exert bends space and time itself. The
432 warped space-time lenses light and will deflect in an analogous way to how glass lenses will bend

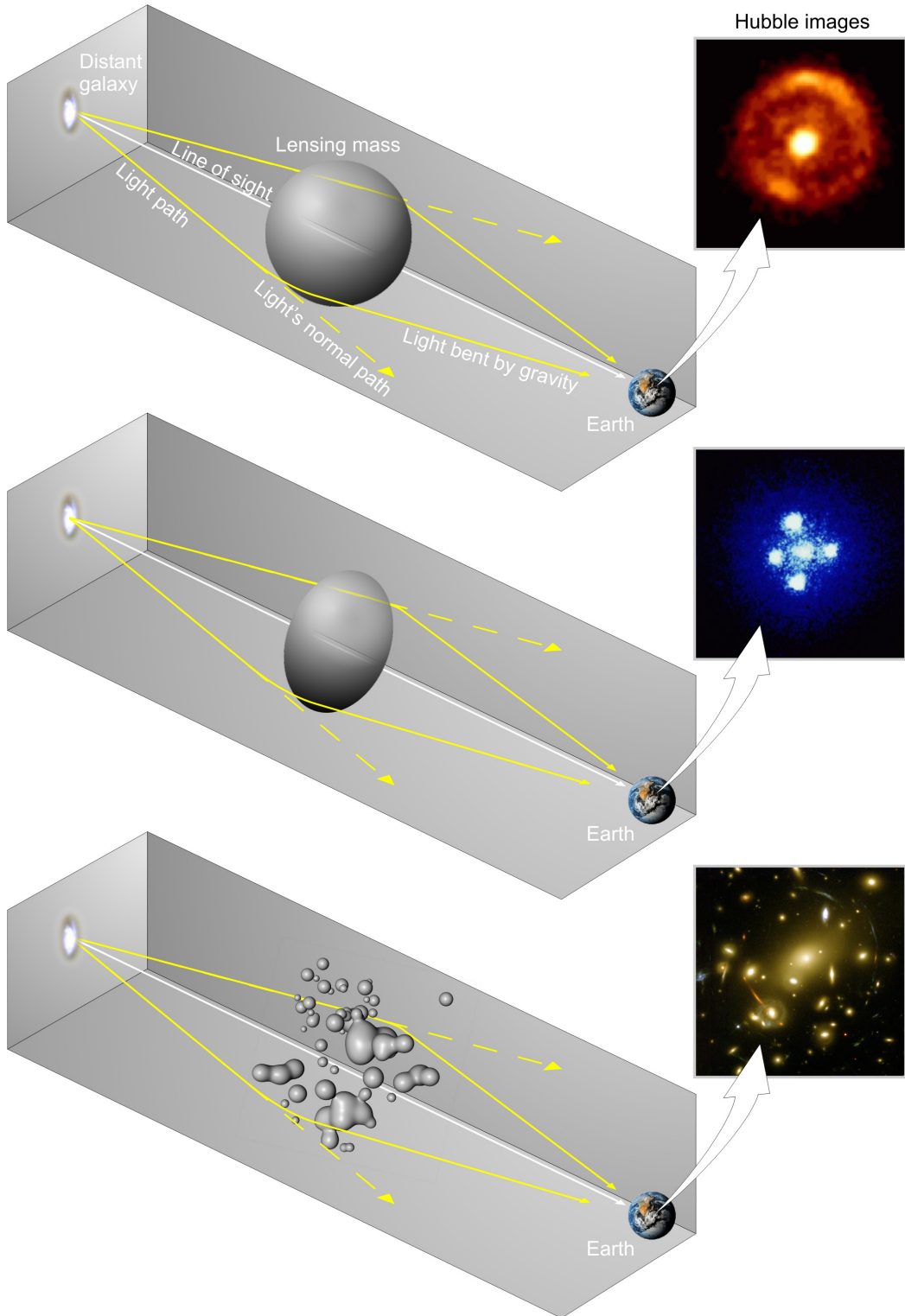


Figure 2.2 Light from distant galaxy is bent in unique ways depending on the distribution of mass between the galaxy and Earth. Yellow dashed lines indicate where the light would have gone if the matter were not present [8].

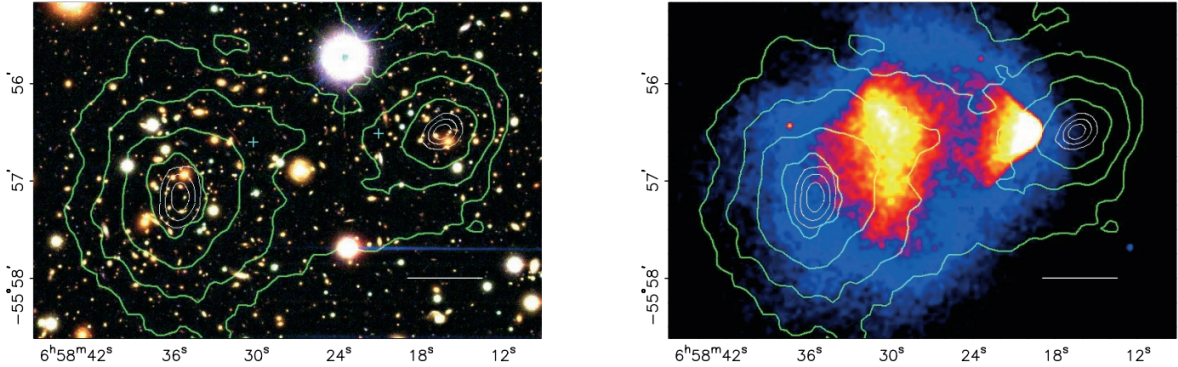


Figure 2.3 (left) Optical image of galactic cluster 1E0657-558. (right) X-ray image of the cluster with redder meaning hotter and higher baryon density. (both) Green contours are reconstruction of gravity contours from weak lensing. White rings are the best fit mass maxima at 68.3%, 95.5%, and 99.7% confidence. The matter maxima of the clusters are clearly separated from x-ray maxima. [9]

433 light, see Figure 2.2. With a sufficient understanding of light sources behind a massive object, we
 434 can reconstruct the contours of the gravitational lenses. The gradient of the contours shown in
 435 Figure 2.3 then indicates how dense the matter is and where it is.

436 The x-ray emission can then be observed from the clusters. Since these galaxies are mostly gas
 437 and are merging, then the gas should be getting hotter. If they are merging, the x-ray emissions
 438 should be the strongest where the gas is mostly moving through each other. Hence, X-ray emission
 439 maps out where the gas is in the merging galaxy cluster.

440 The lensing and x-ray observations were done on the Bullet cluster featured on Figure 2.3.
 441 The x-ray emissions do not align with the gravitational contours from lensing. The incongruence
 442 in mass density and baryon density suggests that there is a lot of matter somewhere that does
 443 not interact with light. Moreover, this dark matter cannot be baryonic [9]. The Bullet Cluster
 444 measurement did not really tell us what DM is exactly, but it did give the clue that DM also does
 445 not interact with itself very strongly. If DM did interact strongly with itself, then it would have been
 446 more aligned with the x-ray emission [9]. There have been follow-up studies of galaxy clusters with
 447 similar results. The Bullet Cluster and others like it provide a persuasive case against something
 448 possibly amiss in our gravitational theories.

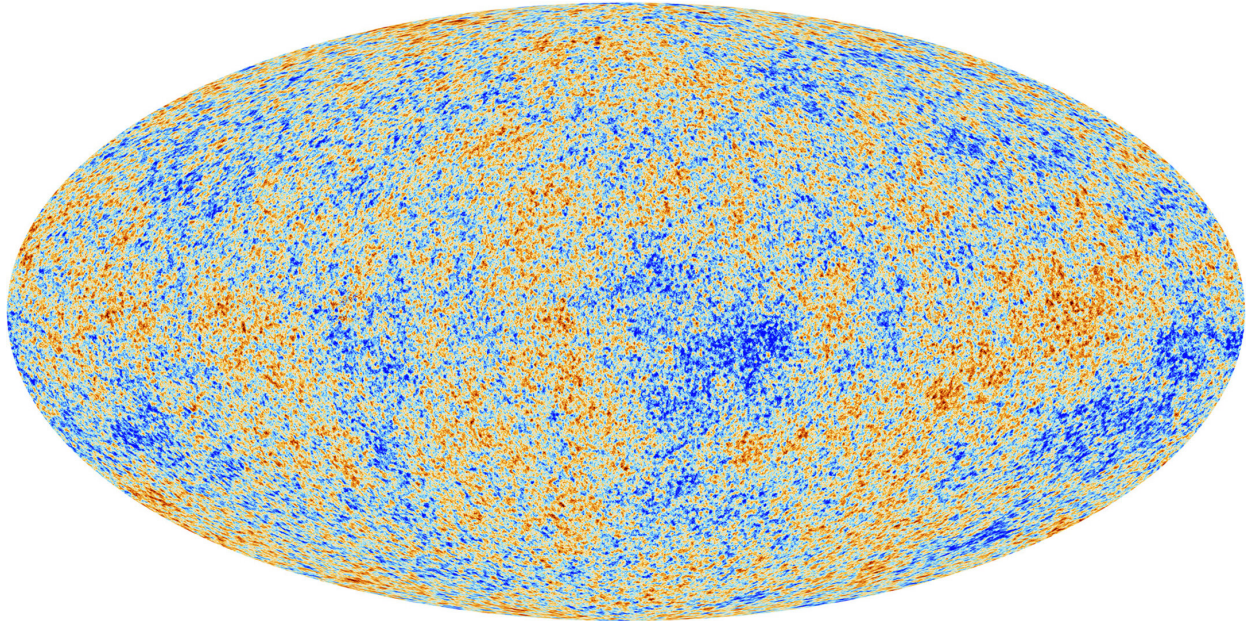


Figure 2.4 Plank CMB sky. Sky map features small variations in temperature in primordial light. These anisotropies are used to make inferences about the universe's energy budget and developmental history. [10]

449 **2.3.3 Evidence for Dark Matter: Cosmic Microwave Background**

450 The Cosmic Microwave Background (CMB) is the primordial light from the early universe
451 when Hydrogen atoms formed from the free electron and proton soup in the early universe. The
452 CMB is the earliest light we can observe; released when the universe was about 380,000 years old.
453 Then we look at how the simulated universes look like compared to what we see. Figure 2.4 is the
454 most recent CMB image from the Plank satellite after subtracting the average value and masking the
455 galactic plane [10]. Redder regions indicate a slightly hotter region in the CMB, and blue indicates
456 colder. The intensity variations are on the order of 1 in 1000 with respect to the average value.

457 The Cosmic Microwave Background shows that the universe had DM in it from an incredibly
458 early stage. To measure the DM, Dark Energy, and matter fractions of the universe from the CMB,
459 the image is analyzed into a power spectrum, which shows the amplitude of the fluctuations as
460 a function of spherical multipole moments. Λ CDM provides the best fit to the power spectra of
461 the CMB as shown in Figure 2.5. The CMB power spectrum is quite sensitive to the fraction
462 of each energy contribution in the early universe. Low l modes are dominated by variations
463 in gravitational potential. Intermediate l emerge from oscillations in photon-baryon fluid from

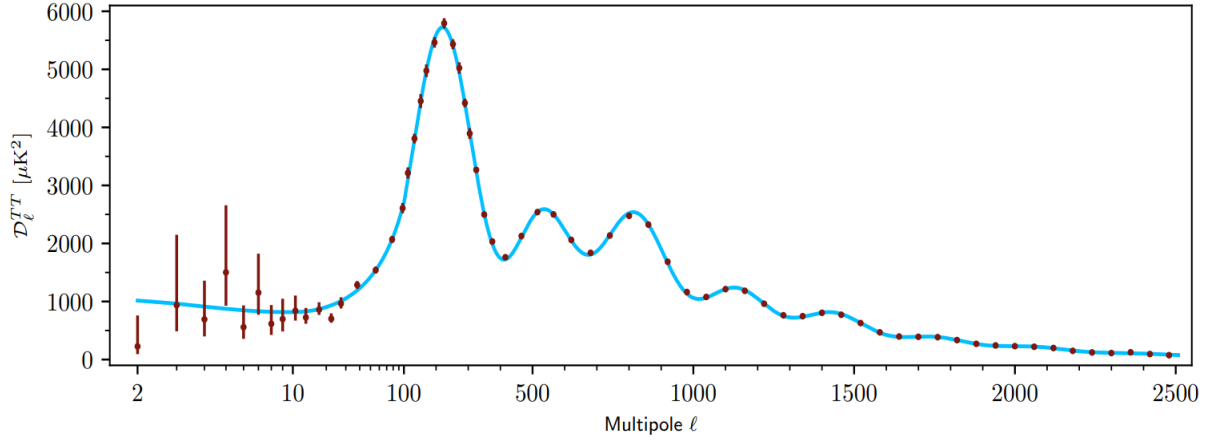


Figure 2.5 Observed Cosmic Microwave Background power spectrum as a function of multipole moment from Plank [10]. Blue line is best fit model from Λ CDM. Red points and lines are data and error, respectively.

464 competing baryon pressures and gravity. High l is a damped region from the diffusion of photons
 465 during electron-proton recombination. [1]

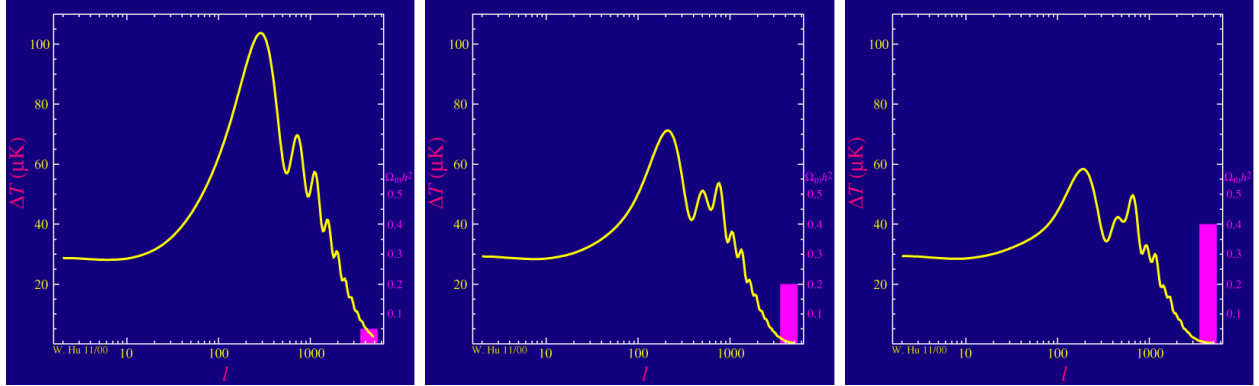


Figure 2.6 Predicted power spectra of CMB for different $\Omega_m h^2$ values for fixed baryon density from [11]. (left) Low $\Omega_m h^2$ increases the prominence of first and second peaks. (middle) $\Omega_m h^2$ is most similar to the observed power spectrum. The second and third peaks are similar in height. (right) $\Omega_m h^2$ is large which suppresses the first peak and raises the prominence of the third peak.

466 The harmonics would look quite different for a universe with less DM. Figure 2.6 demonstrates
 467 the effect $\Omega_m h^2$ has on the expected power spectrum for fixed baryon matter density. [11] Sweeping
 468 $\Omega_m h^2$ in this way clearly shows the effect dark matter has on the CMB power spectrum. The
 469 observations fit well with the Λ CDM model, and the derived fractions are as follows. The matter
 470 fraction: $\Omega_m = 0.3153$; and the baryon fraction: $\Omega_b = 0.04936$ [10]. Plank's observations also
 471 provide a measure of the Hubble constant, H_0 . H_0 especially has seen a growing tension in the

472 past decade that continues to deepened with observations from instruments like the James Webb
473 Telescope [12, 13]. As Hubble tensions deepen, we may find that perhaps Λ **CDM**, despite its
474 successes, is missing some critical physics.

475 Overall, the Newtonian motion of stars in galaxies, weak lensing from galactic clusters, and
476 power spectra from primordial light form a compelling body of research in favor of dark matter.
477 It takes another leap of theory and experimentation to make observations of DM that are non-
478 gravitational in nature. In Section 2.3, the evidence for DM implies strongly that the DM is matter
479 and not a lost parameter in the gravitational fields between massive objects. Finally, if we take one
480 axiom: that this matter has quantum behavior, such as being described by some Bohr wavelength
481 and abiding by some fermion or boson statistics; then we arrive at particle dark matter. One particle
482 DM hypothesis is the Weakly Interacting Massive Particle (WIMP). This DM candidate theory is
483 discussed further in the next section and is the focus of this thesis.

484 **2.4 Searching for Dark Matter: Particle DM**

485 Section 2.4 shows the Standard Model of particle physics and is currently the most accurate
486 model for the dynamics of fundamental particles like electrons and photons. The current status
487 of the SM does not have a viable DM candidate. When looking at the standard model, we can
488 immediately exclude any charged particle because charged particles interact strongly with light.
489 Specifically, this will rule out the following charged, fundamental particles: $e, \mu, \tau, W, u, d, s, c, t, b$
490 and their corresponding antiparticles. Recalling from Section 2.2 that DM must be long-lived and
491 stable over the age of the universe which excludes all SM particles with decay half-lives at or shorter
492 than the age of the universe. The lifetime constraint additionally eliminates the Z and H bosons.
493 Finally, the candidate DM needs to be somewhat massive. Recall from Section 2.2 that DM is cold
494 or not relativistic through the universe. This eliminates the remaining SM particles: $\nu_{e,\mu,\tau}, g, \gamma$ as
495 DM candidates. Because there are no DM candidates within the SM, the DM problem strongly
496 hints to physics beyond the SM (BSM).

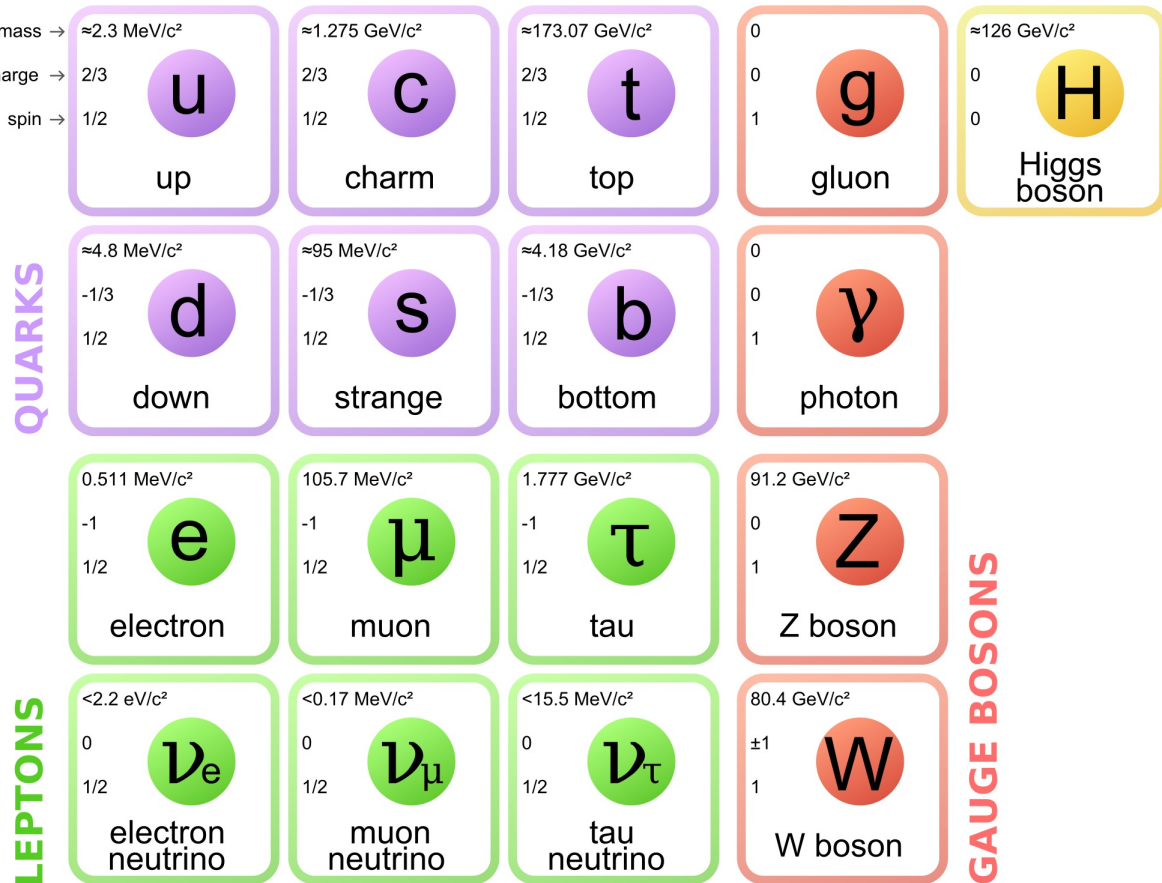


Figure 2.7 The Standard Model (SM) of particle physics. Figure taken from <http://www.quantumdiaries.org/2014/03/14/the-standard-model-a-beautiful-but-flawed-theory/>

497 2.4.1 Shake it, Break it, Make it

498 When considering DM that couples in some way with the SM, the interactions are roughly
 499 demonstrated by interaction demonstrated in Figure 2.8. The figure is a simplified Feynman
 500 diagram where the arrow of time represents the interaction modes of: **Shake it, Break it, Make it.**

501 **Shake it** refers to the direct detection of dark matter. Direct detection interactions start with
 502 a free DM particle and an SM particle. The DM and SM interact via elastic or inelastic collision
 503 and recoil away from each other. The DM remains in the dark sector and imparts some momentum
 504 onto the SM particle. The hope is that the momentum imparted onto the SM particle is sufficiently
 505 high enough to pick up with extremely sensitive instruments. Because we cannot create the DM in
 506 the lab, a direct detection experiment must wait until DM is incident on the detector. Most direct
 507 detection experiments are therefore placed in low-background environments with inert detection

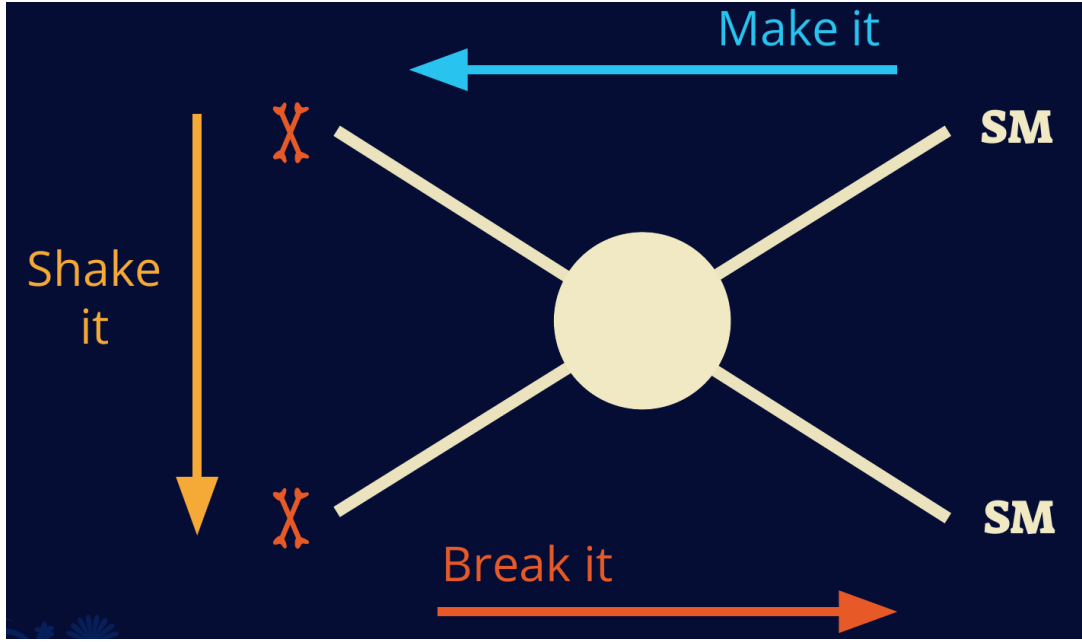


Figure 2.8 Simplified Feynman diagram demonstrating different ways DM can interact with SM particles. The 'X's refer to the DM particles whereas the SM refer to fundamental particles in the SM. The large circle in the center indicates the vertex of interaction and is purposely left vague. The colored arrows refer to different directions of time as well as their respective labels. The arrows indicate the initial and final state of the DM -SM interaction in time.

508 media like the noble gas Xenon. [14]

509 **Make it** refers to the production of DM from SM initial states. The experiment starts with
 510 particles in the SM. These SM particles are accelerated to incredibly high energies and then collide
 511 with each other. In the confluence of energy, DM hopefully emerges as a byproduct of the SM
 512 annihilation. Often it is the collider experiments that are energetic enough to hypothetically produce
 513 DM. These experiments include the world-wide collaborations ATLAS and CMS at CERN where
 514 proton collide together at extreme energies. The DM searches, however, are complex. DM likely
 515 does not interact with the detectors and lives long enough to escape the detection apparatus of
 516 CERN's colliders. This means any DM production experiment searches for an excess of events
 517 with missing momentum or energy in the events. An example event with missing transverse
 518 momentum is shown in Figure 2.9. The missing momentum with no particle tracks implies a
 519 neutral particle carried the energy out of the detector. However, there are other neutral particles
 520 in the SM, like neutrons or neutrinos, so any analysis has to account for SM signatures of missing

521 momentum. [15]

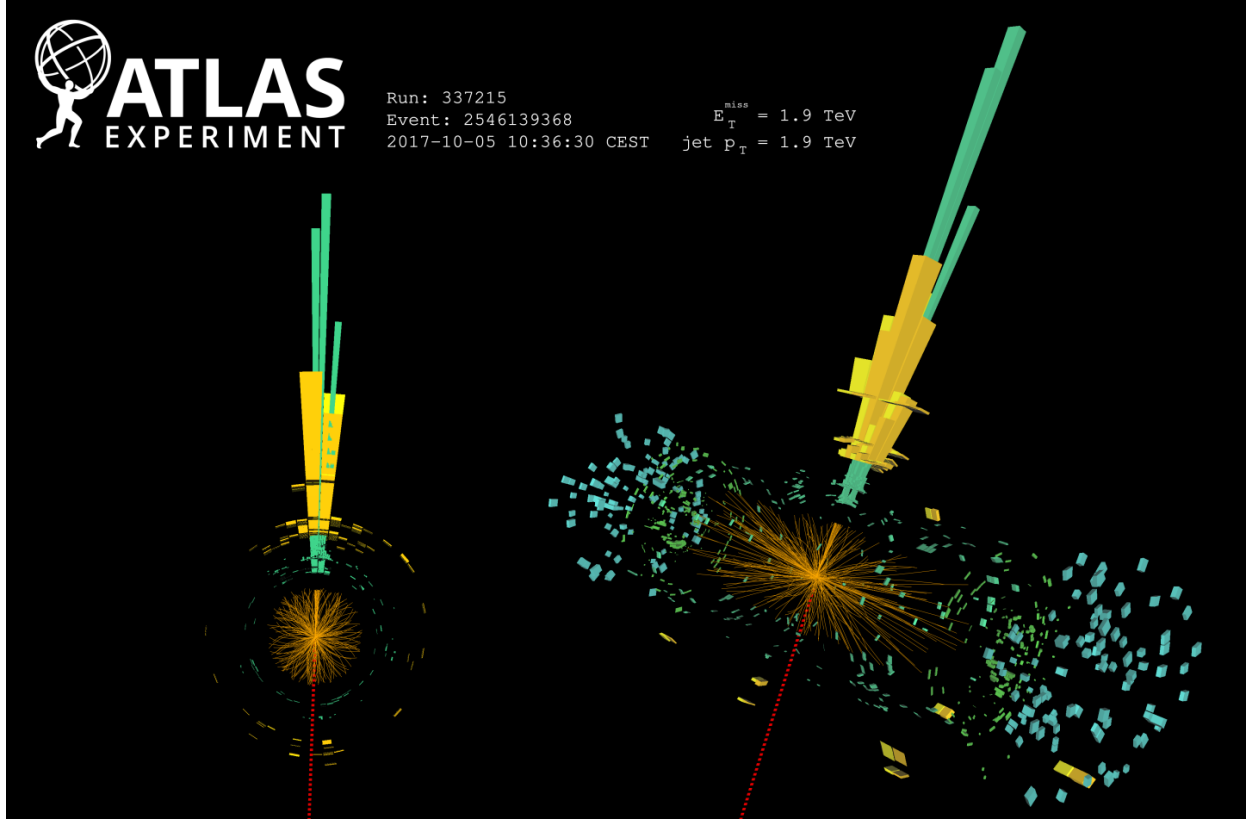


Figure 2.9 A single jet event in ATLAS detector from 2017 [16]. Jet momentum was observed to be 1.9 TeV. Missing transverse momentum was observed to be 1.9 TeV compared to the initial transverse momentum of the event was 0. Implied MET is traced by a red dashed line in event display.

522 2.4.2 Break it: Standard Model Signatures of Dark Matter through Indirect Searches

523 **Break it** refers to the creation of SM particles from the dark sector, and it is the primary focus
524 of this thesis. The interaction begins with DM or in the dark sector. The hypothesis is that this
525 DM will either annihilate with itself or decay and produce an SM byproduct. This method is
526 often referred to as the Indirect Detection of DM because we have no lab to directly control or
527 manipulate the DM. Therefore, most indirect DM searches are performed using observations of
528 known DM densities among the astrophysical sources. The strength is that we have the whole of the
529 universe and its 13.6-billion-year lifespan to use as a detector and particle accelerator. Additionally,
530 locations of dark matter are well cataloged since it was astrophysical observations that presented

531 the problem of DM in the first place.

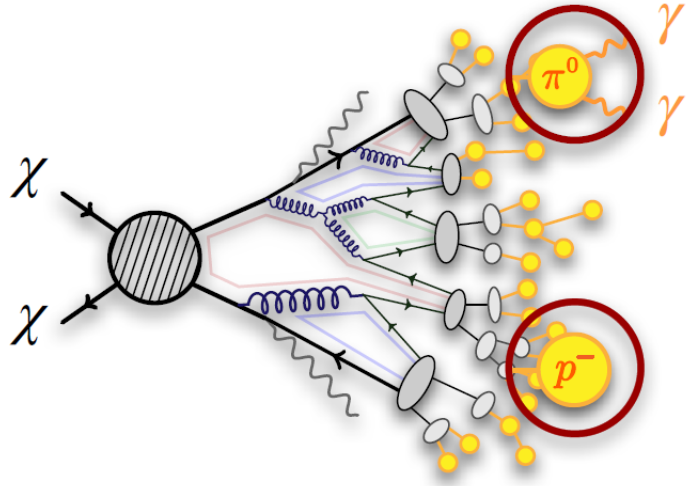


Figure 2.10 More detailed pseudo-Feynman diagram of particle cascade from dark matter annihilation into 2 quarks. The quarks hadronize and down to stable particles like γ or the anti-proton (p^-). Diagram pulled from ICRC 2021 presentation on DM annihilation search [17].

532 However, anything can happen in the universe. There are many difficult to deconvolve back-
533 grounds when searching for DM. One prominent example is the galactic center. We know the
534 galactic center has a large DM content because of stellar kinematics in our Milky Way and DM halo
535 simulations. Yet, any signal from the galactic center is challenging to parse apart from the extreme
536 environment of our supermassive black hole, unresolved sources, and diffuse emission from the
537 interstellar medium [18]. Despite the challenges, any DM model that yields evidence in the other
538 two observation methods, **Shake it or Make it** must be corroborated with indirect observations of
539 the known DM sources. Without corroborating evidence, DM observation in the lab is hard-pressed
540 to demonstrate that it is the model contributing to the DM seen at the universal scale.

541 In the case of WIMP DM, signals are described in terms of primary SM particles produced
542 from DM decay or annihilation. The SM initial state particles are then simulated down to stable
543 final states such as the γ , ν , p , or e which can traverse galactic lengths to reach Earth.

544 Figure 2.10 shows the quagmire of SM particles that emerges from SM initial states that are not
545 stable [17]. There are many SM particles with varying energies that can be produced in such an

546 interaction. For any arbitrary DM source and stable SM particle, the SM flux from DM annihilating
 547 to a neutral particle in the SM, ϕ , from a region in the sky is described by the following.

$$\frac{d\Phi_\phi}{dE_\phi} = \frac{\langle\sigma v\rangle}{8\pi m_\chi^2} \frac{dN_\phi}{dE_\phi} \times \int_{\text{source}} d\Omega \int_{l.o.s} \rho_\chi^2 dl(r, \theta') \quad (2.4)$$

548 In Equation (6.1), $\langle\sigma v\rangle$ is the velocity-weighted annihilation cross-section of DM to the SM. m_χ
 549 refers to the mass of DM, noted with Greek letter χ . $\frac{dN_\phi}{dE_\phi}$ is the N particle flux weighted by the
 550 particle energy. An example is provided in Figure 2.11 for the γ final state. The integrated terms
 551 are performed over the solid angle, $d\Omega$, and line of sight, l.o.s. ρ is the density of DM for a
 552 location (r, θ') in the sky. The terms left of the ' \times ' are often referred to as the particle physics
 553 component. The terms on the right are referred to as the astrophysical component. For decaying
 554 DM, the equation changes to...

$$\frac{d\Phi_\phi}{dE_\phi} = \frac{1}{4\pi\tau m_\chi} \frac{dN_\phi}{dE_\phi} \times \int_{\text{source}} d\Omega \int_{l.o.s} \rho_\chi dl(r, \theta') \quad (2.5)$$

555 In Equation (7.1), τ is the decay lifetime of the DM. Just as in Equation (6.1), the left and right
 556 terms are the particle physics and the astrophysical components respectively. The integrated
 557 astrophysical component of Equation (6.1) is often called the J-Factor. Whereas the integrated
 558 astrophysical component of Equation (7.1) is often called the D-Factor.

559 Exact DM $\text{DM} \rightarrow \text{SM SM}$ branching ratios are not known, so it is usually assumed to go 100%
 560 into an SM particle/anti-particle. Additionally, when a DM annihilation or decay produces one of
 561 the neutral, long-lived SM particles (ν or γ), the particle is traced back to a DM source. For DM
 562 above GeV energies, there are very few SM processes that can produce particles with such a high
 563 energy. Seeing such a signal would almost certainly be an indication of the presence of dark matter.
 564 Fortunately, the universe provides us with the largest volume and lifetime ever for a particle physics
 565 experiment.

566 2.5 Sources for Indirect Dark Matter Searches

567 The first detection of DM relied on optical observations. Since then, we have developed new
 568 techniques to find DM dense regions. As described in Section 2.3.1, many DM dense regions were
 569 through observing galactic rotation curves. Our Milky Way galaxy is among DM dense regions

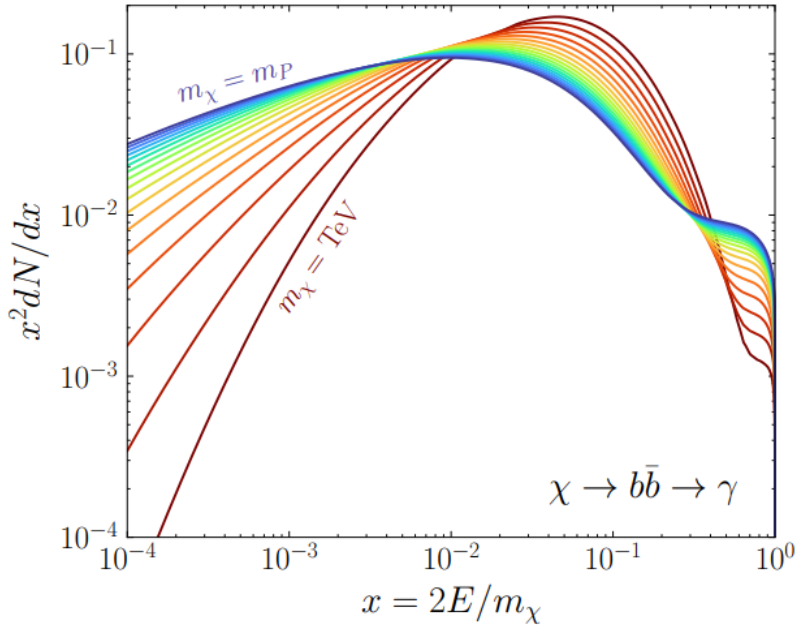


Figure 2.11 Dark Matter (DM) decay spectrum for $b\bar{b}$ initial state and γ final state. Redder spectra are for larger DM masses. Bluer spectra are light DM masses. x is a unitless factor defined as the ratio of the mass of DM, m_χ , and the final state particle energy E_γ . Figure from [19].

discovered, and it is the largest nearby DM dense region to look at. Additionally, the DM halo surrounding the Milky Way is clumpy [18]. There are regions in the DM halo of the Milky Way that have more DM than others that have captured gas over time. These sub-halos were dense enough collapse gas and form stars. These apparent sub galaxies are known as dwarf spheroidal galaxies and are the main sources studied in this thesis. Each source type comes with different trade-offs. Galactic Center studies will be very sensitive to the assumed distribution of DM. The central DM density can vary substantially as demonstrated in Figure 2.12. At distances close to the center of the galaxy, or small r , the differences in DM densities can be 3-4 orders of magnitude. Searches toward the galactic center will therefore be quite sensitive to the assumed DM distribution.

Searches toward Dwarf Spheroidal Galaxies (dSph's) suffer from uncertainties in the DM density less than the galactic center studies. This is mostly from their diminutive size being smaller than the angular resolution of most γ -ray observatories [18]. The DM content dSph's are typically determined with the Virial theorem, Equation (2.1), and are usually majority DM [18] in mass. DSph's tend to be ideal sources to look at for DM searches. Their environments are quiet with little

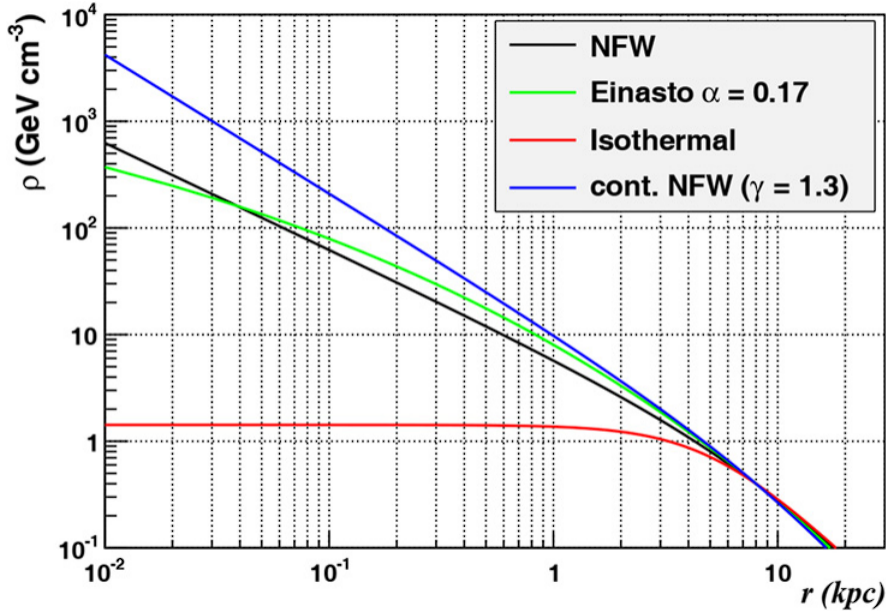


Figure 2.12 Different dark matter density profiles compared. Some models produce exceptionally large densities at small r [20].

584 astrophysical background. Unlike the galactic center, the most active components of dSph's are the
 585 stars within them versus a violent accretion disc around a black hole. All this together means that
 586 dSph's are among the best sources to look at for indirect DM searches. dSph's are the targets of
 587 focus for this thesis.

588 2.6 Multi-Messenger Dark Matter

589 Astrophysics entered a new phase in the past few decades that leverages our increasing sensitivity
 590 to SM channels and general relativity (GR). Up until the 21st century, astrophysical observations
 591 were performed with photons (γ) only. Astrophysics with this 'messenger' is fairly mature now.
 592 Novel observations of the universe have since only adjusted the sensitivity of the wavelength of
 593 light that is observed except at MeV energies. Gems like the CMB [10], and more have ultimately
 594 been observations of different wavelengths of light. Multi-messenger astrophysics proposes using
 595 other SM particles such the p^{+-} , or ν or gravitation waves predicted by general relativity.

596 The experiment LIGO had a revolutionary discovery in 2016 with the first detection of a binary
 597 black hole merger [21]. This opened the collective imagination to observing the universe through
 598 gravitational waves. There has also been a surge of interest in the neutrino (ν) sector. IceCube

599 demonstrated that we are sensitive to neutrinos in regions that correlate with significant photon
 600 emission like the galactic plane [22]. Neutrinos, like gravitational waves and light, travel mostly
 601 unimpeded from their source to our observatories. This makes pointing to the originating source
 602 of these messengers much easier than it is for cosmic rays which are deflected from their source by
 603 magnetic fields.

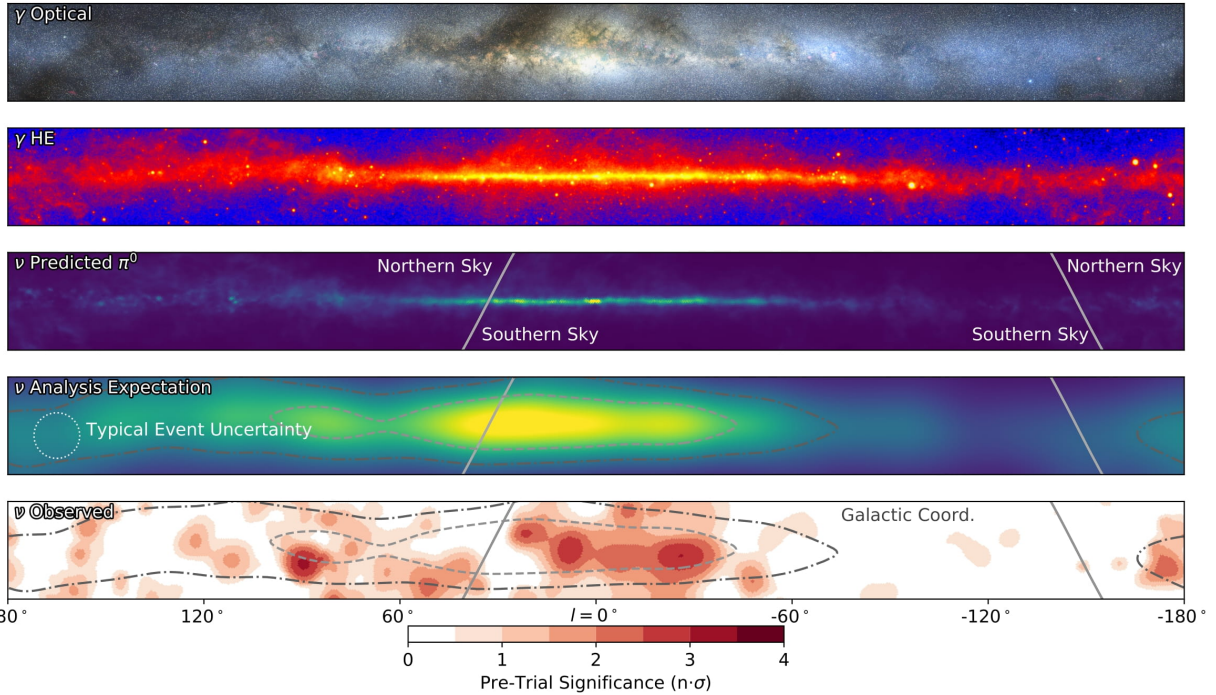


Figure 2.13 The Milky Way Galaxy in photons (γ) and neutrinos (ν) [22]. The Galactic center is at $l=0^\circ$ and is the brightest region in all panels. (top) An Optical color image of the Milky Way galaxy seen from Earth. Clouds of gas and dust obscure some light from stars. (2nd down) Integrated flux of γ -rays observed by the Fermi-LAT telescope [23]. (middle) Expected neutrino emission that corresponds with Fermi-LAT observations. (2nd up) Expected neutrino emission profile after considering detector systematics of IceCube. (bottom) Observed neutrino emission from region of the galactic plane. Substantial neutrino emission was detected.

604 The IceCube collaboration recently published a groundbreaking result of the Milky Way in
 605 neutrinos. The recent result from IceCube, shown in Figure 2.13, proves that we can make
 606 observations under different messenger regimes. The top two panels show the appearance of the
 607 galactic plane to different wavelengths of light. Some sources are more apparent in some panels,
 608 while others are not. This new channel is powerful because neutrinos are readily able to penetrate
 609 through gas and dust in the Milky Way. This new image also refines our understanding of how high

610 energy particles are produced. For example, the fit to IceCube data prefers neutrino production
 611 from the decay of π^0 [22].

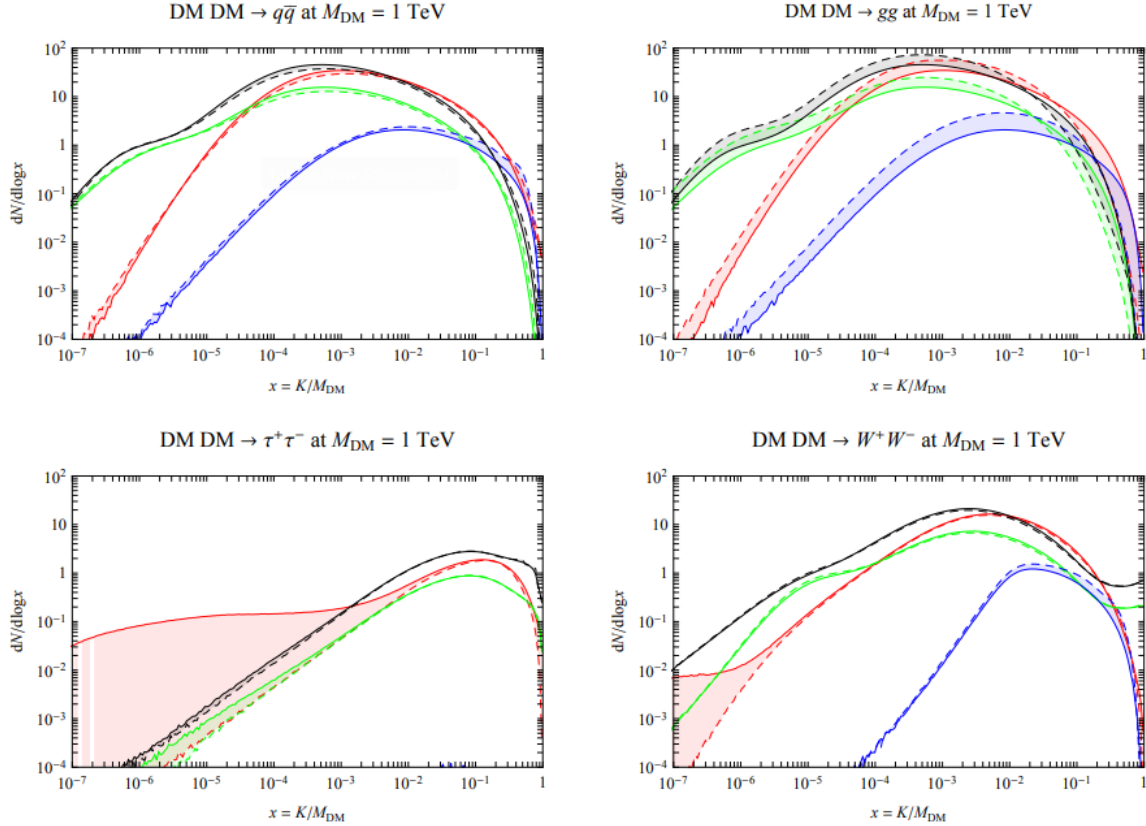


Figure 2.14 Dark Matter annihilation spectra for different final state particle and standard model annihilation channels [24]. Photons (red), e^\pm (green), \bar{p} (blue), ν (black).

612 Exposing our observations to more cosmic messengers greatly increases our sensitivity to
 613 rare processes. In the case of DM, Figure 2.14, there are many SM particles produced in DM
 614 annihilation. Among the final state fluxes are gammas and neutrinos. Charged particles are also
 615 produced however they would not likely make it to Earth since they will be deflected by magnetic
 616 fields between the source and Earth. This means observatories that can see the neutral messengers
 617 are especially good for DM searches and for combining data for a multi-messenger DM search.

CHAPTER 3

618 MULTIMESSENGER ASTROPHYSICS: DETECTING HIGH ENERGY NEUTRAL 619 MESSENGERS

620 3.1 Introduction

621 Before the 20th century, all astrophysics observations were optical in nature. We literally only
622 saw things with highly magnified optical observations. Then we discovered cosmic rays. cosmic
623 rays are charged particles, typically naked protons or H+. This was seen by Victor Hess in 19??.
624 Around the same time we discovered neutrinos from beta decay. Sometime around 1950 we started
625 to build neutrino detectors which were mostly sensitive to neutrinos from the sun. Finally, it was
626 theorized that compact objects like black holes and neutron stars would create waves in space-time
627 when they experience mergers or collisions.

628 In the 21st century, we have developed new observation techniques and detectors that are no only
629 sensitive to these four messengers - photons ([TODO: photon](#)), neutrinos ([TODO: nu](#)), Cosmic
630 Rays (CR), and Gravitational Wave (WV) - we're collect high energy versions of these events.
631 For the standad model particles, we're now sensitive to all messengers above the MeV eneryg
632 range. Additionally, the GW's were sensitive to are in the stellar mass black hole region and above
633 within our galactic neighborhood. This means were becoming sensitive to the fundamental physics
634 occuring within the universe and we can rely on the universe as a TeV+ particle accelerator. We
635 also have the abaility to correlate high energy events across messengers and gain new insights on
636 the processes that occur in our universe.

637 This thesis focuses on very high energy (VHE) gamma rays and neutrinos. These can both be
638 observed through the water cherenkov detection technique altho not exclusively. Methods on how
639 to detect and observe these neutral messengers are discussed Section 3.3 and Section 3.4

640 3.2 Charged Particles in a Medium

641 For high enery gamma-rays and neutrinos, we can exploit the same effect that charged particles
642 have with water. This effect is known as Cherenkov radiation. Cherenkov Radiation occurs when a
643 charged particle, usually electrons (e) or muons (μ), traverse a medium, like water, faster than the

644 speed of light in that medium. This is similar to sonic boom where an object moves through air
645 faster than the speed of sound in air. Cherenkov radiation can therefore be thought of as an 'optic
646 boom'. Many astro-particle physics experiments will use water as the medium as because water
647 has a unique set of properties ideal for charged particle tracking.



Figure 3.1 TODO: Show a nuclear reactor with cherenkov radiation[NEEDS A SOURCE][FACT CHECK THIS]

648 The frequency of light emitted due to cherenkov radiation follows the equation:

$$INSERT\ Cherenkov\ wavelength\ calc\ HERE. \quad (3.1)$$

649 The absorption spectra is shown in the following figure:

650 **3.3 Photons (γ)**

651 **3.4 Neutrinos (ν)**

652 **3.5 Opportunities to Combine for Dark Matter**



Figure 3.2 TODO: absorption spectrum of liquid and solid water[NEEDS A SOURCE][FACT CHECK THIS]

CHAPTER 4

653 **HIGH ALTITUDE WATER CHERENKOV (HAWC) OBSERVATORY**

654 **4.1 The Detector**

655 **4.2 Events Reconstruction and Data Acquisition**

656 **4.2.1 G/H Discrimination**

657 **4.2.2 Angle**

658 **4.2.3 Energy**

659 **4.3 Remote Monitoring**

660 **4.3.1 ATHENA Database**

661 **4.3.2 HOMER**

662

CHAPTER 5

ICECUBE NEUTRINO OBSERVATORY

663 **5.1 The Detector**

664 **5.2 Events Reconstruction and Data Acquisition**

665 **5.2.1 Angle**

666 **5.2.2 Energy**

667 **5.3 Northern Test Site**

668 **5.3.1 PIgeon remote dark rate testing**

669 **5.3.2 Bulkhead Construction**

CHAPTER 6

GLORY DUCK: MULTI-WAVELENGTH SEARCH FOR DARK MATTTER ANNIHILATION TOWARDS DWARF SPHEROIDAL GALAXIES

6.1 Introduction

The field of astrophysics now has several instruments and observatories sensitive to high energy gamma-rays. The energy sensitivity for the modern gamma-ray program spans many orders of magnitude. Figure 6.1 demonstrates these similar sensitivities across energies for the five experiments: Fermi-LAT, HAWC, HESS, MAGIC, and VERITAS.

Each of the five experiments featured in Figure 6.1 have independently searched for DM annihilation from dwarf spheroidal galaxies (dSph) and set limits. Intriguingly, there are regions of substantial overlap in their energy sensitivities. This clearly motivates an analysis that combines data from these five. Each experiment has unique gamma-ray detection methods and their weaknesses and strengths can be leveraged with each other. The HAWC gamma-ray observatory is extensively introduced in chapter 4, so it is not introduced here. A brief description of the remaining experiments are in the following paragraphs.

The Large Area Telescope (LAT) is a pair conversion telescope mounted on the NASA Fermi satellite in orbit \sim 550 km above the Earth [26]. LAT's field of view covers about 20% of the whole sky, and it sweeps the whole sky approximately every 3 hours. LAT's gamma-ray energy sensitivity ranges from 20 MeV up to 1 TeV. Previous DM searches towards dSphs using Fermi-LAT are published in [27] and [28]

The High Energy Spectroscopic System (HESS), Major Atmospheric Gamma Imaging Cherenkov (MAGIC), and Very Energetic Radiation Imaging Telescope Array System (VERITAS) are arrays of Imaging Atmospheric Cherenkov Telescopes (IACT). These telescopes observe the Cherenkov light emitted from gamma-ray showers in the Earth's atmosphere. The field of view for these telescopes is no larger than 5° with energy sensitivities ranging from 30 GeV up to 100 TeV [29, 30, 31]. IACTs are able to make precise observations in selected regions of the sky, however can only be operated in ideal dark conditions. HESS's observations of the dwarves

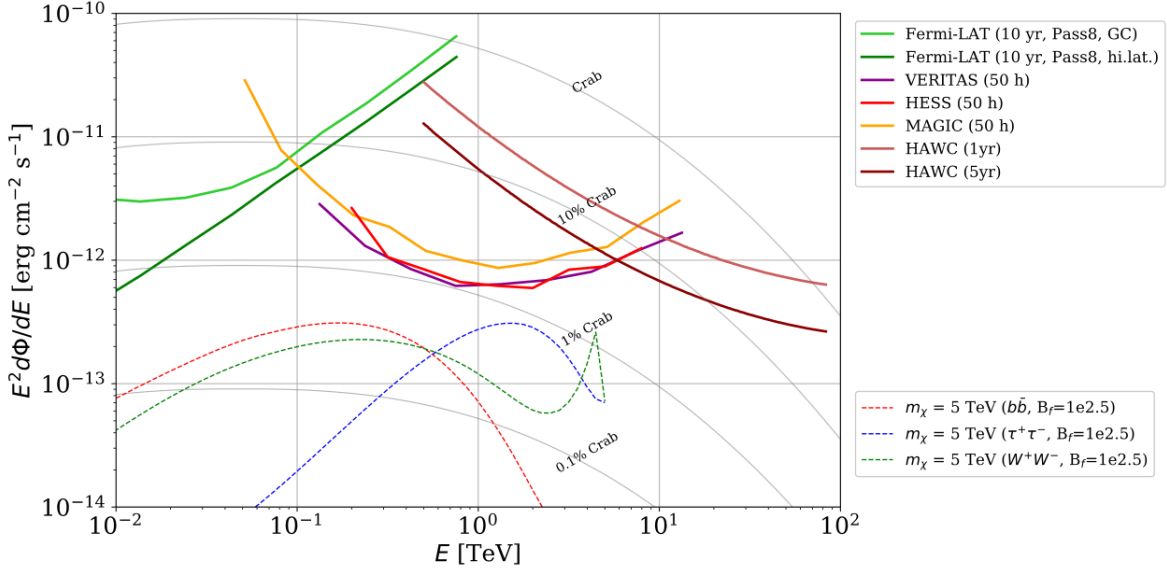


Figure 6.1 Sensitivities of five gamma-ray experiments compared to percentages of the Crab nebula’s emission and dark matter annihilation. Solid lines present estimated sensitivities to power law spectra [FACT CHECK THIS] for each experiment. Green lines are Fermi-LAT sensitivities where lighter green is the sensitivity to the galactic center and dark green is its sensitivity to higher declinations. Orange, red, and purple solid lines represent the MAGIC, HESS, and VERITAS 50 hour sensitivities respectively. The maroon and brown lines are the HAWC 1 year and 5 year sensitivities. Across four decades of gamma-ray energy, these experiments have similar sensitivities on the order 10^{-12} erg $\text{cm}^{-2}\text{s}^{-1}$. The dotted lines are estimated dark matter fluxes assuming $m_\chi = 5$ TeV DM annihilating to bottom quarks (red), tau leptons (blue), and W bosons (green). Faded gray lines outline percentage flux of the Crab nebula. Figure is an augmented version of [25]

696 Sculptor and Carina were between January 2008 and December 2009. HESS’s observations of
 697 Coma Berenices were from 2010 to 2013, and Fornax was observed in 2010 [32, 33, 34]. MAGIC
 698 provided deep observations of Segue1 between 2011 and 2013 [35]. MAGIC also provides data
 699 for three dwarves: Coma Berenices, Draco, and Ursa Major II where observations were made
 700 in: January - June 2019 [36], March - September 2018 [36], and 2014 - 2016 [37] respectively.
 701 VERITAS provided data for Boötes I, Draco, Segue 1, and Ursa Minor from 2009 to 2016 [38].

702 This chapter presents the Glory Duck analysis, the name given for the search for dark matter
 703 annihilation from dSph by combining data from the five gamma-ray observatories: Fermi-LAT,
 704 HAWC, HESS, MAGIC, and VERITAS. Specifically, the methods in analysis and modeling are
 705 presented for the HAWC gamma-ray observatory. This work was published to the Journal of
 706 Cosmology and Astroparticle Physics and presented at the International Cosmic Ray Conference

707 in 2019, 2021, and 2023 [39, 40, 41] and others.

708 **6.2 Dataset and Background**

709 This section enumerates the data and background methods used for HAWC’s study of dSphs.
710 Section 6.2.1 and Section 6.2.2 are most useful for fellow HAWC collaborators looking to replicate
711 the Glory Duck analysis.

712 **6.2.1 Itemized HAWC files**

- 713 • Detector Resolution: `response_aerie_svn_27754_systematics_best_mc_test_no`
714 `broadpulse_10pctlogchargesmearing_0.63qe_25kHzNoise_run5481_curvatu`
715 `re0_index3.root`
- 716 • Data Map: `maps-20180119/liff/maptree_1024.root`
- 717 • Spectral Dictionary: `DM_CirrelliSpectrum_dict_gammas.npy`
- 718 • Analysis wiki: https://private.hawc-observatory.org/wiki/index.php/Glory_Duck_Multi-Experiment_Dark_Matter_Search

720 **6.2.2 Software Tools and Development**

721 This analysis was performed using HAL and 3ML [42, 43] in Python version 2. I built software
722 to implement the *A Poor Particle Physicist Cookbook for Dark Matter Indirect Detection* (PPPC)
723 [44] DM spectral model and dSphs spatial model from [45] for HAWC analysis. A NumPy version
724 of this dictionary was made for both Py2 and Py3. The code base for creating this dictionary is
725 linked on my GitLab sandbox:

- 726 • Py2: [Dictionary Generator \(Deprecated\)](#)
- 727 • Py3: [PPPC2Dict](#)

728 The analysis was performed using the f_{hit} framework performed in the HAWC Crab paper
729 [42]. The Python2 NumPy dictionary file for gamma-ray final states is `dmCirSpecDict.npy`. The
730 corresponding Python3 file is `DM_CirrelliSpectrum_dict_gammas.npy`. These files can also

731 be used for decay channels and the PPPC describes how [44]. All other software used for data
732 analysis, DM profile generation, and job submission to SLURM are also kept in my sandbox for
733 [the Glory Duck](#) project.

734 **6.2.3 Data Set and Background Description**

735 The HAWC data maps used for this analysis contain 1017 days of data between runs 2104
736 (2014-11-26) and 7476 (2017-12-20). They were generated from pass 4.0 reconstruction. The
737 analysis is performed using the f_{hit} energy binning scheme with bins (1-9) similar to what was done
738 for the Crab and previous HAWC dSph analysis [42, 46]. Bin 0 was excluded as it has substantial
739 hadronic contamination and poor angular resolution.

740 This analysis was done on dSphs because of their large DM mass content relative to baryonic
741 mass. We consider the following to estimate the background to this study.

- 742 • The dSphs are small in HAWC’s field of view, so the analysis is not sensitive to large or small
743 scale anisotropies.
- 744 • The dSphs used in this analysis are off the galactic plane.
- 745 • The dSphs are baryonically faint relative to their expected dark matter content and are not
746 expected to contain high energy gamma-ray sources.

747 Therefor we make no additional assumptions on the background from our sources and use
748 HAWC’s standard direct integration method for background estimation [42]. It is possible for
749 gamma rays from DM annihilation to scatter in transit to HAWC via Inverse Compton Scattering
750 (ICS). This was investigated and its impact on the flux is basically zero. Supporting information
751 on this is in Section 6.7.1

752 **6.3 Analysis**

753 The expected differential photon flux from DM-DM annihilation to standard model particles,
754 $d\Phi_\gamma/dE_\gamma$, over solid angle, Ω is described by the familiar equation.

$$\frac{d\Phi_\gamma}{dE_\gamma} = \frac{\langle\sigma v\rangle}{8\pi m_\chi^2} \frac{dN_\gamma}{dE_\gamma} \times \int_{\text{source}} d\Omega \int_{l.o.s} \rho_\chi^2 dl(r, \theta') \quad (6.1)$$

755 Where $\langle \sigma v \rangle$ is the velocity weighted annihilation cross-section. $\frac{dN}{dE}$ is the expected differential
 756 number of photons produced at each energy per annihilation. m_χ is the rest mass of the supposed
 757 DM particle. ρ_χ is the DM density. J is the astrophysical J-factor and is defined as

$$J = \int d\Omega \int_{l.o.s} dl \rho_\chi^2(r, \theta') \quad (6.2)$$

758 l is the distance to the source from Earth. r is the radial distance from the center of the source. θ' is
 759 the half angle defining a cone containing the DM source. How each component is synthesized and
 760 considered for HAWC's analysis is presented in the following sections. Section 6.3.1 presents the
 761 particle physics model for DM annihilation. Section 6.3.2 presents the spatial distributions built
 762 for each dSph.

763 6.3.1 $\frac{dN_\gamma}{dE_\gamma}$ - Particle Physics Component

764 For these spectra, we import the PPPC with Electroweak (EW) corrections [44]. The spectrum
 765 is implemented as a model script in astromodels for 3ML. The EW corrections were previously not
 766 considered for HAWC and are significant for DM annihilating to EW coupled SM particles such
 767 as all leptons, and the γ , Z , and W bosons [46]. Figure 6.2 demonstrates the significance of EW
 768 corrections for W boson annihilation. Across EW SM channels, the gamma-ray spectra become
 769 harder than spectra without EW corrections. Tables from the PPPC were reformatted into Python
 770 NumPy dictionaries for collaboration-wide use. A class in astromodels was developed to include
 771 the EW correction from the PPPC and is aptly named `PPPCSpectra` within `DM_models.py`.

772 6.3.2 J - Astrophysical Component

773 The J-factor profiles for each source are imported from Geringer-Sameth (referred to with \mathcal{GS})
 774 [45]. These were pulled from the publication as $J(\theta)$, where θ is the angular separation from the
 775 center of the source. HAWC requires maps in terms of $\frac{dJ}{d\Omega}$, so the conversion from the maps was
 776 done in the following way...

777 First, convert the angular distances to solid angles

$$\Omega = 2 \cdot \pi(1 - \cos(\theta)) \quad (6.3)$$

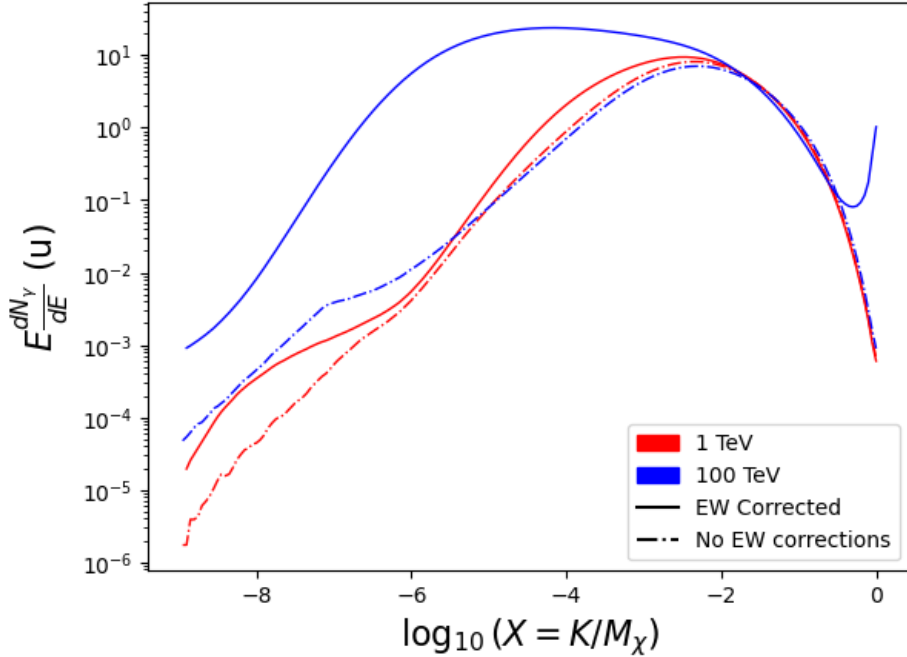


Figure 6.2 Effect of Electroweak (EW) corrections on expected DM annihilation spectrum for $\chi\chi \rightarrow W^-W^+$. Solid lines are spectral models that consider EW corrections. Dash-dot lines are spectral models without EW corrections. Red lines are models for $M_\chi = 1$ TeV. Blue lines represent models for $M_\chi = 100$ TeV. All models are sourced from the PPPC4DMID [44].

778 which reduces with a small angle approximation to $\pi\theta^2$. Next, the central difference for both the
 779 ΔJ and $\Delta\Omega$ value were calculated from the discretized $J(\theta)$ with the central difference stencil:

$$\Delta\phi_i = \phi_{i+1} - \phi_{i-1} \quad (6.4)$$

780 Where ϕ is either Ω or J . These were done separately in case the grid spacing in θ was not uniform.
 781 Finally, these lists are divided so that we are left with an approximation of the $dJ/d\Omega$ profile that
 782 is a function of θ . Admittedly, this is an approximation method for the map which introduces small
 783 errors compared to the true profile estimate. This was checked as a systematic against the author's
 784 profiling of the spatial distribution and is documented in Section 6.8.1.

785 With $\frac{dJ}{d\Omega}(\theta)$, a map is generated, first by filling in the north-east quadrant of the map. This
 786 quadrant is then reflected twice, vertically then horizontally, to fill the full map. Maps are then
 787 normalized by dividing the discrete 2D integral of the map. The 2D integral was a simple height

788 of bins, Newton's integral:

$$p^2 \cdot \sum_{i,j=0}^{N,M} \frac{dJ}{d\Omega}(\theta_{i,j}, \phi_{i,j}) \quad (6.5)$$

789 These maps are HEALpix maps with NSIDE 16384 and saved in the `.fits` format.

790 Another DM spatial distribution model from Bonnivard (\mathcal{B}) [47] was used for the Glory Duck
791 study. However, to save computational time, limits from \mathcal{GS} were scaled to \mathcal{B} instead of each
792 experiment performing a full study a second time. How these models compare is demonstrated
793 for each dSph in Figure 6.16 and Figure 6.17 Plots of these maps are provided for each source
794 in chapter A Examples of the two most impactful dSphs derived from \mathcal{GS} , Segue1 and Coma
795 Berenices are featured in Figure 6.3

796 **6.3.3 Source Selection and Annihilation Channels**

797 We use many of the dSphs presented in HAWC's previous dSph DM search [46]. HAWC's
798 sources for Glory Duck include Boötes I, Coma Berenices, Canes Venatici I + II, Draco, Hercules,
799 Leo I, II, + IV, Segue 1, Sextans, and Ursa Major I + II. A full description of all sources used
800 in Glory Duck is found in Table 6.1. Triangulum II was excluded from the Glory Duck analysis
801 because of large uncertainties in its J factor. Ursa Minor was excluded from HAWC's contribution
802 to the combination because the source extension model extended Ursa Minor beyond HAWC's field
803 of view. Ursa Minor was not expected to contribute significantly to the combined limit, so work
804 was not invested in a solution to include Ursa Minor.

805 This analysis improves on the previous HAWC dSph paper [46] in the following ways. Pre-
806 viously, the dSphs were treated and implemented as point sources. For this analysis, dSphs are
807 modeled and treated as extended source. The impact of this change with respect to the upper limit
808 is source dependent and is explored in Section 6.7.2. Previously, the particle physics model used for
809 gamma-ray spectra from DM annihilation did not have EW corrections where the PPPC includes
810 them. Finally, the gamma-ray ray dataset is much larger. The study performed here analyzes over
811 1000 days of data compared to 507.

812 The SM annihilation channels probed for the Glory Duck combination include $b\bar{b}$, $e\bar{e}$, $\mu\bar{\mu}$, $\tau\bar{\tau}$,
813 $t\bar{t}$, W^+W^- , and ZZ . A summary of all sources, with a description of each experiments' sensitivity

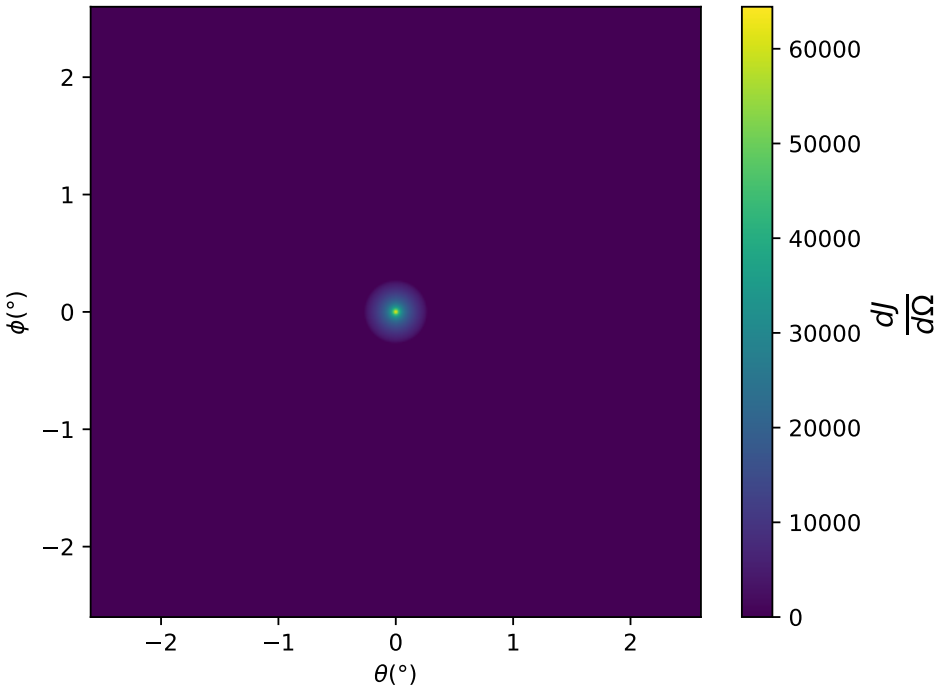
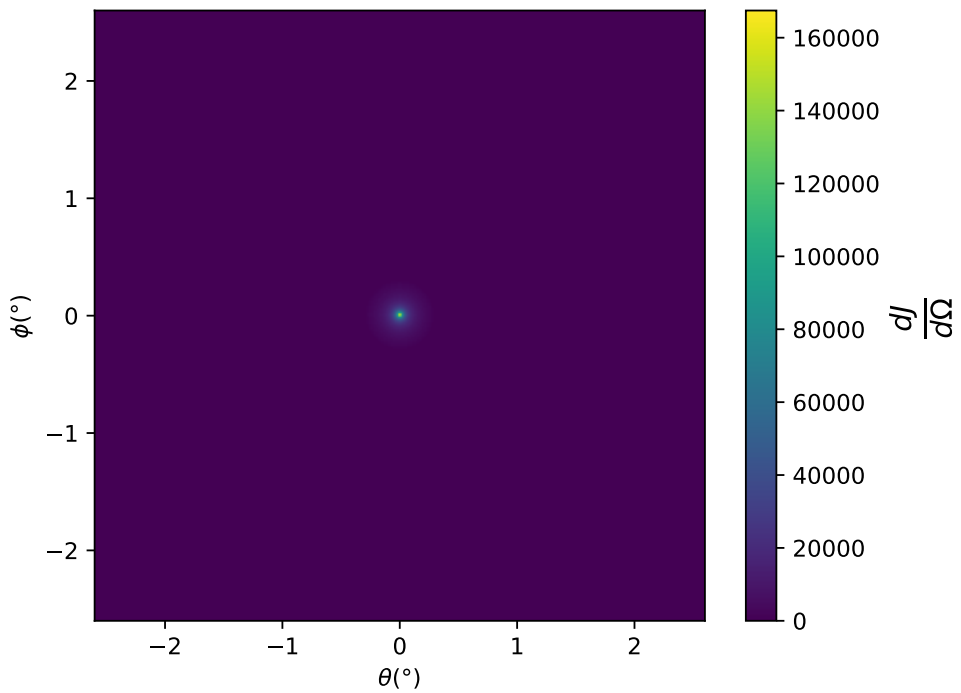


Figure 6.3 $\frac{dJ}{d\Omega}$ maps for Segue1 (top) and Coma Berenices (bottom). Origin is centered on the specific dwarf spheroidal galaxies (dSph). X and Y axes are the angular separation from the center of the dwarf. Plots of the remaining 11 dSph HAWC studied are linked in Fig. A.1.

Table 6.1 Summary of the relevant properties of the dSphs used in the present work. Column 1 lists the dSphs. Columns 2 and 3 present their heliocentric distance and galactic coordinates, respectively. Columns 4 and 5 report the J -factors of each source given from the \mathcal{GS} and \mathcal{B} independent studies and their estimated $\pm 1\sigma$ uncertainties. The values $\log_{10} J$ (\mathcal{GS} set) [45] correspond to the mean J -factor values for a source extension truncated at the outermost observed star. The values $\log_{10} J$ (\mathcal{B} set) [47] are provided for a source extension at the tidal radius of each dSph. **Bolded sources are within HAWC's field of view and provided to the Glory Duck analysis.**

Name	Distance (kpc)	l, b ($^{\circ}$)	$\log_{10} J$ (\mathcal{GS} set) $\log_{10}(\text{GeV}^2 \text{cm}^{-5} \text{sr})$	$\log_{10} J$ (\mathcal{B} set) $\log_{10}(\text{GeV}^2 \text{cm}^{-5} \text{sr})$
Boötes I	66	358.08, 69.62	$18.24^{+0.40}_{-0.37}$	$18.85^{+1.10}_{-0.61}$
Canes Venatici I	218	74.31, 79.82	$17.44^{+0.37}_{-0.28}$	$17.63^{+0.50}_{-0.20}$
Canes Venatici II	160	113.58, 82.70	$17.65^{+0.45}_{-0.43}$	$18.67^{+1.54}_{-0.97}$
Carina	105	260.11, -22.22	$17.92^{+0.19}_{-0.11}$	$18.02^{+0.36}_{-0.15}$
Coma Berenices	44	241.89, 83.61	$19.02^{+0.37}_{-0.41}$	$20.13^{+1.56}_{-1.08}$
Draco	76	86.37, 34.72	$19.05^{+0.22}_{-0.21}$	$19.42^{+0.92}_{-0.47}$
Fornax	147	237.10, -65.65	$17.84^{+0.11}_{-0.06}$	$17.85^{+0.11}_{-0.08}$
Hercules	132	28.73, 36.87	$16.86^{+0.74}_{-0.68}$	$17.70^{+1.08}_{-0.73}$
Leo I	254	225.99, 49.11	$17.84^{+0.20}_{-0.16}$	$17.93^{+0.65}_{-0.25}$
Leo II	233	220.17, 67.23	$17.97^{+0.20}_{-0.18}$	$18.11^{+0.71}_{-0.25}$
Leo IV	154	265.44, 56.51	$16.32^{+1.06}_{-1.70}$	$16.36^{+1.44}_{-1.65}$
Leo V	178	261.86, 58.54	$16.37^{+0.94}_{-0.87}$	$16.30^{+1.33}_{-1.16}$
Leo T	417	214.85, 43.66	$17.11^{+0.44}_{-0.39}$	$17.67^{+1.01}_{-0.56}$
Sculptor	86	287.53, -83.16	$18.57^{+0.07}_{-0.05}$	$18.63^{+0.14}_{-0.08}$
Segue I	23	220.48, 50.43	$19.36^{+0.32}_{-0.35}$	$17.52^{+2.54}_{-2.65}$
Segue II	35	149.43, -38.14	$16.21^{+1.06}_{-0.98}$	$19.50^{+1.82}_{-1.48}$
Sextans	86	243.50, 42.27	$17.92^{+0.35}_{-0.29}$	$18.04^{+0.50}_{-0.28}$
Ursa Major I	97	159.43, 54.41	$17.87^{+0.56}_{-0.33}$	$18.84^{+0.97}_{-0.43}$
Ursa Major II	32	152.46, 37.44	$19.42^{+0.44}_{-0.42}$	$20.60^{+1.46}_{-0.95}$
Ursa Minor	76	104.97, 44.80	$18.95^{+0.26}_{-0.18}$	$19.08^{+0.21}_{-0.13}$

814 to the source, is provided in Table 6.2.

815 6.4 Likelihood Methods

816 6.4.1 HAWC Likelihoods

817 For every analysis bin in energy, f_{hit} bins (1-9), and location, we can expect N signal events and
818 B background events. The expected number of excess signal events from dark matter annihilation,

Table 6.2 Summary of dSph observations by each experiment used in this work. A ‘-’ indicates the experiment did not observe the dSph for this study. For Fermi-LAT, the exposure at 1 GeV is given. For HAWC, $|\Delta\theta|$ is the absolute difference between the source declination and HAWC latitude. HAWC is more sensitive to sources with smaller $|\Delta\theta|$. For IACTs, we show the zenith angle range, the total exposure, the energy range, the angular radius θ of the signal or ON region, the ratio of exposures between the background-control (OFF) and signal (ON) regions (τ), and the significance of gamma-ray excess in standard deviations, σ .

Source name	Fermi-LAT	HAWC	H.E.S.S, MAGIC, VERITAS						
	Exposure (10^{11} s m 2)	$ \Delta\theta $ (°)	IACT	Zenith (°)	Exposure (h)	Energy range (GeV)	θ (°)	τ	S (σ)
Boötes I	2.6	4.5	VERITAS	15 – 30	14.0	100–41000	0.10	8.6	-1.0
Canes Venatici I	2.9	14.6	–	–	–	–	–	–	–
Canes Venatici II	2.9	15.3	–	–	–	–	–	–	–
Carina	3.1	–	H.E.S.S.	27 – 46	23.7	310 – 70000	0.10	18.0	-0.3
Coma Berenices	2.7	4.9	H.E.S.S.	47 – 49	11.4	550 – 70000	0.10	14.4	-0.4
Draco	3.8	38.1	MAGIC	5 – 37	49.5	60 – 10000	0.17	1.0	–
			MAGIC	29 – 45	52.1	70 – 10000	0.22	1.0	–
			VERITAS	25 – 40	49.8	120 – 70000	0.10	9.0	-1.0
Fornax	2.7	–	H.E.S.S.	11 – 25	6.8	230 – 70000	0.10	45.5	-1.5
Hercules	2.8	6.3	–	–	–	–	–	–	–
Leo I	2.5	6.7	–	–	–	–	–	–	–
Leo II	2.6	3.1	–	–	–	–	–	–	–
Leo IV	2.4	19.5	–	–	–	–	–	–	–
Leo V	2.4	–	–	–	–	–	–	–	–
Leo T	2.6	–	–	–	–	–	–	–	–
Sculptor	2.7	–	H.E.S.S.	10 – 46	11.8	200 – 70000	0.10	19.8	-2.2
Segue I	2.5	2.9	MAGIC	13 – 37	158.0	60 – 10000	0.12	1.0	-0.5
			VERITAS	15 – 35	92.0	80 – 50000	0.10	7.6	0.7
Segue II	2.7	–	–	–	–	–	–	–	–
Sextans	2.4	20.6	–	–	–	–	–	–	–
Ursa Major I	3.4	32.9	–	–	–	–	–	–	–
Ursa Major II	4.0	44.1	MAGIC	35 – 45	94.8	120 – 10000	0.30	1.0	-2.1
Ursa Minor	4.1	–	VERITAS	35 – 45	60.4	160 – 93000	0.10	8.4	-0.1

819 S , is estimated by convolving Equation (6.1) with HAWC's energy response and pixel point spread
 820 functions. I then compute the test statistic (TS) with the log-likelihood ratio test,

$$\text{TS} = -2 \ln \left(\frac{\mathcal{L}_0}{\mathcal{L}^{\max}} \right) \quad (6.6)$$

822 where \mathcal{L}_0 is the null hypothesis, or no DM emission, likelihood. \mathcal{L}^{\max} is the best fit signal
 823 hypothesis where $\langle \sigma v \rangle$ maximizes the likelihood. We calculate the likelihood of each source and
 824 model, assuming events are Poisson distributed, with

$$\mathcal{L} = \prod_i \frac{(B_i + S_i)^{N_i} e^{-(B_i + S_i)}}{N_i!} \quad (6.7)$$

825 where S_i is the sum of expected number of signal counts. B_i is the number of background counts
 826 observed. N_i is the total number of counts.

827 I also calculate an upper limit on $\langle \sigma v \rangle$ by calculating the 95% confidence level (CL). For the
 828 CL, we define a parameter, TS_{95} , as

$$\text{TS}_{95} \equiv \sum_{\text{bins}} \left[2N \ln \left(1 + \frac{\epsilon S_{\text{ref}}}{B} \right) - 2\epsilon S_{\text{ref}} \right] \quad (6.8)$$

829 where the expected signal counts from a dSph is scaled by ϵ . S_{ref} is the expected number of excess
 830 counts in a bin from DM emission from a dSph with a corresponding annihilation cross-section,
 831 $\langle \sigma v \rangle$. We scan ϵ such that

$$2.71 = \text{TS}_{\max} - \text{TS}_{95} \quad (6.9)$$

832 6.4.2 Glory Duck Joint Likelihood

833 The joint likelihood for the 5-experiment combination was done similarly as Section 6.4.1. We
 834 calculate upper limits on $\langle \sigma v \rangle$ from the TS, Eq. (6.6), and define the likelihood ratio more generally

$$\lambda(\langle \sigma v \rangle | \mathcal{D}_{\text{dSphs}}) = \frac{\mathcal{L}(\langle \sigma v \rangle; \hat{\nu} | \mathcal{D}_{\text{dSphs}})}{\mathcal{L}(\widehat{\langle \sigma v \rangle}; \hat{\nu} | \mathcal{D}_{\text{dSphs}})} \quad (6.10)$$

835 $\mathcal{D}_{\text{dSphs}}$ is the totality of observations across experiments and dSphs. ν are the nuisance parameters
 836 which are the J factors in this study. $\widehat{\langle \sigma v \rangle}$ and $\hat{\nu}$ are the respective estimate that maximize \mathcal{L}
 837 globally. Finally, $\hat{\nu}$ is the set of nuisance parameters that maximize \mathcal{L} for a fixed value of $\langle \sigma v \rangle$.

838 The *complete* joint likelihood, \mathcal{L} that encompasses all observations from all instruments and
 839 dSphs can be factorized into *partial* functions for each dSph l (with $\mathcal{L}_{\text{dSph},l}$) and its J factor (\mathcal{J}_l):

$$\mathcal{L}(\langle\sigma v\rangle; \nu | \mathcal{D}_{\text{dSphs}}) = \prod_{l=1}^{N_{\text{dSphs}}} \mathcal{L}_{\text{dSph},l}(\langle\sigma v\rangle; J_l, \nu_l | \mathcal{D}_l) \times \mathcal{J}_l(J_l | J_{l,\text{obs}}, \sigma_{\log J_l}). \quad (6.11)$$

840 For this study, $N_{\text{dSphs}} = 20$ is the number of dSphs studied. \mathcal{D}_l are the gamma-ray observations
 841 of dSph, l . ν_l are the nuisance parameters modifying the gamma-ray observations of dSph, l ,
 842 but excludes \mathcal{J}_l . \mathcal{J}_l is the J factor for dSph, l , as defined in Equation (6.2), and it is a nuisance
 843 parameter whose value is unknown. $\log_{10} J_{l,\text{obs}}$ and $\sigma_{\log J_l}$ are obtained from fitting a log-normal
 844 function of $J_{l,\text{obs}}$ to the posterior distribution of J_l [48]. $\log_{10} J_{l,\text{obs}}$ and $\sigma_{\log J_l}$ values are provided
 845 in Table 6.1. The term \mathcal{J}_l constraining J_l is written as:

$$\mathcal{J}_l(J_l | J_{l,\text{obs}}, \sigma_{\log J_l}) = \frac{1}{\ln(10)J_{l,\text{obs}}\sqrt{2\pi}\sigma_{\log J_l}} \exp\left(-\frac{(\log_{10} J_l - \log_{10} J_{l,\text{obs}})^2}{2\sigma_{\log J_l}^2}\right). \quad (6.12)$$

846 Both the \mathcal{GS} and \mathcal{B} , displayed in Table 6.1, sets of J factors are used in this analysis. Equation (6.12)
 847 is also normalized, so it can also be interpreted as a probability density function (PDF) for $J_{l,\text{obs}}$.
 848 From Equation (6.1), we can also see that $\langle\sigma v\rangle$ and J_l are degenerate when computing $\mathcal{L}_{\text{dSph},l}$.
 849 Therefore, as noted in [49], it is sufficient to compute $\mathcal{L}_{\text{dSph},l}$ versus $\langle\sigma v\rangle$ for a fixed value of J_l .
 850 We used $J_{l,\text{obs}}(\mathcal{GS})$ reported in Tab. 6.1, in order to perform the profile of \mathcal{L} with respect to J_l .
 851 The degeneracy implies that for any $J'_l \neq J_{l,\text{obs}}$ (in practice in our case we used $J'_l = J_{l,\text{obs}}(\mathcal{B})$ to
 852 compute results from a different set of J factors):

$$\mathcal{L}_{\text{dSph},l}(\langle\sigma v\rangle; J'_l, \nu_l | \mathcal{D}_l) = \mathcal{L}_{\text{dSph},l}\left(\frac{J'_l}{J_{l,\text{obs}}}\langle\sigma v\rangle; J_{l,\text{obs}}, \nu_l | \mathcal{D}_l\right), \quad (6.13)$$

853 which is a straightforward rescaling operation that reduces the computational needs of the profiling
 854 operation since:

$$\mathcal{L}(\langle\sigma v\rangle; \hat{\nu} | \mathcal{D}_{\text{dSphs}}) = \prod_{l=1}^{N_{\text{dSphs}}} \max_{J_l} \left[\mathcal{L}_{\text{dSph},l}(\langle\sigma v\rangle; J_l, \hat{\nu}_l | \mathcal{D}_l) \times \mathcal{J}_l(J_l | J_{l,\text{obs}}, \sigma_{\log J_l}) \right]. \quad (6.14)$$

855 In addition, Eq. (6.13) enables the combination of data from different gamma-ray instruments and
 856 observed dSphs via tabulated values of $\mathcal{L}_{\text{dSph},l}$, or equivalently of λ from Eq. (6.10) as was done in

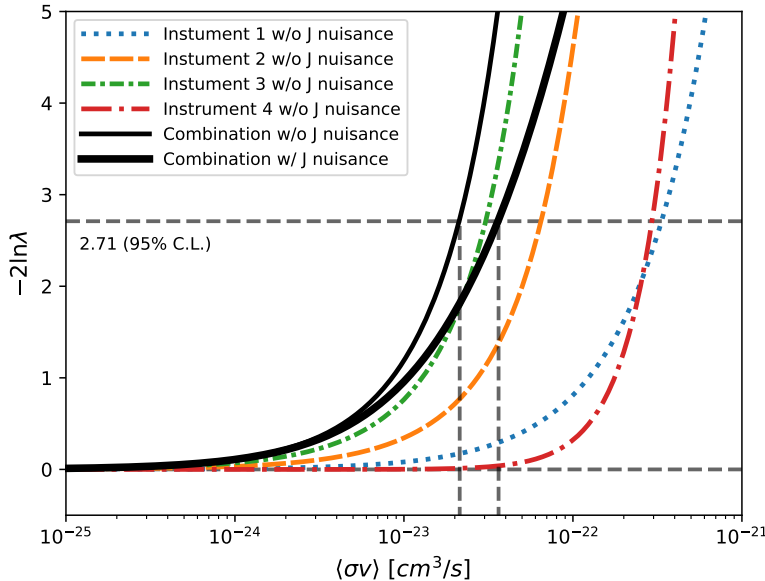


Figure 6.4 Illustration of the combination technique showing a comparison between $-2 \ln \lambda$ provided by four instruments (colored lines) from the observation of the same dSph without any J nuisance and their sum, *i.e.* the resulting combined likelihood (thin black line). According to the test statistics of Equation (6.6), the intersection of the likelihood profiles with the line $-2 \ln \lambda = 2.71$ indicates the 95% C.L. upper limit on $\langle \sigma v \rangle$. The combined likelihood (thin black line) shows a smaller value of upper limit on $\langle \sigma v \rangle$ than those derived by individual instruments. We also show how the uncertainties on the J factor effects the combined likelihood and degrade the upper limit on $\langle \sigma v \rangle$ (thick black line). All likelihood profiles are normalized so that the global minimum $\widehat{\langle \sigma v \rangle}$ is 0. We note that each profile depends on the observational conditions in which a target object was observed. The sensitivity of a given instrument can be degraded and the upper limits less constraining if the observations are performed in non-optimal conditions such as a high zenith angle or a short exposure time.

857 this work, versus $\langle \sigma v \rangle$. $\mathcal{L}_{dSph,l}$ is computed for a fixed value of J_l and profiled with respect to all
 858 instrumental nuisance parameters ν_l , these nuisance parameters are discussed in more detail below.
 859 These values are produced by each detector independently and therefore there is no need to share
 860 sensitive low-level information used to produce them, such as event lists. Figure 6.4 illustrates the
 861 multi-instrument combination technique used in this study with a comparison of the upper limit
 862 on $\langle \sigma v \rangle$ obtained from the combination of the observations of four experiments towards one dSph
 863 versus the upper limit from individual instruments. It also shows graphically the effect of the
 864 J -factor uncertainty on the combined observations.

865 The *partial* joint likelihood function for gamma-ray observations of each dSph ($\mathcal{L}_{dSph,l}$) is

written as the product of the likelihood terms describing the $N_{\text{exp},l}$ observations performed with any of our observatories:

$$\mathcal{L}_{\text{dSph},l} (\langle \sigma v \rangle; J_l, \nu_l | \mathcal{D}_l) = \prod_{k=1}^{N_{\text{exp},l}} \mathcal{L}_{lk} (\langle \sigma v \rangle; J_l, \nu_{lk} | \mathcal{D}_{lk}), \quad (6.15)$$

where each \mathcal{L}_{lk} term refers to an observation of the l -th dSph with associated k -th instrument responses. $N_{\text{exp},l}$ varies from dSph to dSph and can be inferred from Table 6.2.

Each collaboration separately analyzes their data for \mathcal{D}_{lk} corresponding to dSph l and gamma-ray detector k , using as many common assumptions as possible in the analysis. HAWC’s treatment was described earlier in Section 6.4.1 whereas the specifics of the remaining experiments is left to the publication. We compute the values for the likelihood functions \mathcal{L}_{lk} (see Eq. (6.15)) for a fixed value of J_l and profile over the rest of the nuisance parameters ν_{lk} . Then, values of λ from Eq. (6.10) are computed as a function of $\langle \sigma v \rangle$, and shared using a common format. Results are computed for seven annihilation channels, W^+W^- , ZZ , $b\bar{b}$, $t\bar{t}$, e^+e^- , $\mu^+\mu^-$, and $\tau^+\tau^-$ over 62 m_χ values between 5 GeV and 100 TeV provided in [44]. The $\langle \sigma v \rangle$ range is defined between 10^{-28} and $10^{-18} \text{cm}^3 \cdot \text{s}^{-1}$, with 1001 logarithmically spaced values. The likelihood combination, i.e. Equation (6.11), and profile over the J -factor to compute the profile likelihood ratio λ , Equation (6.10), are carried out with two different public analysis software packages, namely `gLike` [50] and `LklCom` [51], that provide the same results [52].

As mentioned previously, each experiment computes the \mathcal{L}_{lk} from Equation (6.10) differently. The remainder of this section highlights the differences in this calculation across the experiments. Four experiments, namely *Fermi*-LAT, H.E.S.S., HAWC and MAGIC, use a binned likelihood to compute the \mathcal{L}_{lk} . For these experiments, for each observation \mathcal{D}_{lk} of a given dSph l carried out using a given gamma-ray detector k , the binned likelihood function is:

$$\mathcal{L}_{lk} (\langle \sigma v \rangle; J_l, \nu_{lk} | \mathcal{D}_{lk}) = \prod_{i=1}^{N_E} \prod_{j=1}^{N_P} \left[\mathcal{P}(s_{lk,ij}(\langle \sigma v \rangle, J_l, \nu_{lk}) + b_{lk,ij}(\nu_{lk}) | N_{lk,ij}) \right] \times \mathcal{L}_{lk,\nu} (\nu_{lk} | \mathcal{D}_{\nu_{lk}}) \quad (6.16)$$

where N_E and N_P are the number of considered bins in reconstructed energy and arrival direction, respectively; \mathcal{P} represents a Poisson PDF for the number of gamma-ray candidate events $N_{lk,ij}$

889 observed in the i -th bin in energy and j -th bin in arrival direction, when the expected number is
 890 the sum of the expected mean number of signal events s_{ij} (produced by DM annihilation) and of
 891 background events b_{ij} ; $\mathcal{L}_{lk,\nu}$ is the likelihood term for the extra ν_{lk} nuisance parameters that vary
 892 from one instrument k to another. The expected counts for signal events s_{ij} for a given dSph l and
 893 detector k is given by:

$$s_{ij}(\langle\sigma\nu\rangle, J) = \int_{E'_{\min,i}}^{E'_{\max,i}} dE' \int_{P'_{\min,j}}^{P'_{\max,j}} d\Omega' \int_0^\infty dE \int_{\Delta\Omega_{tot}} d\Omega \int_0^{T_{\text{obs}}} dt \frac{d^2\Phi(\langle\sigma\nu\rangle, J)}{dEd\Omega} \text{IRF}(E', P' | E, P, t) \quad (6.17)$$

894 where E' and E are the reconstructed and true energies, P' and P the reconstructed and true
 895 arrival directions; $E'_{\min,i}$, $P'_{\min,j}$, $E'_{\max,i}$, and $P'_{\max,j}$ are their lower and upper limits of the i -th
 896 energy bin and the j -th arrival direction bin; T_{obs} is the (dead-time corrected) total observation
 897 time; t is the time along the observations; $d^2\Phi/dEd\Omega$ is the DM flux in the source region (see
 898 Equation (6.1)); and $\text{IRF}(E', P' | E, P, t)$ is the IRF, which can be factorized as the product of the
 899 effective collection area of the detector $A_{\text{eff}}(E, P, t)$, the PDFs for the energy estimator $f_E(E' | E, t)$,
 900 and arrival direction $f_P(P' | E, P, t)$ estimators. Note that for Fermi-LAT, HAWC, MAGIC, and
 901 VERITAS the effect of the finite angular resolution is taken into account through the convolution
 902 of $d\Phi/dEd\Omega$ with f_P in Equation (6.17), whereas in the cases of H.E.S.S. f_P is approximated by a
 903 delta function. This approximation has been made in order to maintain compatibility of the result
 904 with what has been previously published. The difference introduced by this approximation is $< 5\%$
 905 for all considered dSphs. A more comprehensive review of the differences between the analyses of
 906 different instruments can be found in [25].

907 6.5 HAWC Results

908 13 of the 20 dSphs considered for the Glory Duck analysis are within HAWC's field of view.
 909 These dSph are analyzed for emission from DM annihilation according to the likelihood method
 910 described in Section 6.4. The 13 likelihood profiles are then stacked to synthesize a combined
 911 limit on the dark matter cross-section, $\langle\sigma\nu\rangle$. This combination is done for the 7 SM annihilation
 912 channels used in the Glory Duck analysis. Figure 6.5 shows the combined limit for all annihilation
 913 channels with HAWC only observations. We also perform 300 studies of Poisson trials on the

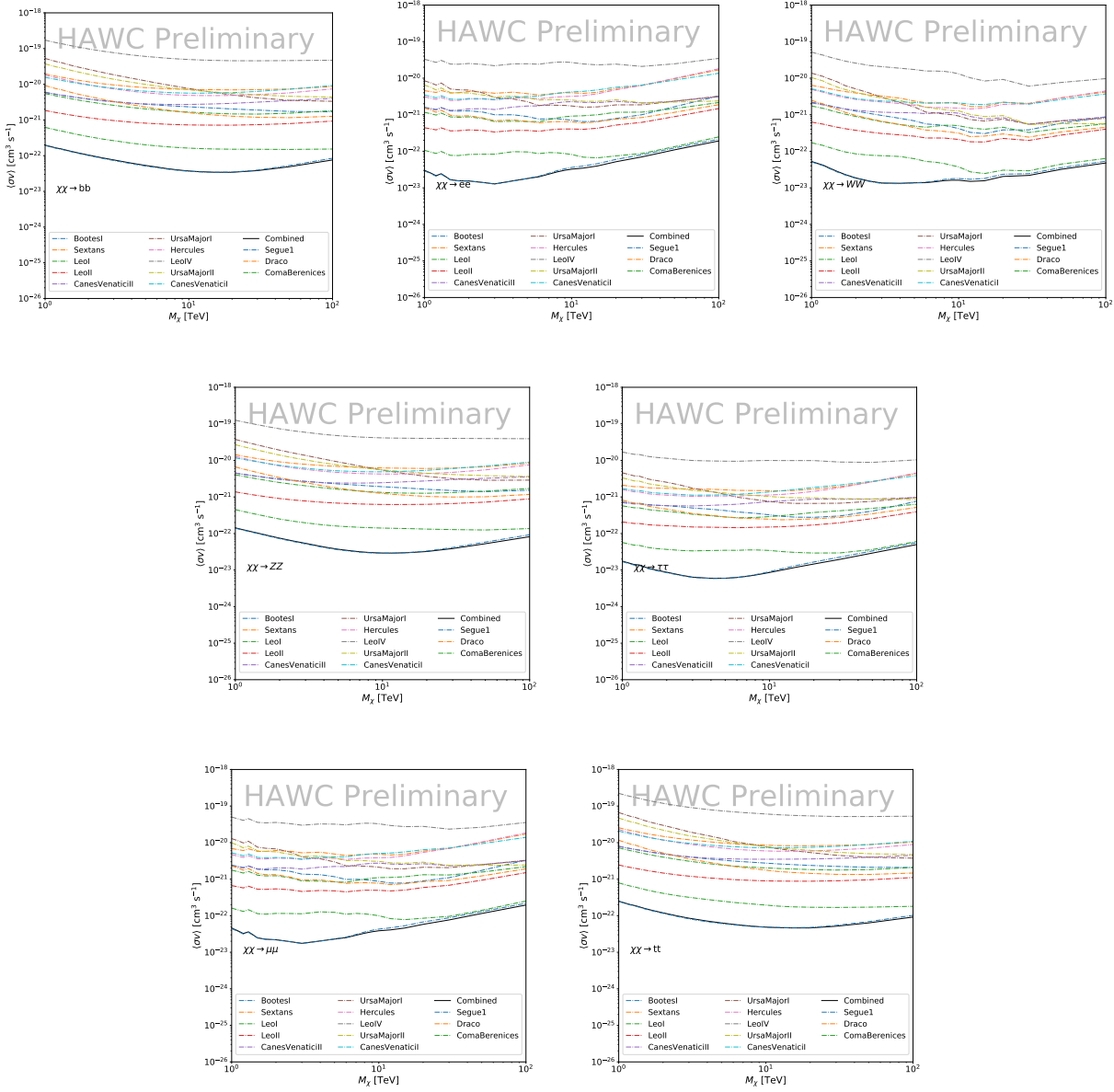


Figure 6.5 HAWC upper limits at 95% confidence level on $\langle\sigma v\rangle$ versus DM mass for seven annihilation channels, using the set of J -factors from Ref. [53]. The solid line represents the observed combined limit. Dashed lines represent limits from individual dSphs.

background. These trials are used to produce HAWC Brazil bands which were shared with the other collaborators for combined Brazil Bands. The results on fitting to HAWC's Poisson trials of the DM hypothesis is shown in Figure 6.7 for all the DM annihilation channels studied for Glory Duck.

No DM was found in HAWC observations. HAWC's limits are dominated by the dSphs Segue1

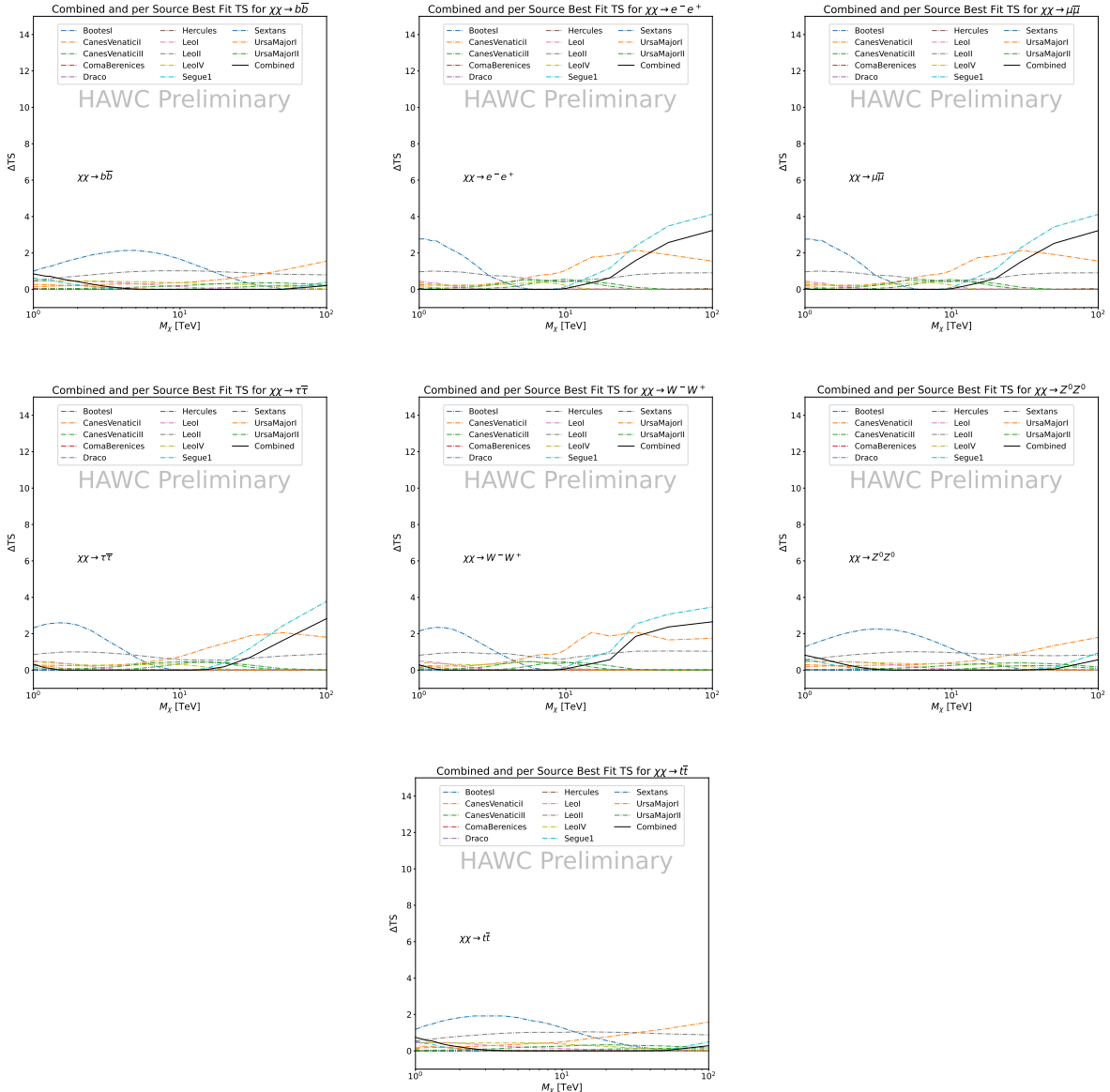


Figure 6.6 HAWC TS values for best fit $\langle \sigma v \rangle$ versus m_χ for seven SM annihilation channels with J factors from \mathcal{GS} . The solid black line shows the combined best fit TS values. The colored, dashed lines are the TS values for each of the 13 sources HAWC studied.

and Coma Berenices. The remaining 11 dSphs do not contribute significantly to the limit because they are at high zenith and/or have much smaller J factors. Even though some remaining dSphs have large J factors, they are towards the edge of HAWC's field of view where HAWC analysis is less sensitive.

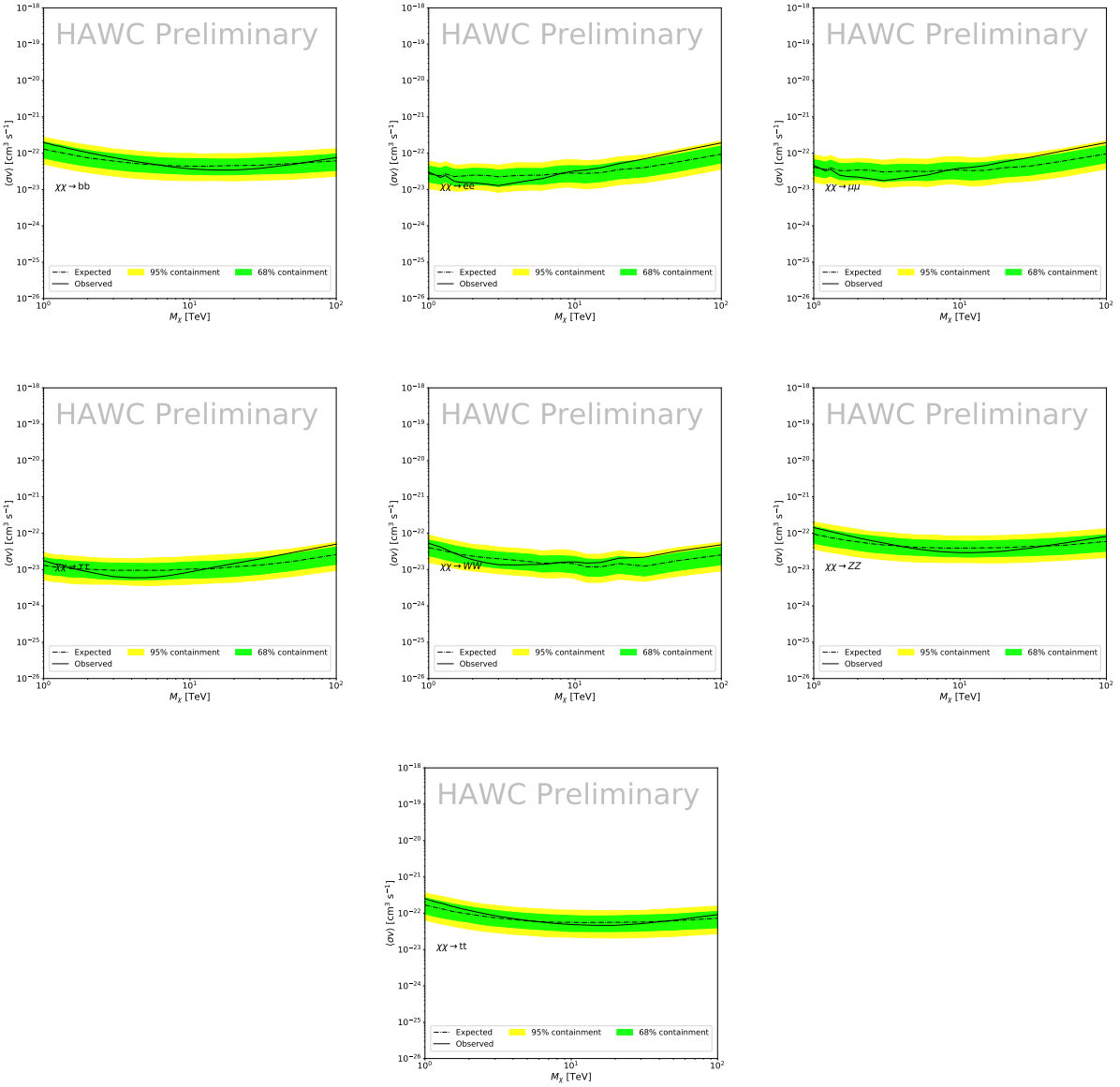


Figure 6.7 HAWC Brazil bands at 95% confidence level on $\langle\sigma v\rangle$ versus DM mass for seven annihilation channels with J -factors from GS [53]. The solid line represents the combined limit from 13 dSphs. The dashed line is the expected limit. The green band is the 68% containment. The yellow band is the 95% containment.

923 6.6 Glory Duck Combined Results

924 The crux of this analysis is that HAWC's results are combined with 4 other gamma-ray observa-
 925 tories: Fermi-LAT, H.E.S.S., MAGIC, and VERITAS. No significant DM emission was observed
 926 by any of the five instruments. We present the upper limits on $\langle\sigma v\rangle$ assuming seven independent
 927 DM self annihilation channels, namely W^+W^- , Z^+Z^- , $b\bar{b}$, $t\bar{t}$, e^+e^- , $\mu^+\mu^-$, and $\tau^+\tau^-$. The 68%

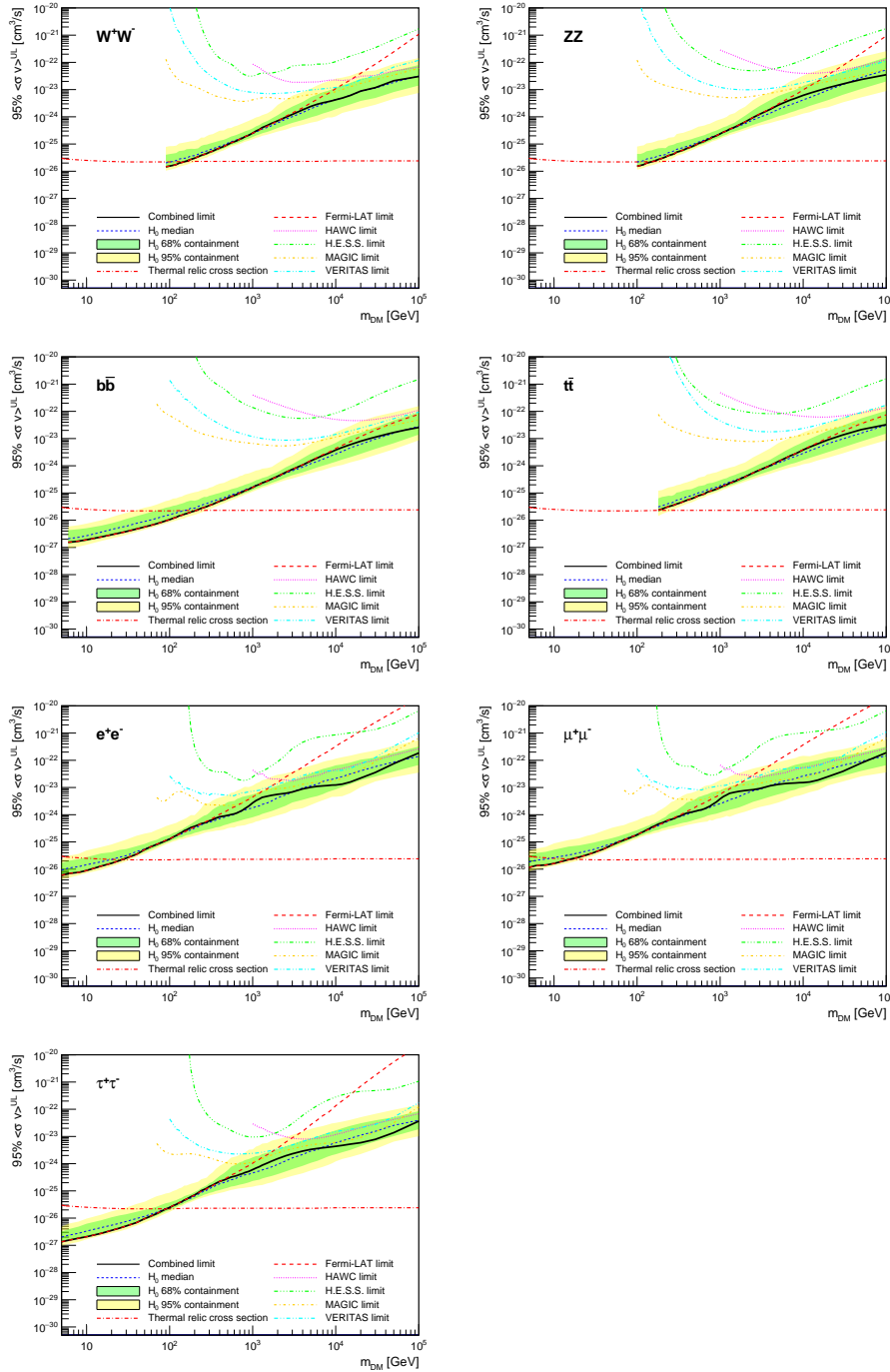


Figure 6.8 Upper limits at 95% confidence level on $\langle\sigma v\rangle$ in function of the DM mass for eight annihilation channels, using the set of J factors from Ref. [53] (\mathcal{GS} set in Table 6.1). The black solid line represents the observed combined limit, the black dashed line is the median of the null hypothesis corresponding to the expected limit, while the green and yellow bands show the 68% and 95% containment bands. Combined upper limits for each individual detector are also indicated as solid, colored lines. The value of the thermal relic cross-section in function of the DM mass is given as the red dotted-dashed line [54].

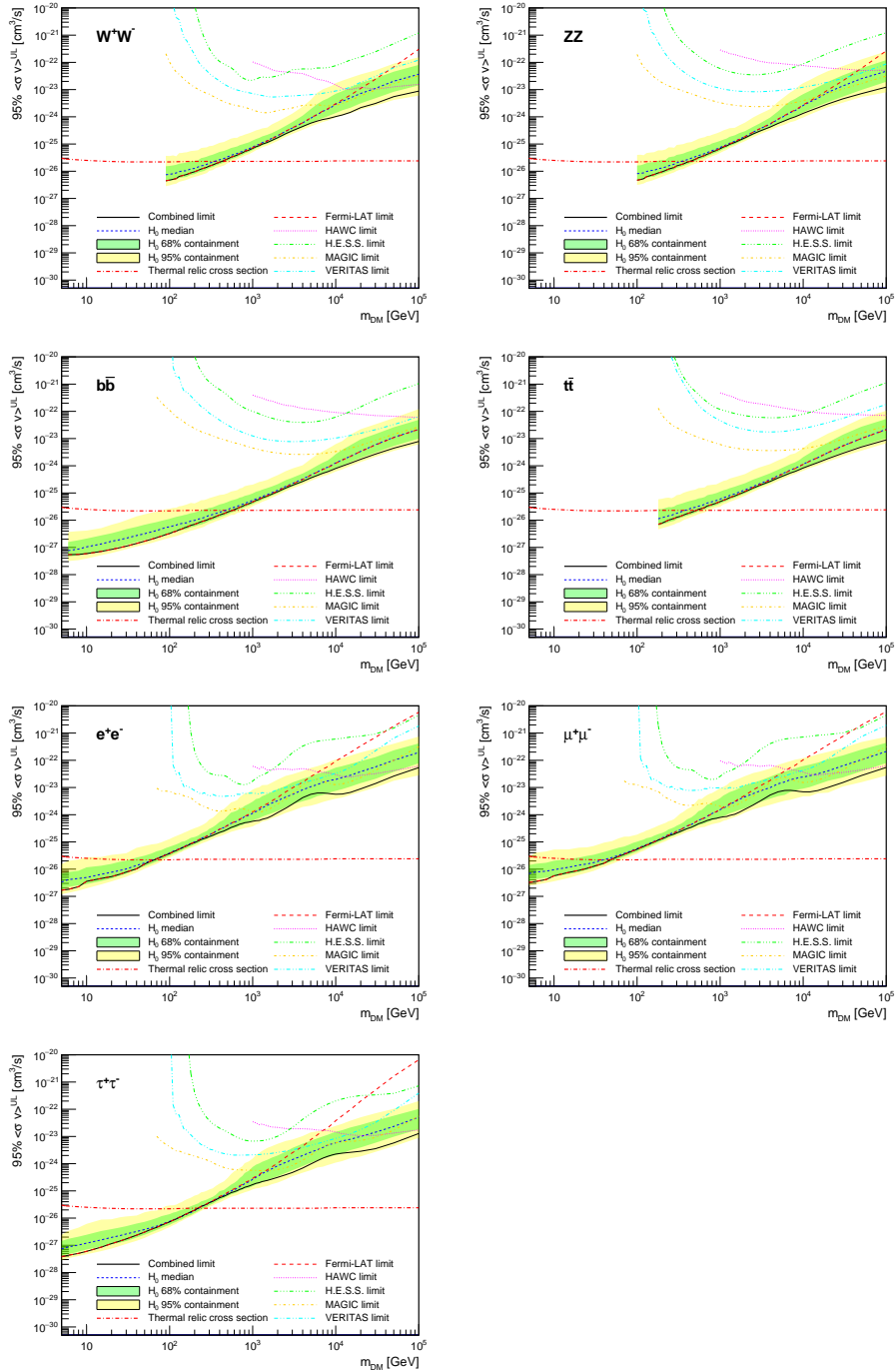


Figure 6.9 Same as Fig. 6.8, using the set of J factors from Ref. [47, 55] (\mathcal{B} set in Table 6.1).

and 95% containment bands are produced from 300 Poisson realizations of the null hypothesis corresponding to each of the combined datasets. These 300 realizations are combined identically to dSph observations. The containment bands and the median are extracted from the distribution of resulting limits on the null hypothesis. These 300 realizations are obtained either by fast simu-

932 lations of the OFF observations, for H.E.S.S., MAGIC, VERITAS, and HAWC, or taken from real
933 observations of empty fields of view in the case of Fermi-LAT [48, 56, 57].

934 The obtained limits are shown in Figure 6.8 for the $\mathcal{G}\mathcal{S}$ set of J -factors [53] and in Figure 6.9
935 for the \mathcal{B} set of J -factors [47, 55]. The combined limits are presented with their 68% and 95%
936 containment bands, and are expected to be close to the median limit when no signal is present.
937 We observe agreement with the null hypothesis for all channels, within 2σ standard deviations,
938 between the observed limits and the expectations given by the median limits. Limits obtained from
939 each detector are also indicated in the figures, where limits for all dSphs observed by the specific
940 instrument have been combined.

941 Below ~ 300 GeV, the *Fermi*-LAT dominates the DM limits for all annihilation channels. From
942 ~ 300 GeV to ~ 2 TeV, *Fermi*-LAT continues to dominate for the hadronic and bosonic DM channels,
943 yet the IACTs (H.E.S.S., MAGIC, and VERITAS) and *Fermi*-LAT all contribute to the limit for
944 leptonic DM channels. For DM masses between ~ 2 TeV to ~ 10 TeV, the IACTs dominate leptonic
945 DM annihilation channels, whereas both the *Fermi*-LAT and the IACTs dominate bosonic and
946 hadronic DM annihilation channels. From ~ 10 TeV to ~ 100 TeV, both the IACTs and HAWC
947 contribute significantly to the leptonic DM limit. For hadronic and bosonic DM, the IACTs and
948 *Fermi*-LAT both contribute strongly.

949 We notice that the limits computed using the \mathcal{B} set of J -factor are always better compared to the
950 ones calculated with the $\mathcal{G}\mathcal{S}$ set. For the W^+W^- , Z^+Z^- , $b\bar{b}$, and $t\bar{t}$ channels, the ratio between the
951 limits computed with the two sets of J -factor is varying between a factor of ~ 3 and ~ 5 depending
952 on the energy, with the largest ratio around 10 TeV. For the channels e^+e^- , $\mu^+\mu^-$, and $\tau^+\tau^-$, the
953 ratio lies between ~ 2 to ~ 6 , being maximum around 1 TeV. Examining Figure 6.16 and Figure 6.17
954 in Section 6.8, these differences are explained by the fact that the \mathcal{B} set provides higher J -factors
955 for the majority of the studied dSphs, with the notable exception of Segue I. The variation on the
956 ratio of the limits for the two sets is due to different dSph dominating the limits depending on the
957 energy. This pushes the range of thermal cross-section which can be excluded to higher mass. This
958 comparison demonstrates the magnitude of systematic uncertainties associated with the choice of

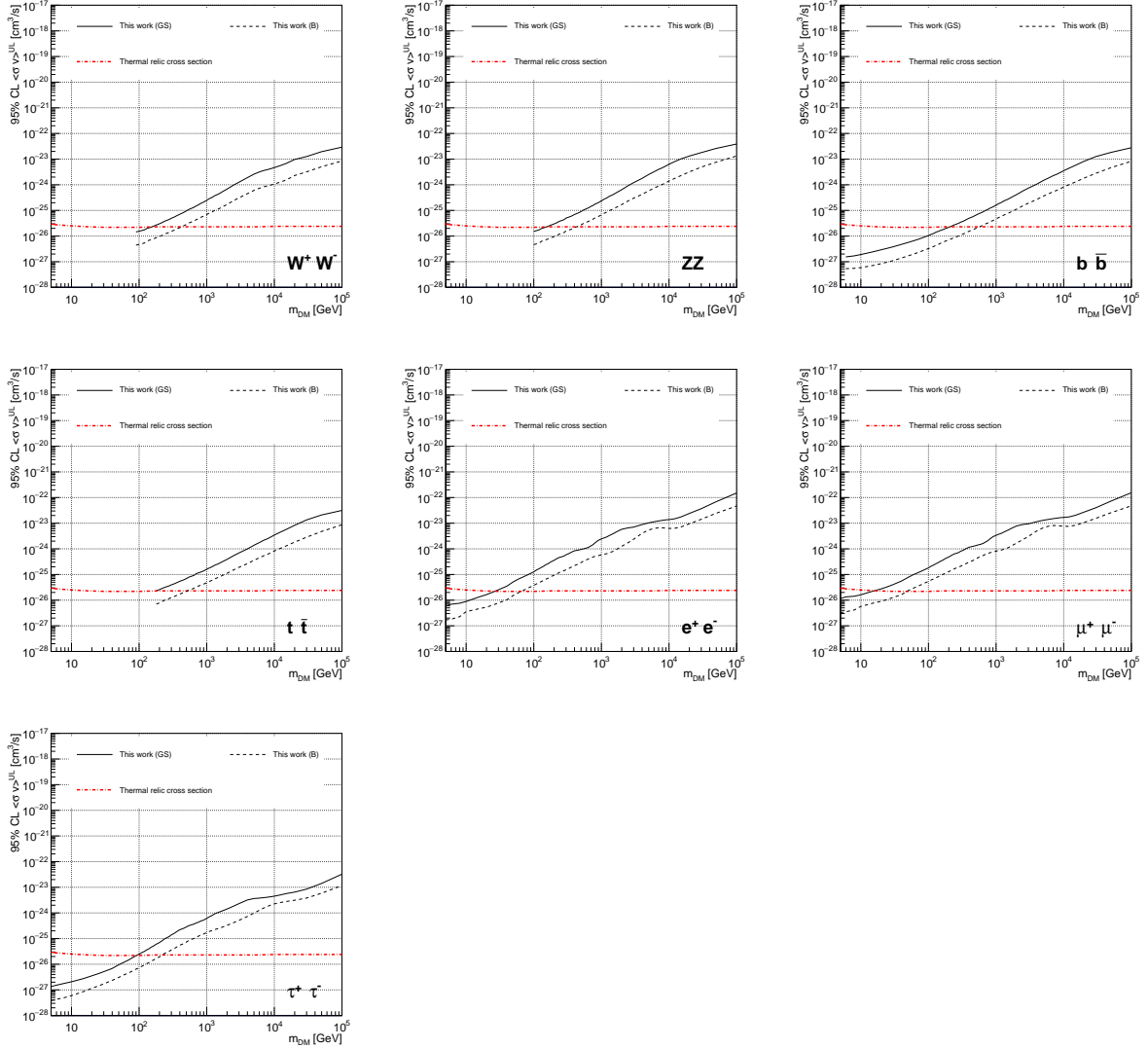


Figure 6.10 Comparisons of the combined limits at 95% confidence level for each of the eight annihilation channels when using the J factors from Ref. [53] (\mathcal{GS} set in Table 6.1), plain lines, and the J factor from Ref. [47, 55] (\mathcal{B} set in Table 6.1), dashed lines. The cross-section given by the thermal relic is also indicated [54].

959 the J -factor

960 This comparison demonstrates the magnitude of systematic uncertainties associated with the
 961 choice of the J -factor calculation. The \mathcal{GS} and \mathcal{B} sets present a difference in the limits for all
 962 channels of about This difference is explained, see Figure 6.16 and Figure 6.17 in Appendix, by the
 963 fact that the \mathcal{B} set provides higher J factors for all dSph except for Segue I. This pushes the range
 964 of thermal cross-section which can be excluded to higher mass.

965 **6.7 HAWC Systematics**

966 **6.7.1 Inverse Compton Scattering**

967 The DM-DM annihilation channels produce many high energy electrons regardless of the
968 primary annihilation channel. These high energy electrons can produce high energy gamma-rays
969 through Inverse Compton Scattering (ICS). If this effect is strong, it would change the morphology
970 of the source and increase the total expected gamma-ray counts from any source. The PPPC [44]
971 provides tools in Mathematica for calculating the impact of ICS for an arbitrary location in the
972 sky for a specified annihilation channel. We calculated the change in gamma-ray counts for DM
973 annihilation to primary $e\bar{e}$ for RA and Dec corresponding to Segue1 and Coma Berenices. These
974 dSphs were chosen because they are the strongest contributors to the limit. $e\bar{e}$ was selected because
975 it would have the largest number of high energy electrons. The effect was found to be on the order
976 of 10^{-7} on the gamma-ray spectrum. As a result, this systematic is not considered in our analysis.

977 **6.7.2 Point Source Versus Extended Source Limits**

978 The previous DM search toward dSph approximated the dSphs as point sources [46]. In
979 this analysis, the dSphs are implemented as extended with J-factor distributions following those
980 produced by [53]. The resolution of the cited map is much finer than HAWC's angular resolution.
981 The vast majority of the J-factor distribution is represented on the central HAWC pixel of the dSph
982 spatial map. However, the neighboring 8 pixels are not negligible and contribute to our limit.

983 Figure 6.11 shows a substantial improvement to the limit for Segue1. Fig. 6.12 however showed
984 identical limits. These disparities are best explained by the relative difference in their J-Factors.
985 Both dSphs pass almost overhead the HAWC detector, however Segue1 has the larger J-Factor
986 between the two. Adjacent pixels to the central pixel will therefore contribute to the limits. This is
987 the case for other dSph that are closer to overhead the HAWC detector.

988 Comparison plots for all sources and the combined limit can be found in the sandbox for the
989 Glory Duck project.

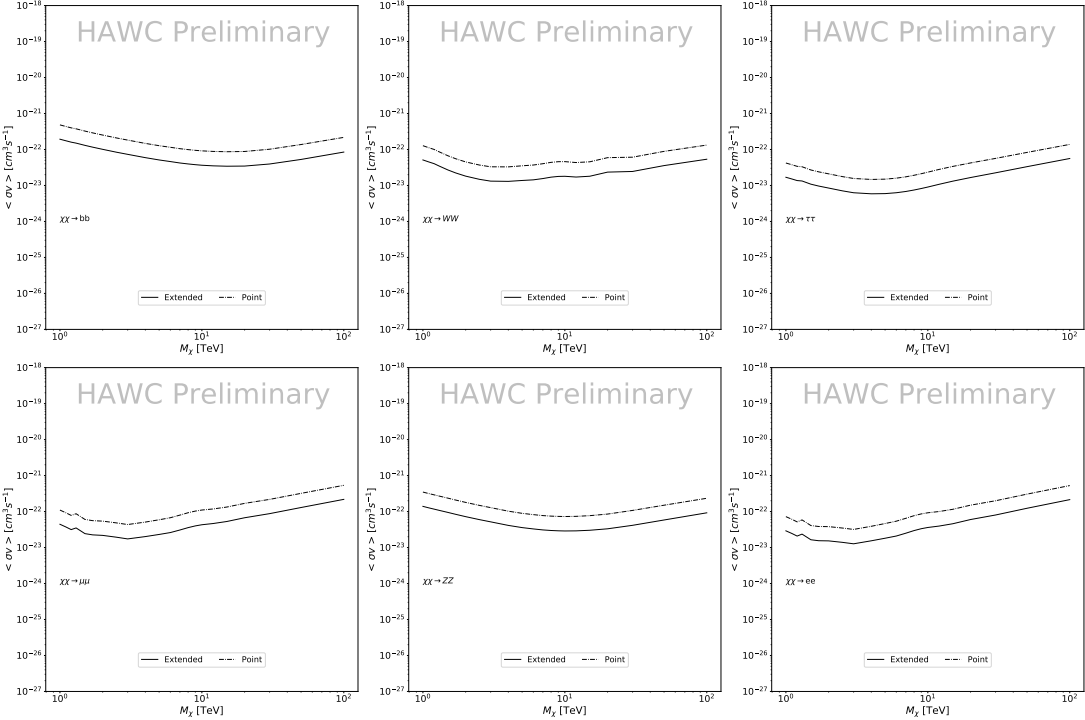


Figure 6.11 Comparisons of the combined limits at 95% confidence level for a point source analysis and extended source using [53] \mathcal{GS} J-factor distributions and PPPC [44] annihilation spectra. Shown are the limits for Segue1 which will have the most significant impact on the combined limit. 6 of the 7 DM annihilation channels are shown. Solid lines are extended source studies. Dashed lines are point source studies. Overall, the extended source analysis improves the limit by a factor of 2.

6.7.3 Impact of Pointing Systematic

During the analysis it was discovered that reconstruction of gamma-rays. Slides describing this systematic can be found [here](#). Shown on the presentation is dependence on the pointing systematic on declination. New spatial profiles were generated for every dSph and limits were computed for the adjusted declination.

Section 6.7.3 demonstrates the impact of this systematic for all DM annihilation channels studied by HAWC. The impact is a tiny improvement, yet mostly identical, to the combined limits.

6.8 J-factor distributions

6.8.1 Numerical integration of \mathcal{GS} maps

It was discovered well after the HAWC analysis was completed that the published tables from

\mathcal{GS} [45] quoted median J-factors were computed in a non-trivial manner. The assumption myself

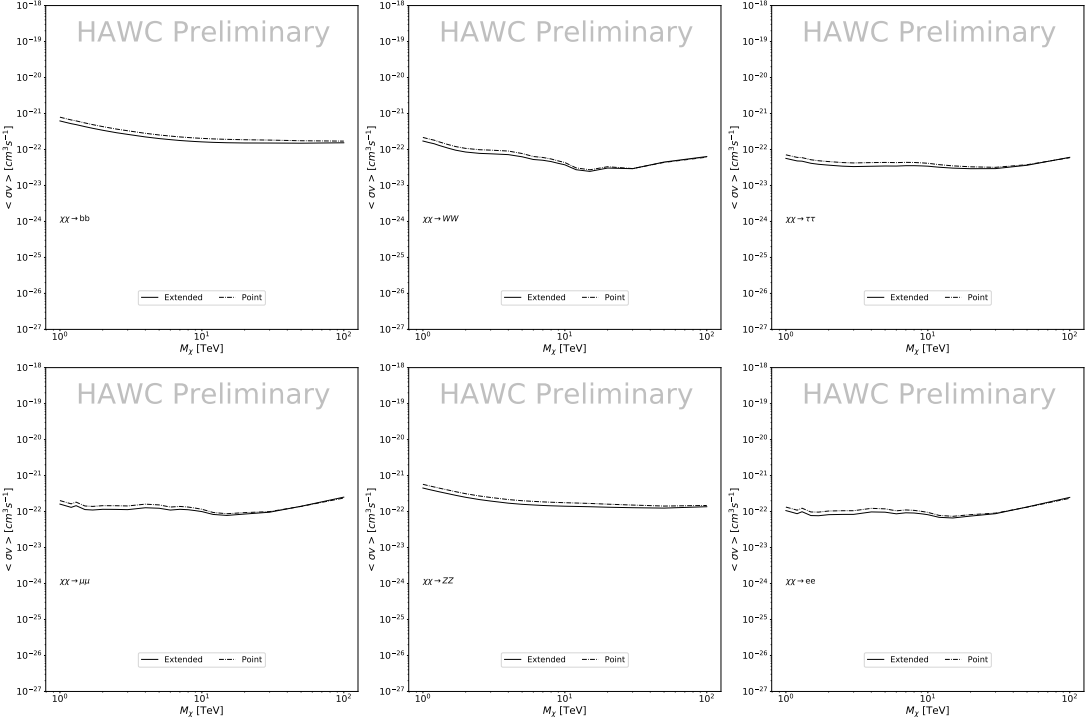


Figure 6.12 Same as Fig. 6.11 on Coma Berenices. This dSph also contributes significantly to the limit. The limits are identical in this case.

and collaborators had been that the published tables represented the J -factor as a function of θ for the best global fit model on a per-source basis. However, this is not the case. Instead, what is published are the best fit model for each dwarf that only considers stars up to the angular separation θ . Therefore, the model is changing for each value of θ for each dwarf. Yet, the introduced features from unique models at each θ are much smaller than the angular resolution of HAWC. It is not expected for these effects to impact the limits and TS greatly as a result.

Median J -factor model profiles were provided by the authors. New maps were generated and analyzed for Segue1 and Coma Berenices. Figure 6.14 shows the differential between maps generated with the method from Section 6.8.1 and from the authors of [45]. These maps were reanalyzed for all SM DM annihilation channels. Upper limits for these channels are shown in Figure 6.15

From Figure 6.15, we can see that the impact of these model difference was no substantial. The observed impact was a fractional effect which is much smaller than the impact from selecting another DM spatial distribution model as was shown in Figure 6.10.

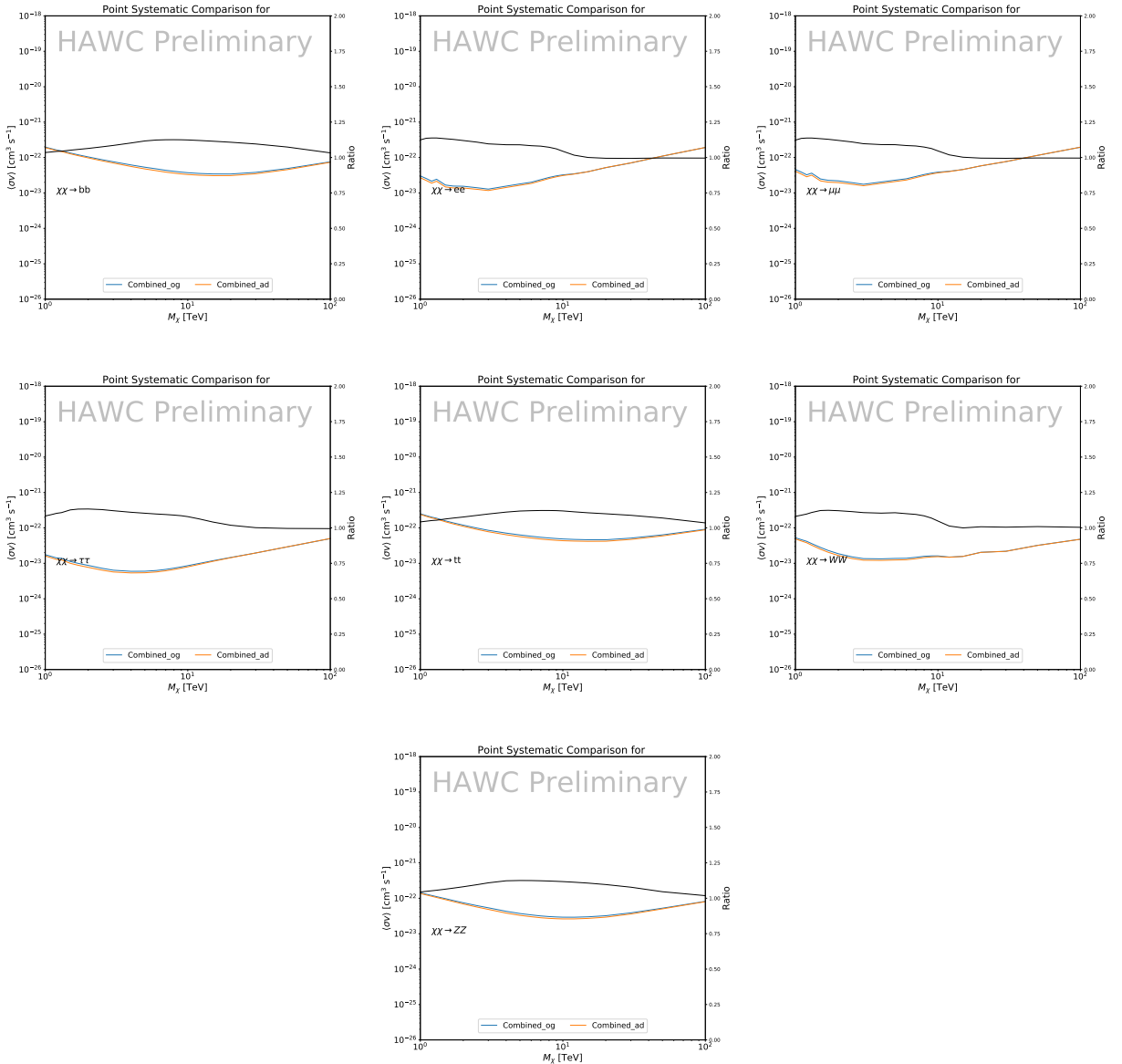


Figure 6.13 Comparison of combined limits when correcting for HAWC’s pointing systematic. All DM annihilation channels are shown. The solid black line is the ratio between published limit to the declination corrected limit. The blue solid line or “Combined_{og}” represented the limits computed for Glory Duck. The solid orange line or “Combined_{ad}” represented the limits computed after correcting for the pointing systematic.

1015 6.8.2 $\mathcal{G}\mathcal{S}$ Versus \mathcal{B} spatial models

1016 We show in this appendix a comparison between the J -factors computed by Geringer-Sameth
 1017 *et al.* [53] (the $\mathcal{G}\mathcal{S}$ set) and the ones computed by Bonnivard *et al.* [47, 55] (the \mathcal{B} set). The
 1018 $\mathcal{G}\mathcal{S}$ J -factors are computed through a Jeans analysis of the kinematic stellar data of the selected

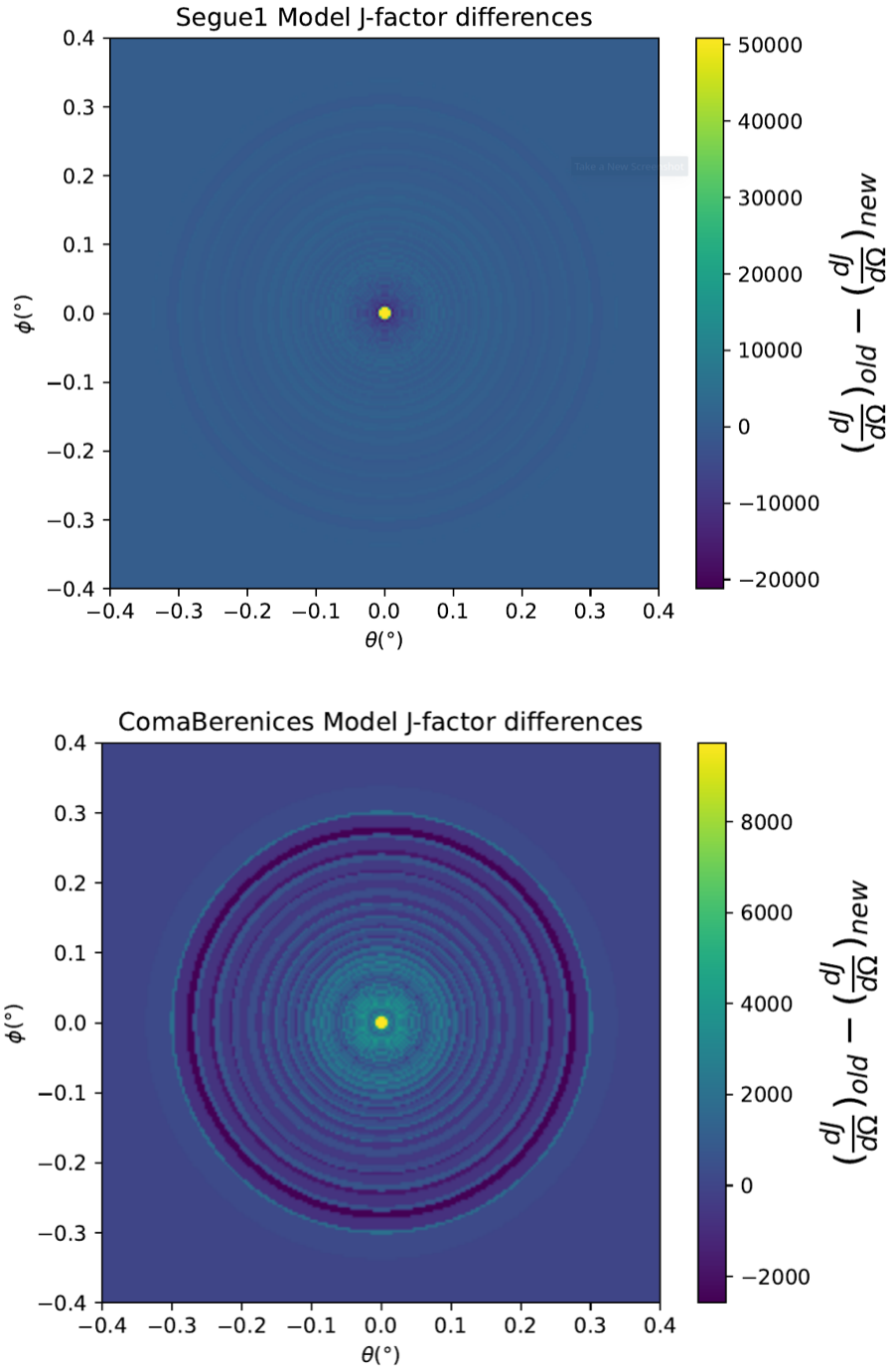


Figure 6.14 Differential map of dJ/Ω from model built in Section 6.8.1 and profiles provided directly from authors. (Top) Differential from Segue1. (bottom) Differential from Coma Berenices. Note that their scales are not the same. Segue1 shows the deepest discrepancies which is congruent with its large uncertainties. Both models show anuli where unique models become apparent.

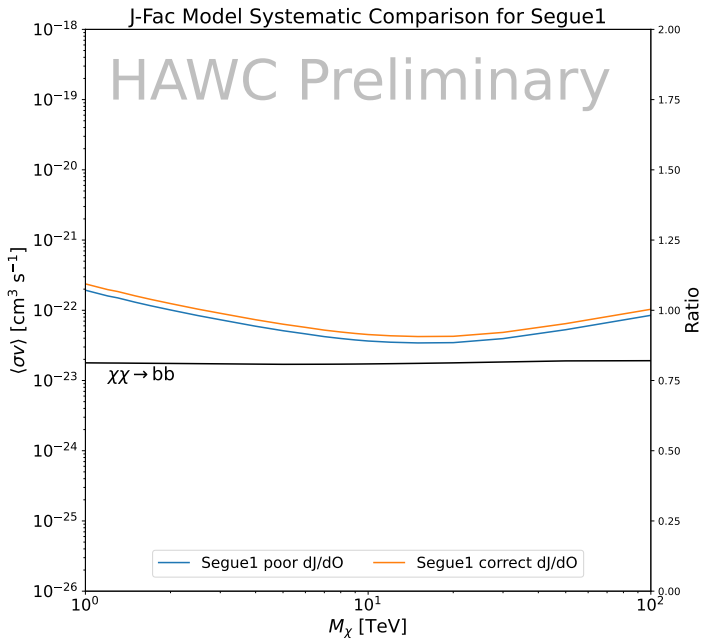
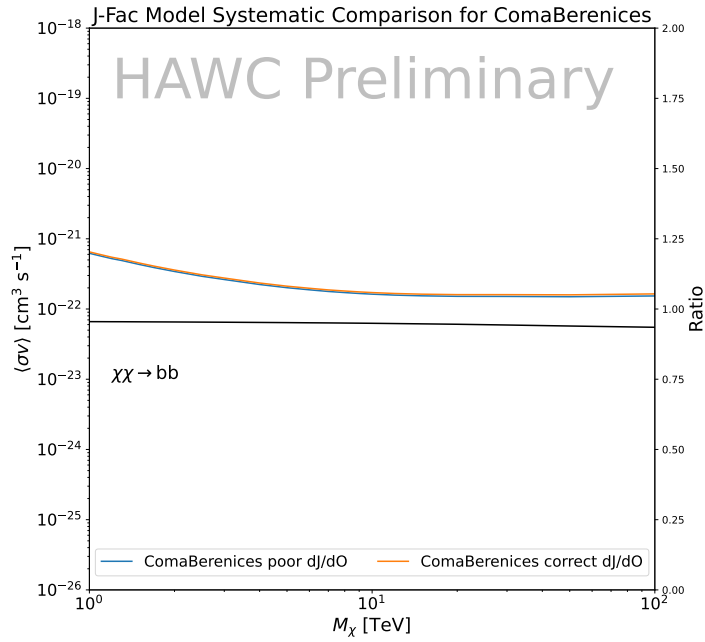


Figure 6.15 HAWC limits for Coma Berenices (top) and Segue1 (bottom) for two different map sets. Blue lines are limits calculated on maps with poor model representation. Orange lines are limits calculated on spatial profiles provided by the authors of [45]. Black line is the ratio of the poor spatial model limits to the corrected spatial models. The left y-axis measures $\langle \sigma v \rangle$ for the blue and orange lines. The right y-axis measures the ratio and is unitless.

1019 dSphs, assuming a dynamic equilibrium and a spherical symmetry for the dSphs. They adopted
1020 the generalized DM density distribution, known as Zhao-Hernquist, introduced by [58], carrying
1021 three additional index parameters to describe the inner and outer slopes, and the break of the
1022 density profile. Such a profile parametrization allows the reduction of the theoretical bias from
1023 the choice of a specific radial dependency on the kinematic data. In other words, the increase of
1024 free parameters with the use of the Zhao-Hernquist profile allows a better description of the mass
1025 density distribution of dark matter.

1026 In addition, a constant velocity anisotropy profile and a Plummer light profile [59] for the stellar
1027 distribution were assumed. The velocity anisotropy profile depends on the radial and tangential
1028 velocity dispersion. However, its determination remains challenging since only the line-of-sight
1029 velocity dispersion can be derived from velocity measurements. Therefore, the parametrization of
1030 the anisotropy profile is obtained from simulated halos (see [60] for more details). They provide the
1031 values of the J -factors of regions extending to various angular radius up to the outermost member
1032 star.

1033 The \mathcal{B} J -factors were computed through a Jeans analysis taking into account the systematic
1034 uncertainties induced by the DM profile parametrization, the radial velocity anisotropy profile, and
1035 the triaxiality of the halo of the dwarf galaxies. They performed a more complete study of the dSph
1036 kinematics and dynamics than \mathcal{GS} for the determination of the J -factor. Conservative values of the
1037 J -factors where obtained using an Einasto DM density profile [61], a realistic anisotropy profile
1038 known as the Baes & Van Hese profile [62] which takes into account that the inner regions can be
1039 significantly non-isotropic, and a Zhao-Hernquist light profile [58].

1040 For both sets, J -factor values are provided for all dSphs as a function of the radius of the
1041 integration region [53, 47, 55]. Table 6.1 shows the heliocentric distance and Galactic coordinates
1042 of the twenty dSphs, together with the two sets of J -factor values integrated up to the outermost
1043 observed star for \mathcal{GS} and the tidal radius for \mathcal{B} . Both J -factor sets were derived through a Jeans
1044 analysis based on the same kinematic data, except for Draco where the measurements of [63] have
1045 been adopted in the computation of the \mathcal{B} value. The computations for producing the \mathcal{GS} and \mathcal{B}

1046 samples differ in the choice of the DM density, velocity anisotropy, and light profiles, for which the
1047 set \mathcal{B} takes into account some sources of systematic uncertainties.

1048 Figure 6.16 and Figure 6.17 show the comparisons for the J -factor versus the angular radius
1049 for each of the 20 dSphs used in this study. The uncertainties provided by the authors are also
1050 indicated in the figures. For the \mathcal{GS} set, the computation stops at the angular radius corresponding
1051 to the outermost observed star, while for the \mathcal{B} set, the computation stops at the angular radius
1052 corresponding to the tidal radius.

1053 6.9 Discussion and Conclusions

1054 In this multi-instrument analysis, we have used observations of 20 dSphs from the gamma-ray
1055 telescopes Fermi-LAT, H.E.S.S., MAGIC, VERITAS, and HAWC to perform a collective DM
1056 search annihilation signals. The data were combined across sources and detectors to significantly
1057 increase the sensitivity of the search. We have observed no significant deviation from the null, no
1058 DM hypothesis, and so present our results in terms of upper limits on the annihilation cross-section
1059 for seven potential DM annihilation channels.

1060 Fermi-LAT brings the most stringent constraints for continuum channels below approximately
1061 1 TeV. The remaining detectors dominate at higher energies. Overall, for multi-TeV DM mass,
1062 the combined DM constraints from all five telescopes are 2-3 times stronger than any individual
1063 telescope for multi-TeV DM.

1064 Derived from observations of many dSphs, our results produce robust limits given the DM
1065 content of the dSphs is relatively well constrained. The obtained limits span the largest mass
1066 range of any WIMP DM search. Our combined analysis improves the sensitivity over previously
1067 published results from each detector which produces the most stringent limits on DM annihilation
1068 from dSphs. These results are based on deep exposures of the most promising known dSphs with
1069 the currently most sensitive gamma-ray instruments. Therefore, our results constitute a legacy of
1070 a generation of gamma-ray instruments on WIMP DM searches towards dSphs. Our results will
1071 remain the reference in the field until a new generation of more sensitive gamma-ray instruments
1072 begin operations, or until new dSphs with higher J -factors are discovered.

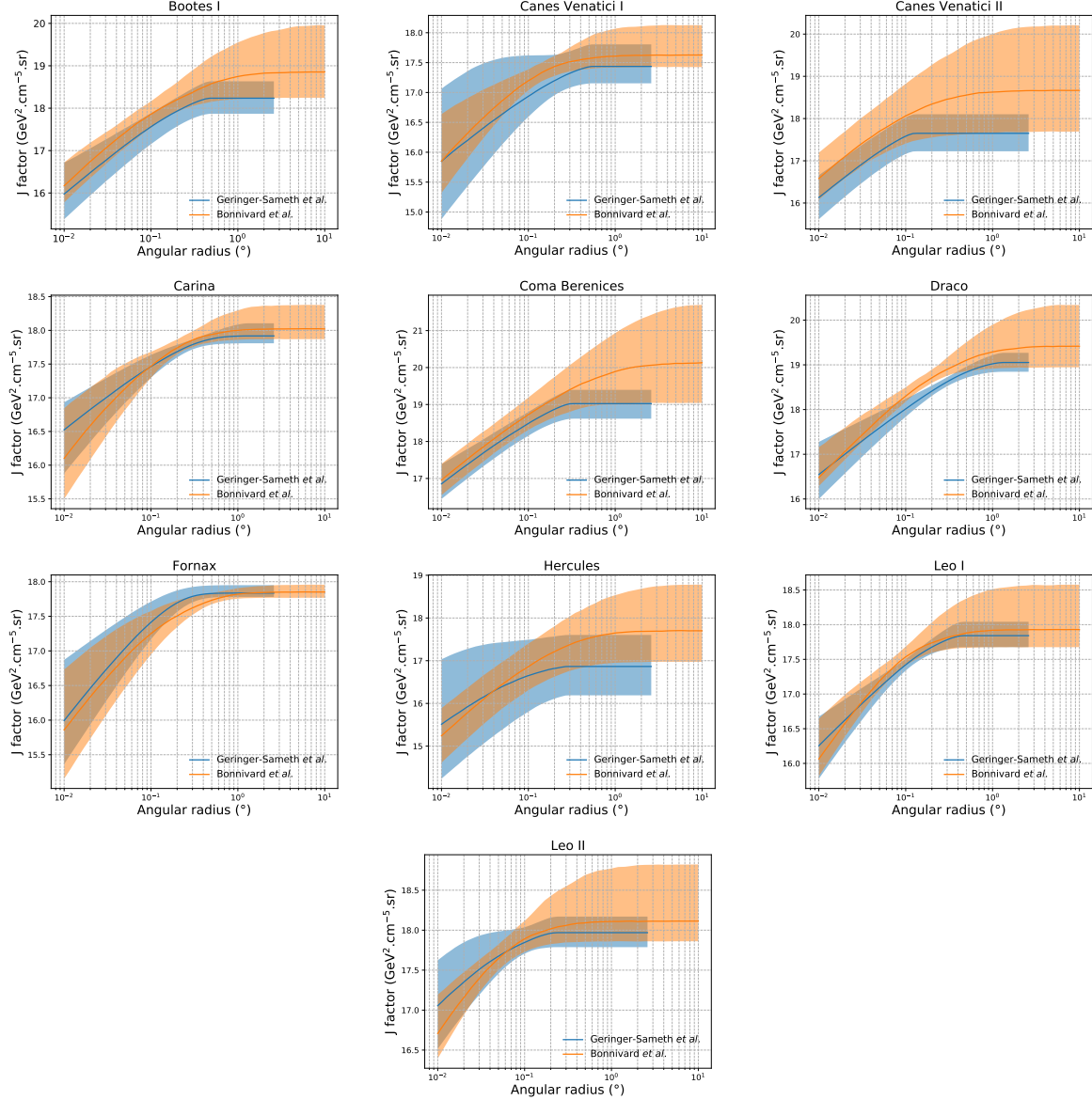


Figure 6.16 Comparisons between the J -factors versus the angular radius for the computation of J factors from Ref. [53] (\mathcal{GS} set in Table 6.1) in blue and for the computation from Ref. [47, 55] (\mathcal{B} set in Tab. 6.1) in orange. The solid lines represent the central value of the J -factors while the shaded regions correspond to the 1σ standard deviation.

This analysis serves as a proof of concept for future multi-instrument and multi-messenger combination analyses. With this collaborative effort, we have managed to sample over four orders in magnitude in gamma-ray energies with distinct observational techniques. Determining the nature of DM continues to be an elusive and difficult problem. Larger datasets with diverse measurement techniques could be essential to tackling the DM problem. A future collaboration using similar

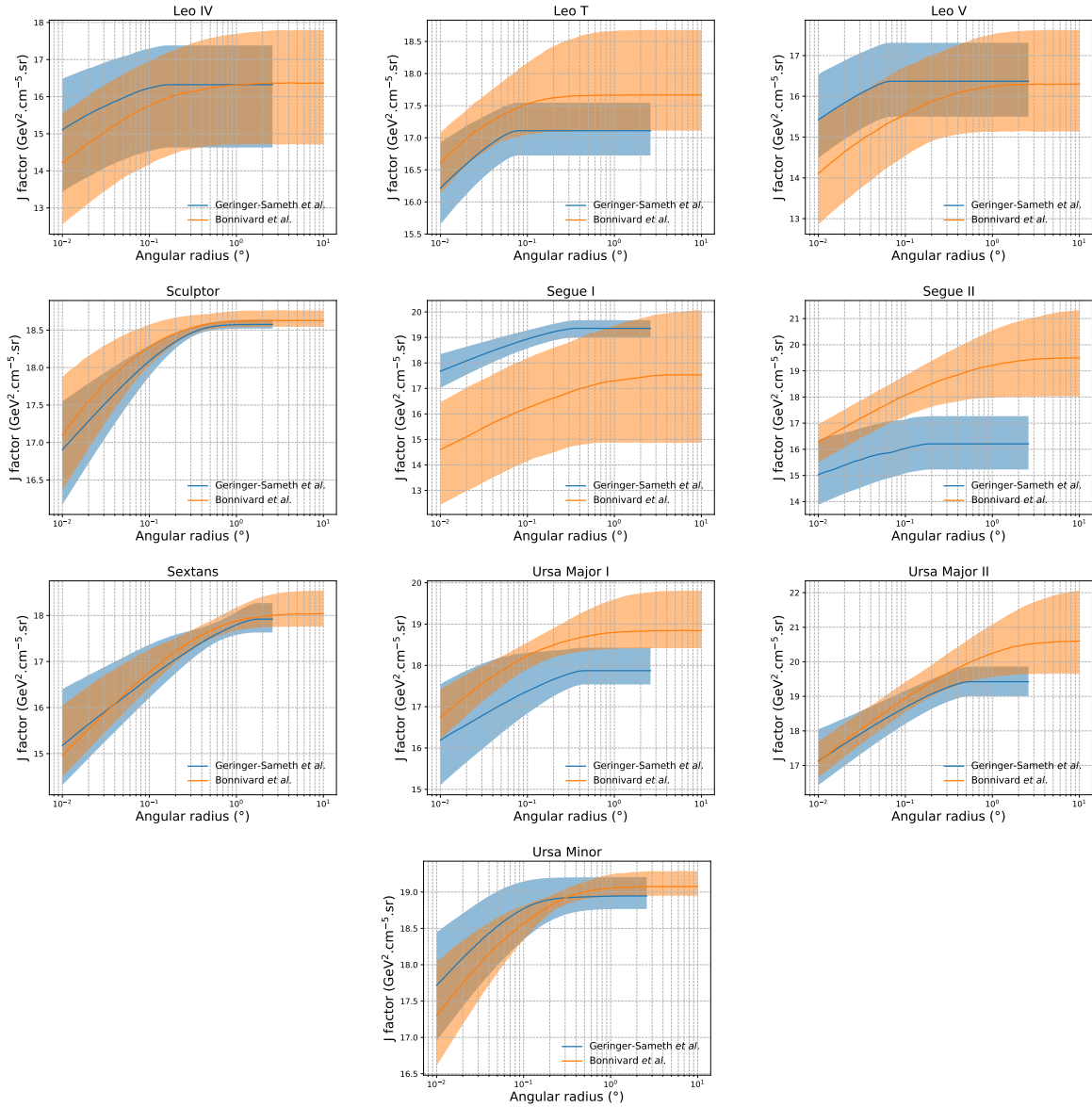


Figure 6.17 Comparisons between the J -factors versus the angular radius for the computation of J factors from Ref. [53] (\mathcal{GS} set in Tab. 6.1) in blue and for the computation from Ref. [47, 55] (\mathcal{B} set in Tab. 6.1) in orange. The solid lines represent the central value of the J -factors while the shaded regions correspond to the 1σ standard deviation.

1078 techniques as the ones described in this paper could grow even beyond gamma rays. The models we
 1079 used for this study include annihilation channels with neutrinos in the final state. Advanced studies
 1080 could aim to merge our results with those from neutrino observatories with large data sets. Efforts
 1081 are already underway to add data from the IceCube, ANTARES, and KM3NeT observatories to
 1082 these gamma-ray results.

1083 From this work, a selection of the best candidates for observations, according to the latest
1084 knowledge on stellar dynamics and modelling techniques for the derivation of the J -factors on
1085 the potential dSphs targets, is highly desirable at the time that new experiments are starting their
1086 dark matter programs using dSphs. Given the systematic uncertainty inherent to the derivation of
1087 the J -factors, an informed observational strategy would be to select both objects with the highest
1088 J -factors that could lead to DM signal detection, and objects with robust J -factor predictions, i.e.
1089 with kinematic measurements on many bright stars, which would strengthen the DM interpretation
1090 reliability of the observation outcome.

1091 This analysis combines data from multiple telescopes to produce strong constraints on astro-
1092 physical objects. From this perspective, these methods can be applied beyond just DM searches.
1093 Almost every astrophysical study can benefit from multi-telescope, multi-wavelength gamma-ray
1094 studies. We have enabled these telescopes to study the cosmos with greater precision and detail.
1095 Many astrophysical searches can benefit from multi-instrument gamma-ray studies, for which our
1096 analysis lays the foundation.

CHAPTER 7

MULTITHREADING HAWC ANALYSES FOR DARK MATTER SEARCHES

7.1 Introduction

HAWC's current software suite, plugins to 3ML, does not fully utilize computational advancements of recent decades. Said advancements include the proliferation of Graphical Processing Units (GPUs), and multithreading on multi-core processors. The analysis described in chapter 6 took up to 3 months of human time waiting for the full gambit of data analysis and simulation of background to run. Additionally, with the addition of a 2D binning scheme, f_{hit} and NN, the compute time is expected to grow. Although excessive computing time was, in part, from an intense use of a shared computing cluster, it was evident that there was room for improvement. In HAWC's next generation dSph DM search, I decided to develop codes that would utilize the multi-core processors on modern high performance computing clusters. The results of this work are featured in this chapter and brought a human timing improvement to computation that scales as $1/N$ where N is the number of threads.

7.2 Dataset and Background

This section enumerates the data and background methods used for HAWC's multi-threaded study of dSphs. Section 7.2.1 and Section 7.2.2 are most useful for fellow HAWC collaborators looking to replicate a multithreaded dSph DM search.

7.2.1 Itemized HAWC files

- Detector Resolution: `refit-Pass5-Final-NN-detRes-zenith-dependent.root`
- Data Map: `Pass5-Final-NN-maptree-ch103-ch1349-zenith-dependent.root`
- Spectral Dictionary: `HDMspectra_dict_gamma.npy`

7.2.2 Software Tools and Development

This analysis was performed using HAL and 3ML [42, 43] in Python version 3. I built software in collaboration with Michael Martin and Letrell Harris to implement the *Dark Matter Spectra from*

1121 *the Electroweak to the Planck Scale* (HDM) [64] and dSphs spatial model from [65] for HAWC
1122 analysis. A NumPy dictionary of HDM was made for Py3. The corresponding Python3 file is
1123 `HDMspectra_dict_gamma.npy`. These files can also be used for decay channels and tools are
1124 provided in HDM’s [git repository](#) [64]. The analysis was performed using the Neural Network
1125 energy estimator for Pass 5.F. A description of this estimator was provided in chapter 4. **TODO:**
1126 **define a subsection when it’s written** All other software used for data analysis, DM profile generation,
1127 and job submission to SLURM are also kept in my sandbox in the [Dark Matter HAWC](#) project.
1128 The above repository also incorporates the model inputs used previously in Glory Duck, described
1129 in chapter 6

1130 7.2.3 Data Set and Background Description

1131 The HAWC data maps used for this analysis contain 2565 days of data between runs 2104 (

1132 **TODO: Day start**) and 7476 (**TODO: day end**). They were generated from pass 4.0 reconstruction.

1133 The analysis is performed using the NN energy estimator with bin list:

1134 B1C0Ea, B1C0Eb, B1C0Ec, B1C0Ed, B1C0Ee, B2C0Ea, B2C0Eb, B2C0Ec, B2C0Ed, B2C0Ee,
1135 B3C0Ea, B3C0Eb, B3C0Ec, B3C0Ed, B3C0Ee, B3C0Ef, B4C0Eb, B4C0Ec, B4C0Ed, B4C0Ee,
1136 B4C0Ef, B5C0Ec, B5C0Ed, B5C0Ee, B5C0Ef, B5C0Eg, B6C0Ed, B6C0Ee, B6C0Ef, B6C0Eg,
1137 B6C0Eh, B7C0Ee, B7C0Ef, B7C0Eg, B7C0Eh, B7C0Ei, B8C0Ee, B8C0Ef, B8C0Eg, B8C0Eh,
1138 B8C0Ei, B8C0Ej, B9C0Ef, B9C0Eg, B9C0Eh, B9C0Ei, B9C0Ej, B10C0Eg, B10C0Eh,
1139 B10C0Ei, B10C0Ej, B10C0Ek, B10C0El

1140 Bin 0 was excluded as it has substantial hadronic contamination and poor angular resolution.

1141 Background considerations and source selection was identical to Section 6.2, and no additional
1142 arguments are provided here. Many of the HAWC systematics explored in Section 6.7 also apply
1143 for this DM search and are not added upon here.

1144 7.3 Analysis

1145 The analysis and its systematics are almost identical to Section 6.3. Importantly, we use the
1146 same Equation (6.1) and Equation (6.2) for estimating the gamma-ray flux at HAWC from our

1147 sources. We add on to the previous study with a search for DM decay. The flux equations for DM
 1148 decay are

$$\frac{d\Phi_\gamma}{dE_\gamma} = \frac{1}{4\pi\tau m_\chi} \frac{dN_\gamma}{dE_\gamma} \times \int_{\text{source}} d\Omega \int_{l.o.s} \rho_\chi dl(r, \theta') \quad (7.1)$$

1149 with a new quantity, the D factor, defined as

$$D = \int d\Omega \int_{l.o.s} dl \rho_\chi(r, \theta') \quad (7.2)$$

1150 Software was written to accomodate DM decay from dSphs, however decay profiles were not
 1151 received from $\mathcal{L}\mathcal{S}$ by the time of writing this tehsis.

1152 **7.3.1 $\frac{dN_\gamma}{dE_\gamma}$ - Particle Physics Component**

1153 For these spectra, we import HDM with Electroweak (EW) corrections and additional correc-
 1154 tions for neutrinos above the EW scale [64]. The spectrum is implemented as a model script in
 1155 astromodels for 3ML. A comprehensive description of EW corrections and neutrino considerations
 1156 are provided later in [TODO: refeance MM nu duck](#).

1157 Figure 7.1 demonstrates the impact of changes from HDM on DM annihilation to W bosons.
 1158 A class in astromodels was developed to include HDM and is aptly named `HDMspectra` within
 1159 `DM_models.py`. The SM DM annihilation channels studied here are $\chi\chi \rightarrow$:

1160 e^+e^- , $\mu^+\mu^-$, $\tau^+\tau^-$, $b\bar{b}$, $t\bar{t}$, gg , W^+W^- , ZZ , $c\bar{c}$, $u\bar{u}$, $d\bar{d}$, $s\bar{s}$, $\nu_e\bar{\nu}_e$, $\nu_\mu\bar{\nu}_\mu$, $\nu_\tau\bar{\nu}_\tau$, $\gamma\gamma$, hh .

1161 For $\gamma\gamma$ and ZZ , a substantial fraction of the signal photons are expected to have total energy equal
 1162 m_χ [64]. This introduces a δ -function that is much narrower than the energy resolution of the
 1163 HAWC detector. To ensure that this feature is not lost in the likelihood fits, the 'line' feature is
 1164 convolved with a gausian kernel with a 1σ width of $0.05 \cdot m_\chi$ and total kernel window of $\pm 4\sigma$.
 1165 This difers from HAWC's previous line study where 30% of HAWC's energy resolution was used
 1166 for the kernel [66]. The NN energy estimator's strength compared to f_{hit} at low gamma-ray energy
 1167 enables smaller resolutions in addition to low energy tails in the spectral models [64]. $\chi\chi \rightarrow \gamma\gamma$
 1168 and ZZ spectral hypotheses are shown in Figure 7.2. Spectral models for the remaining annihilation
 1169 channels are plotted for each m_χ in Figure B.1.

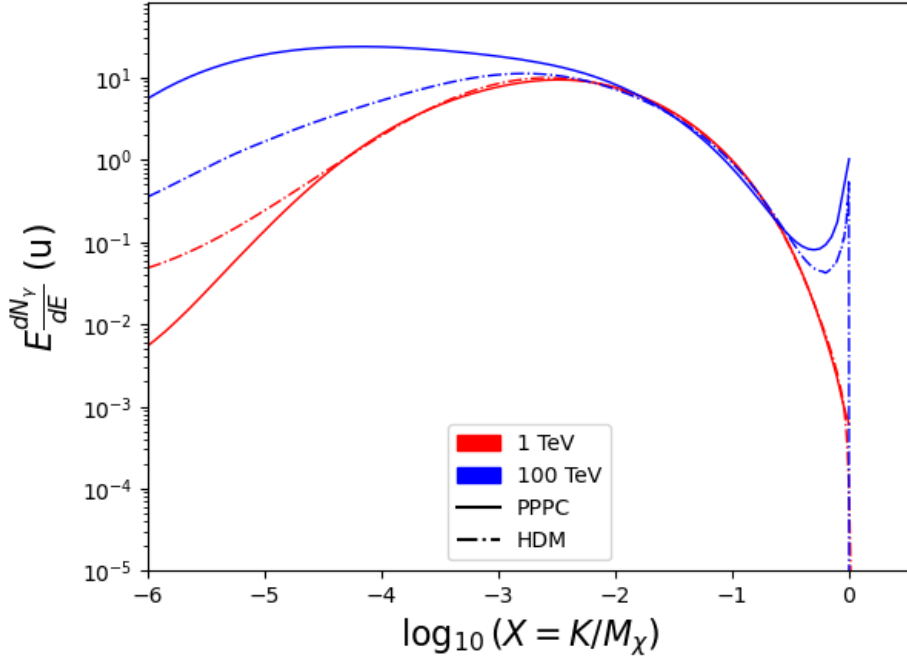


Figure 7.1 Difference between spectral hypotheses from PPPC [44] and HDM [64]. Shown is the expected DM annihilation spectrum for $\chi\chi \rightarrow W^-W^+$. Solid lines are spectral models with EW corrections from the PPPC. Dash-dot lines are spectral models from HDM. Red lines are models for $M_\chi = 1$ TeV. Blue lines represent models for $M_\chi = 100$ TeV.

1170 7.3.2 *J* and *D*- Astrophysical Components

1171 The J-factor profiles for each source are imported from Louis Strigari et al. (referred to with
 1172 \mathcal{LS}) [65]. Profiles in $\frac{dJ}{d\Omega}(\theta)$ up to $\theta = 0.5^\circ$ were provided directly from the authors. Map generation
 1173 from these profiles were almost identical to Section 6.3.2 except that a higher order trapezoidal
 1174 integral was used for the normalization of the square, uniformly-spaced map:

$$p^2 \cdot \sum_{i=0}^N \sum_{j=0}^M w_{i,j} \frac{d\mathcal{K}}{d\Omega}(\theta_{i,j}, \phi_{i,j}) \quad (7.3)$$

1175 \mathcal{K} is either J or D for the spatial distributions of annihilation or decay respectively. p is the angular
 1176 side of one pixel in the map. $w_{i,j}$ is a weight assigned the following ways:

1177 $w_{i,j} = 1$ if $(\theta_{i,j}, \phi_{i,j})$ is fully within the region of integration

1178 $w_{i,j} = 1/2$ if $(\theta_{i,j}, \phi_{i,j})$ is on an edge of the region of integration

1179 $w_{i,j} = 1/4$ if $(\theta_{i,j}, \phi_{i,j})$ is on a corner of the region of integration

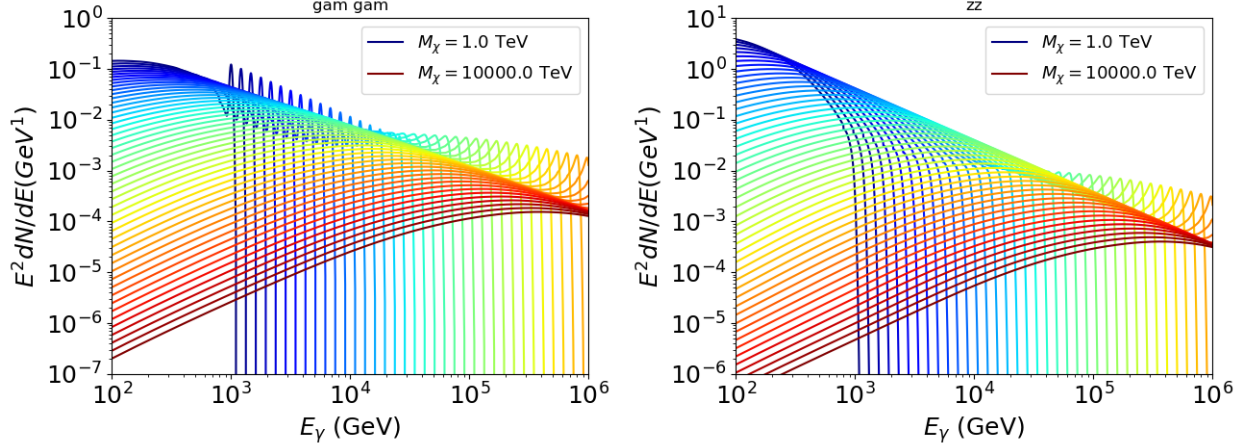


Figure 7.2 Photon spectra for $\chi\chi \rightarrow \gamma\gamma$ (left) and $\chi\chi \rightarrow ZZ$ (right) after gaussian convolution of line features. Both spectra have δ -features at photon energies equal to the DM mass. Bluer lines are annihilation spectra with lower DM mass. Redder lines are spectra from larger DM mass. All Spectral models are sourced from the Heavy Dark Matter models [64]. Axes are drawn roughly according to the energy sensitivity of HAWC.

1180 Figure 7.3 shows the median and $\pm 1\sigma$ maps used as input for DM annihilation studied by \mathcal{LS} .

1181 7.3.3 Source Selection and Annihilation Channels

1182 HAWC's sources for this multithreaded analysis include Coma Berenices, Draco, Segue 1, and
 1183 Sextans. \mathcal{LS} observes up to 43 sources in its publication, however only 4 of the best fit profiles were
 1184 provided at the time this thesis was written. A full description of each source used in this analysis
 1185 is found in Table 7.1.

1186 This analysis improves on chapter 6 in the following ways. Previously, the particle physics

Name	Distance (kpc)	l, b ($^\circ$)	$\log_{10} J$ (\mathcal{LS} set) $\log_{10}(\text{GeV}^2 \text{cm}^{-5} \text{sr})$
Coma Berenices	44	241.89, 83.61	$19.00^{+0.36}_{-0.35}$
Draco	76	86.37, 34.72	$18.83^{+0.12}_{-0.12}$
Segue I	23	220.48, 50.43	$19.12^{+0.49}_{-0.58}$
Sextans	86	243.50, 42.27	$17.73^{+0.13}_{-0.12}$

Table 7.1 Summary of the relevant properties of the dSphs used in the present work. Column 1 lists the dSphs. Columns 2 and 3 present their heliocentric distance and galactic coordinates, respectively. Column 4 reports the J -factors of each source given from the \mathcal{LS} studies and estimated $\pm 1\sigma$ uncertainties. The values $\log_{10} J$ (\mathcal{LS} set) [65] correspond to the mean J -factor values for a source extension truncated at 0.5° .

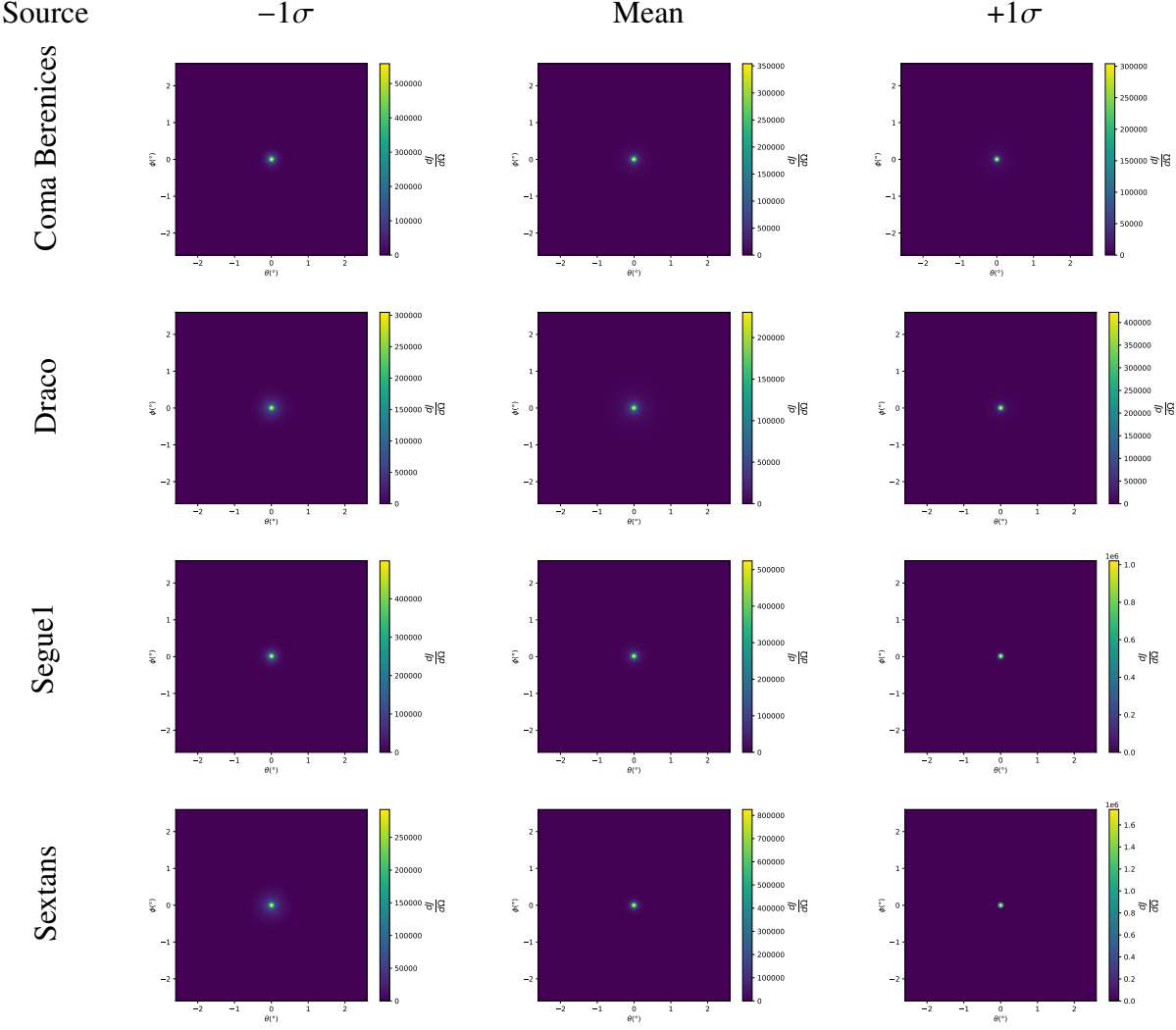


Figure 7.3 $\frac{dJ}{d\Omega}$ maps for Coma Berenices, Draco, Segue1, and Sextans. Columns are divided for the $\pm 1\sigma$ uncertainties in $dJ/d\Omega$ around the mean value from \mathcal{LS} [65]. Origin is centered on the specific dwarf spheroidal galaxies (dSph). θ and ϕ axes are the angular separation from the center of the dwarf

model used for gamma-ray spectra from DM annihilation was from the PPPC [44] which missed important considerations relevant for the neutrino sector. HDM is used to account for this shortfall [64]. HDM also models DM to the Planck scale which permits HAWC to probe PeV scale DM. For this study, we sample DM masses: 1 TeV - 10 PeV with 6 mass bins per decade in DM mass. In the case of line spectra ($\chi\chi \rightarrow \gamma\gamma$, or ZZ), we double the mass binning to 12 DM mass bins per decade in DM mass. A larger source catalog is used that uses a Navarro–Frenk–White (NFW) spatial DM distribution from \mathcal{LS} [65]. Because NFW has fewer parameters than what is used

1194 for \mathcal{GS} , \mathcal{LS} is able to fit ultra-faint dwarves, expanding the number of sources available for DM
1195 searches. Finally, the gamma-ray ray dataset is much larger. The study performed here analyzes
1196 2565 days of data compared to 1017 days analyzed in chapter 6.

1197 **7.4 Likelihood Methods**

1198 These are identical to Section 6.4.1 and no additional changes are made to the likelihood. Bins
1199 in this analysis are expanded to include HAWC’s NN energy estimator.

1200 **7.5 Computational Methods: Multithreading**

1201 Previously, as in Section 6.3, the likelihood was minimized for one model at a time. One
1202 model in this case representing a DM annihilation channel, DM mass, and dSph. In an effort
1203 to conserve human and CPU time, jobs submitted for high performance computing contained a
1204 list of DM masses to iterate over for likelihood fitting. Jobs were then trivially parallelized for
1205 each permutation of the two lists: CHANS (SM annihilation channel) and SOURCES (dSph spatial
1206 templates). The lists for CHANS and SOURCES are found in Section 7.3.1 and Table 7.1, respectively.
1207 Initially, 11 DM mass bins were serially sampled for one job defined by a [SM channel, dSph] set.
1208 Computing the likelihoods would take between 1.5 to 2 hrs, stocastically, for a job. We expect to
1209 compute likelihoods for data and 300 Poisson background trials. The estimated CPU time based on
1210 the above for all SM annihilation channels (17) and 25 sources (all \mathcal{LS} sources withing HAWC’s
1211 field of view) amounted to 127,925 jobs. In total, 1,407,175 likelihood fits and profiles would be
1212 computed for the 11 mass bins we wished to study. The estimated CPU time ranged between 10k
1213 CPU days - 8k CPU days. Human time is more challenging to estimate as job allocation is stochastic
1214 and highly dependant on what other users are submitting, yet it is unlikely that all jobs would run
1215 simultaneously. Therefore we can expect human time to be about as long as was seen in chapter 6
1216 which was on the order of months to fully compute on a smaller analysis. A visual aid to describe
1217 how jobs were organized is provided in Figure 7.4.

1218 The computational needs for this next generation DM analysis are extreme and is unlike other
1219 analyses performed on HAWC. It became clear that there was a lot to gain from optimzing how
1220 the likelihoods are computed. This section discusses how multi-threading was applied to solve and

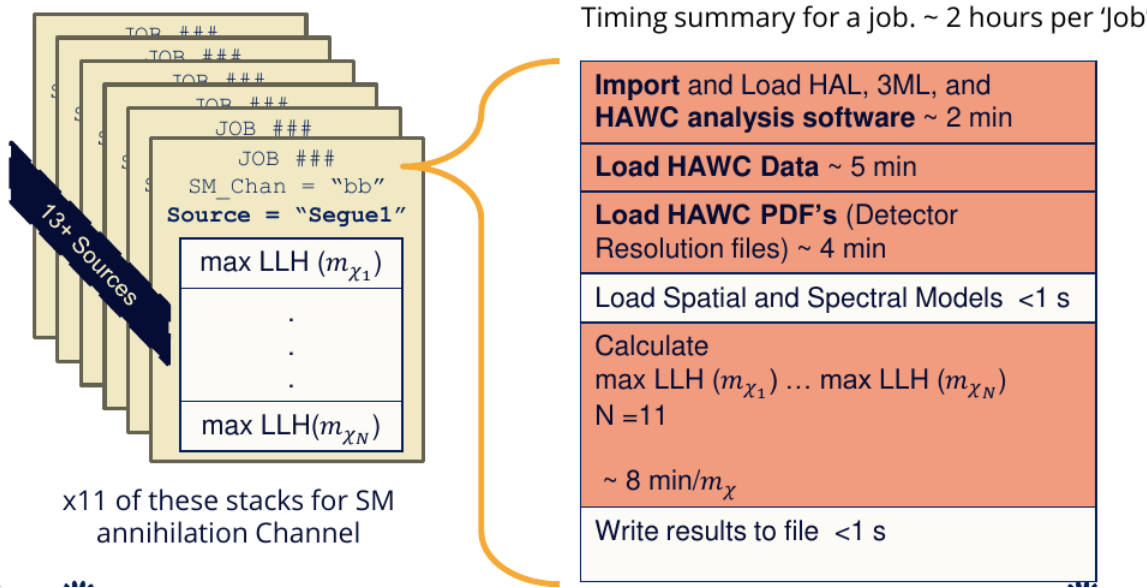


Figure 7.4 Infographic on how jobs and DM computation was organized in Section 6.3. Jobs were built for each permutation of CHANS and SOURCES shown by the left block in the figure. Each job, which took on the order 2 hrs to compute, had the following work flow: 1. Import HAWC analysis software, 2 min to run. 2. Load HAWC count maps, 5 min to run. 3. Load HAWC energy and spatial resolutions, 4 min. 5. Load DM spatial source templates and spectral models, less than 1 s. 6. Perform likelihood fit on data and model, about 8 min per DM mass. 7. Write results to file, less than 1s.

1221 reduce HAWC's computing of likelihoods for large parameter spaces like in DM searches.

1222 7.5.1 Relevant Foundational Information

1223 The profiling of the likelihood for HAWC is done via gradient descent where the normalization
 1224 of Equation (6.1) (linearly correlated with $\langle \sigma v \rangle$) is rescaled in the descent. Additionally, we sample
 1225 the likelihood space for a defined list of $\langle \sigma v \rangle$'s described in Section 6.4.2. The time to compute
 1226 these values is not predictable or consistent because many variables can change across the full
 1227 model-space. comprehensively, these variables are:

- 1228 • m_{χ} : DM rest mass
- 1229 • CHAN : DM SM annihilation channel.
- 1230 • SOURCE : dSph within HAWC's field of view. This involves a spatial template AND coordinate
 1231 in HAWC data.

1232 • $\langle \sigma v \rangle$: Effectevely the flux normalization and free parameter in the likelihood fit.
 1233 Therefore, we develop an asynchronous, functional-parallel coding pattern. Asyncronous meaning
 1234 that the instructions and computing within a function are independent and permitted to be out of sync
 1235 with sibling computations. Functional-parallel meaning that instructions are the subject of parral-
 1236 lelization rather than threading the likelihood computation. This is close to trivial parametrization
 1237 seen in Figure 7.4 except that we seek to consolidate the loading stages (software, data, and detector
 1238 resolution loading). Reducing the total instances of loading stages and distributing access to the
 1239 reduced loads across multiple asynchronous threads is expected to reduce serial processing time and
 1240 the overhead implicit to each job in addition to saving human time.

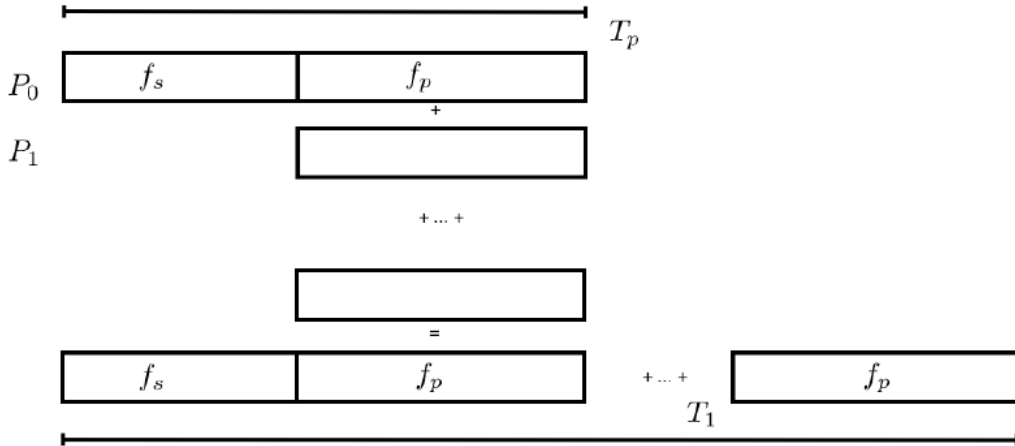


Figure 7.5 Graphic of Gustafson parallel coding pattern. f_s is the fraction of a program, in time, spent on serial computation. f_p is the fraction of computing time that is parallelizable. T_p is the total time for a parallel program to run. T_1 is the total time for a parallel program to run if only 1 processor is allocated. P_N is the N -th processor where it's row is the computation the processor performs. The Gustafson pattern is most similar to what is implemented for this analysis. Figure is pulled from [67].

1241 We need a way to measure and compare the expected speedup and efficiency gain for this
 1242 asynchronous coding pattern. I pull inspiration for timing measurement from [67] and use *Amdahl's
 1243 law with hybrid programming*. Hybrid programming meaning that the computation is a mix of
 1244 distributed and shared memory programming. If we assume the code is fully parallelizable over p
 1245 processors and c threads, the ideal speedup is simply pc and ideal run-time is $T_1/(pc)$. T_1 is the

1246 total time for a parallel program to run if only 1 processor is allocated. However, the coding pattern
1247 contains some amount of unavoidable serial computation, as shown in Figure 7.5. In our case, the
1248 run time is estimated to be

$$T_{p,c} = \frac{T_1}{pc} (1 + F_s(c - 1)). \quad (7.4)$$

1249 F_s is the fraction of CPU time dedicated to serial computation. The expected speedup is

$$S_{p,c} \equiv \frac{T_1}{T_{p,c}} = \frac{pc}{1 + F_s(c - 1)}. \quad (7.5)$$

1250 From Equation (7.5), we can see that the speed up scales with p/F_s . We are free to minimize
1251 F_s asymptotically by enlarging the total models that are submitted to the thread pool, thereby
1252 shrinking the CPU fraction dedicated to serial operation. We are also free to define exactly how
1253 many threads and processors we utilize, yet eventually hit a hard cap at the hardware available on
1254 our computing cluster. HAWC uses Intel Xeon processors with 48 cores and 96 threads. This
1255 means when N-threads (c) are defined, $N \bmod 2$ cores (p) are needed. We see that a successful
1256 code scales well as the expected speedup is inversely correlated with F_s . As the total number of
1257 models sampled grows, the speedup will also.

1258 7.5.2 Implementation

1259 The multithreaded code was written in Python3 and is documented in the `dark_matter_hawc`
1260 `repository` within the script named `mpu_analysis.py`. A version of the script as of April 25
1261 **TODO: make sure to update on this date** is also provided in Section B.1 It has many dependancies
1262 including the HAWC analysis software. Figure 7.6 displays the workflow of a job with 3 threads.
1263 Within a job, SOURCE is kept fixed. CHAN(S) remains 17 elements long. More m_χ are sampled
1264 from 11 bins up to 49 (for $\gamma\gamma$ and ZZ) and 25 (for remaining CHANS) which amounts to 12 or 6
1265 mass bins per decade. The DM mass, m_χ , and SM annihilation channels, CHANS, are permuted into
1266 a 473 element list which is split evenly across N threads where N ranges between 5 - 16. Within a
1267 thread, for each m_χ -CHAN tuple, 1001 $\langle\sigma v\rangle$ values are sampled in the likelihood, and the value of
1268 $\langle\sigma v\rangle$ that maximizes the likelihood is found. Although rare, fits that failed are handled on a case
1269 by case basis.

Timing summary for a multi-threaded job.

Import and Load HAL, 3ML, and HAWC analysis software ~ 2 min		
Load HAWC Data ~ 5 min		
Load HAWC PDF's (Detector Resolution files) ~ 4 min		
Load Spatial Model < 1s		
Load Spectra Models <1 s	Load Spectra Models <1 s	Load Spectra Models <1 s
Calculate max LLH (Chan_0, m_{χ_1}) ... max LLH (Chan_?, m_{χ_N}) N = TOTAL/N_THREADS ~ 8 min/Spec_model	Calculate max LLH (Chan_?, m_{χ_1}) ... max LLH (Chan_?, m_{χ_N}) N = TOTAL/N_THREADS ~ 8 min/Spec_model	Calculate max LLH (Chan_?, m_{χ_1}) ... max LLH (Chan_?, m_{χ_N}) N = TOTAL/N_THREADS ~ 8 min/Spec_model
Write results to file <1 s	Write results to file <1 s	Write results to file <1 s
Join Threads and terminate < 1s		

Figure 7.6 Task chart for one multi-threaded job developed for this project. Green blocks indicate a shared resource across the threads AND computation performed serially. Red blocks indicate functional parallel processing within each thread. 3 threads are represented here, yet many more can be employed during the full analysis. Jobs are defined by the SOURCE as these require unique maps to be loaded into the likelihood estimator. The m_{χ} , CHAN, and $\langle \sigma v \rangle$ variables are entered into the thread pool and allocated as evenly as possible across the threads.

1270 7.5.3 Performance

M Tasks	$T_{p,c}$ (hr:min:s)			
	$T_{1,1}$	$T_{1,2}$	$T_{4,8}$	$T_{8,16}$
50	1:40:37.5	0:52:43.7	0:19:13.8	0:13:44.0
74	2:22:30.0	1:15::00.6	0:25:21.3	0:15:49.8
100	(3:07:51.9)			
200	(6:02:20.6)	-		
473	(13:58:40.3)	-		1:09:42.9

Table 7.2 Timing summaries for analyses for serial and multithreaded processes. M tasks is the number of functional-parallel tasks ran for the computation. $T_{p,c}$ is a single run time in hours:minutes:seconds for runs utilizing p cores/processors and c threads. Runs are run interactively on the same computer to maximize consistency. Empty entries are indicated with '-'. (.) entries are estimated entries extrapolated from data earlier in the column.

1271 We see a tremendous reduction to human time waiting for our dSph analyses to run. Table 7.2
 1272 shows the timing summaries for analyses of different sizes and thread counts. Additionally, the
 1273 efficiency gained when consolidating the serial loading of data is also apparent in our ability to

1274 study many more tasks in about the same amount of wall time as a smaller serial computation. Trials
 1275 represented in the table were run on an AMD Opteron® processor 6344 with 48 cores, 2 threads
 1276 per core; 2.6 GHz clock. This is not the same architecture used for analysis on the computing
 1277 cluster however they are similar enough that results shown here are reasonably representative of
 1278 computing on the HAWC computing cluster. I use the Tab. 7.2 for the inferences and conclusions
 1279 in the following paragraphs.

1280 First, we want to find T_s , the time of serial computation. From Fig. 7.5, the timing for our
 1281 coding pattern can be written as

$$T_s + Mt_p = T_{1,1}^M. \quad (7.6)$$

1282 M is the number of functional-parallel tasks (represented as column 1 of Tab. 7.2), and t_p is the
 1283 average time to complete a single parallel task. $T_{1,1}^M$ is the total time for a parallel program to run if
 1284 only 1 processor is allocated for M parallel task. With two runs of different M ($M1$ and $M2$), we
 1285 can use a system of equations to derive

$$T_s = T_{1,1}^{M1} - M1 \left(\frac{T_{1,1}^{M1} - T_{1,1}^{M2}}{M1 - M2} \right). \quad (7.7)$$

1286 We also extract t_p using the same methods:

$$t_p = \frac{T_{1,1}^{M1} - T_{1,1}^{M2}}{M1 - M2}. \quad (7.8)$$

1287 From Tab. 7.2, we set $M1 = 50$ and $M2 = 74$ and take their corresponding $T_{1,1}$ from the table to
 1288 calculate T_s and t_p .

$$T_s = 803.1\text{s} \text{ and } t_p = 104.6\text{s} \quad (7.9)$$

1289 Now, we have specific estimation for the fraction of serial computing time, F_s :

$$F_s = \frac{803.1}{803.1 + 104.6 \cdot M}. \quad (7.10)$$

1290 The maximum M for this study is 473 which evaluates Eq. (7.10): $F_s = 0.016$ or 1.6% of computing
 1291 time. Table 7.3 shows the resulting speedups

M Tasks	$S_{p,c}$		
	$S_{1,2}$	$S_{1,8}$	$T_{1,16}$
50	1.90 [1.76]	5.23 [4.14]	6.35 [5.34]
74	1.90 [1.83]	5.62 [4.82]	9.00 [6.64]
100			
200	-		
473	-		1:09:42.9

Table 7.3 Speed up summaries for analyses for serial and multithreaded processes. M tasks is the number of functional-parallel tasks ran for the computation. $S_{p,c}$ is a single speedup comparison for runs utilizing p cores/processors and c threads. $[\cdot]$ are the estimated speedups calculated from Tab. 7.2, Eq. (7.10), and Eq. (7.5). Empty entries are indicated with '-'. (\cdot) entries are calculated from estimated entries from data in Tab. 7.2.

CHAPTER 8

1292 **HEAVY DARK MATTER ANNIHILATION SEARCH WITH ICECUBE'S NORTH SKY**
1293 **TRACK DATA**

CHAPTER 9

NU DUCK

1294

MULTI-EXPERIMENT SUPPLEMENTARY FIGURES

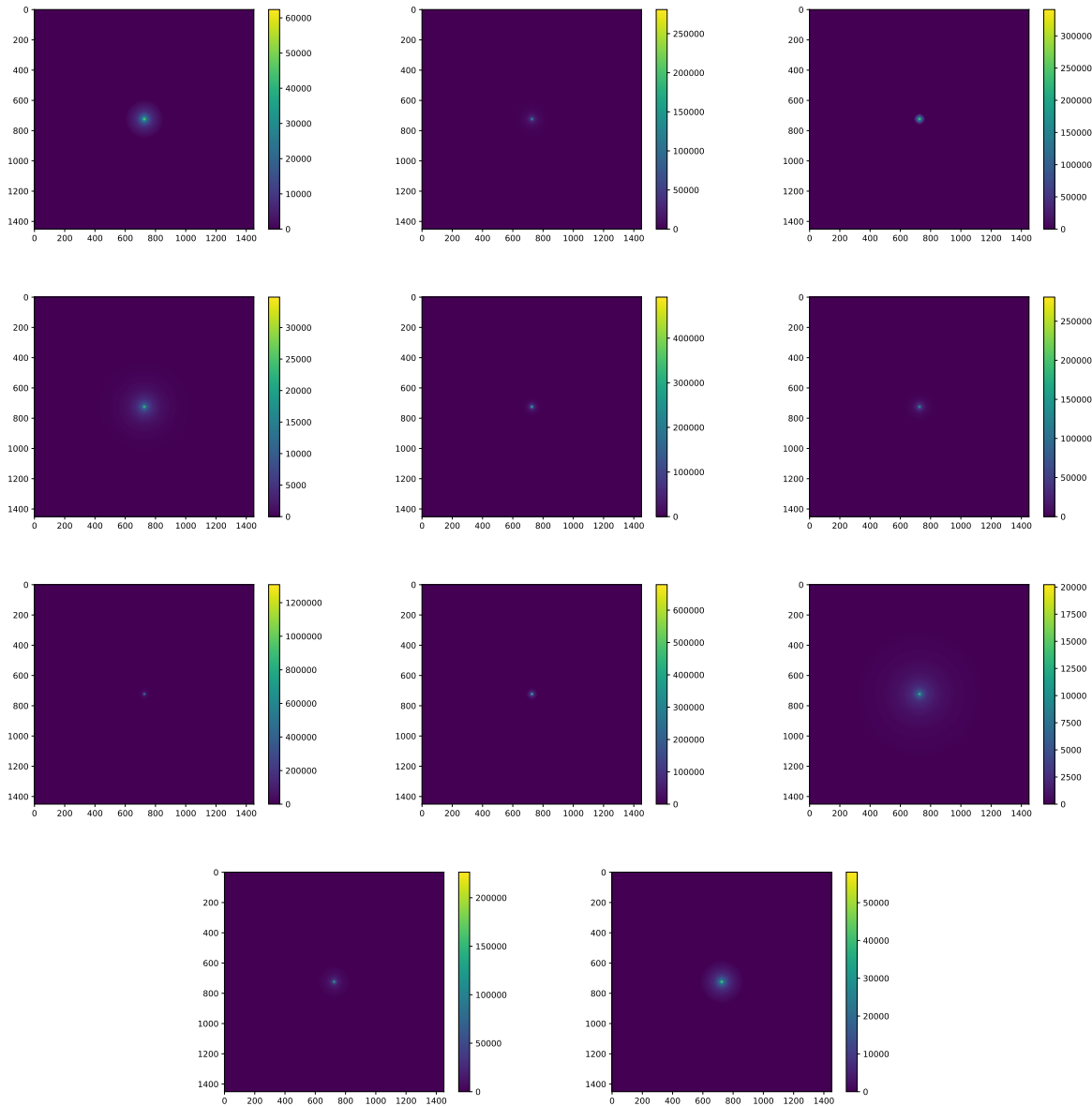


Figure A.1 Sister figure to Figure 6.3. Sources in the first row from left to right: Bootes I, Canes Venatici I, II. In second row: Draco, Hercules, Leo I. In the first row: Leo II, Leo IV, Sextans. In the final row: Ursa Major I, Ursa Major II.

APPENDIX B

MULTITHREADING SUPPLEMENTARY FIGURES

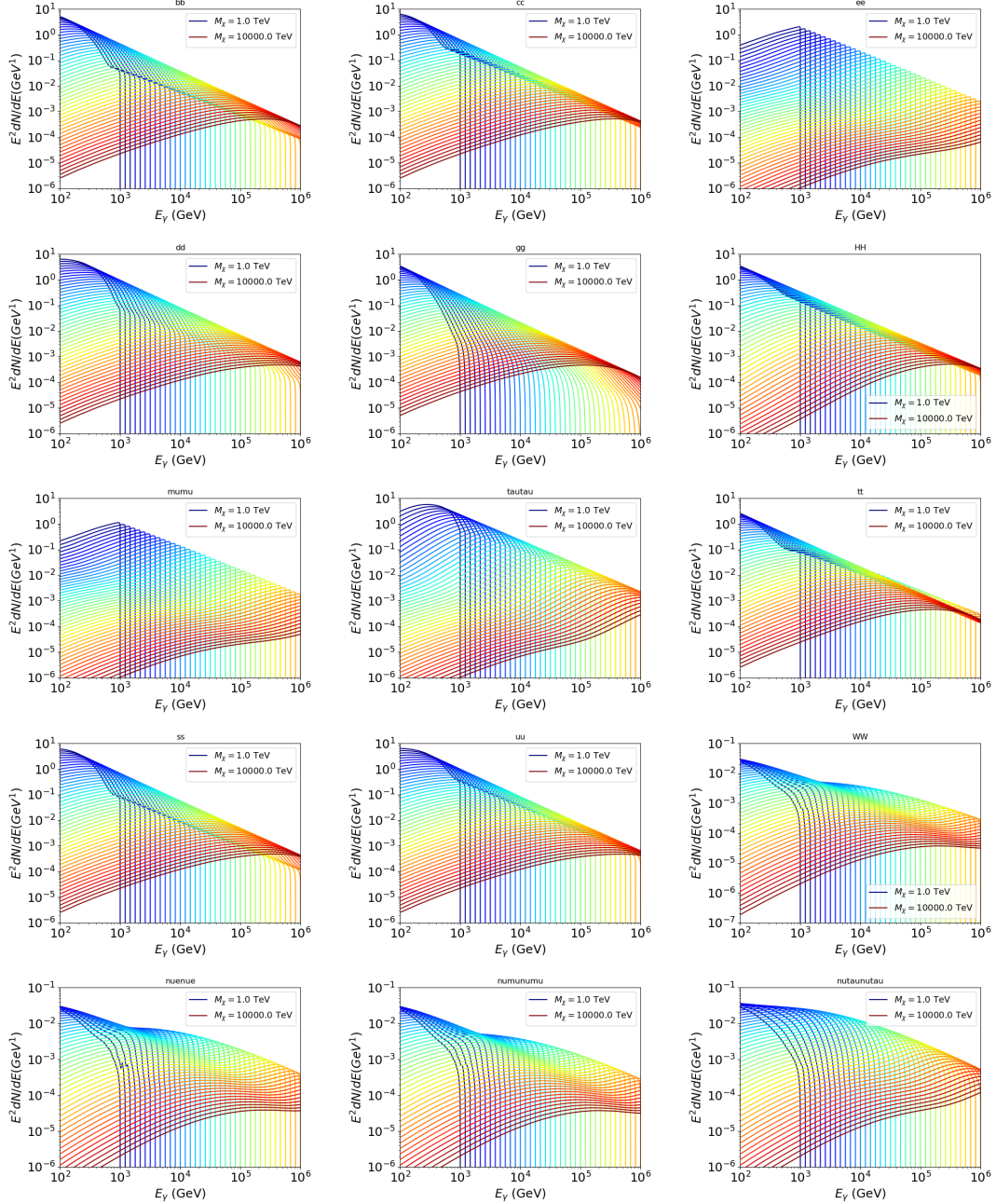


Figure B.1 Sister figure to Figure 7.2 for remaining SM primary annihilation channels studied for this thesis. These did not require any post generation smoothing and so are directly pulled from [64] with a binning scheme most helpful for a HAWC analysis.

1297 B.1 mpu_analysis.py

```
12981 import warnings
12992 with warnings.catch_warnings():
13003     warnings.simplefilter("ignore")
13014 # Python base libraries
13025 import os
13036 import sys
13047 import time
13058 # Import general libraries with namespace
13069 import matplotlib
13070 # Necessary for computing on cluster
13081 matplotlib.use("agg")
13092 import numpy as np
13103 import multiprocessing as mp
13114 # Import HAWC software
13125 sys.path.insert(1, os.path.join(os.environ['HOME'], 'hawc_software', 'threeML-
1313     analysis-scripts', 'fitModel'))
13146 from analysis_modules import *
13157 from threeML import *
13168 from hawc_hal import HAL, HealpixConeROI
13179 from threeML.minimizer.minimization import FitFailed
13180 # Import Dark Matter HAWC Libraries
13191 import analysis_utils as au
13202 import spectra as spec
13213 import sources as srcs
13224
13235 #* READ ONLY PATHS This block will change eventually
13246 MASS_LIST = './plotting/studies/nd/masses.txt'
13257 CHAN_LIST = './plotting/studies/nd/chans.txt'
13268
13279 #* WRITE PATHS, default location is to scratch
13280 OUT_PATH = os.path.join(os.environ["SCRATCH"], os.environ["USER"], 'New_duck')
```

```

13291 print('Our out path is going to be {}'.format(OUT_PATH))
13302
13313 # Define parallel Function. Can also be run serially
13324 def some_mass_fit(sigVs, datalist, shape, dSph, jfactor, mass_chan,
13335                 progress=None, log_file='', queue=None, i_job=0):
13346
13357     if progress is None:
13368         progress = [0]
13379     else: # Create log files for each thread
13380         log_file = log_file.replace('.log', '_ThreadNo_')
13391         log_file = log_file + str(i_job) + ".log"
13402         sys.stdout = open(log_file, "w")
13413
13424     fits = []
13435
13446     try:
13457         for m_c in mass_chan:
13468             print(f'Mass chan tuple: {m_c}')
13479             mass = int(m_c[0])
13480             ch = m_c[1]
13491             # Build path to output files
13502             outPath = os.path.join(OUT_PATH, ch, dSph)
13513             au.ut.ensure_dir(outPath)
13524
13535             if progress[i_job] < 0:
13546                 # If the master gets a Keyboard interrupt, commit suicide.
13557                 break
13568
13579                 ### Start Model Building for DM mass and SM channel #####
13580                 spectrum = spec.DM_models.HDMSpectra()
13591                 spectrum.set_channel(ch)
13602
13613                 myDwarf = ExtendedSource(dSph, spatial_shape=shape,

```

```

13624                     spectral_shape=spectrum)

13635

13646     spectrum.J = jfactor * u.GeV**2 / u.cm**5
13657     spectrum.sigmav = 1e-24 * u.cm**3 / u.s
13668     spectrum.set_dm_mass(mass * u.GeV)

13679

13680     spectrum.sigmav.bounds = (1e-30, 1e-12)
13691     model = Model(myDwarf)
13702     ##### End model Building #####
13713
13724     jl = JointLikelihood(model, datalist, verbose=False)
13735
13746     try:
13757         result, lhdf = jl.fit(compute_covariance=False)
13768         ts = -2.* (jl.minus_log_like_profile(1e-30) - jl.
1377 _current_minimum)
13789         # Also profile the LLH vs sv
13790         ll = jl.get_contours(spectrum.sigmav, sigVs[0],
13801                         sigVs[-1], len(sigVs),
13812                         progress=False, log=['False'])
13823
13834         sigv_ll = au.ut.calc_95_from_profile(ll[0], ll[2])
13845         # Write results to file
13856         outFileLL = outPath+f"/LL_{dSph}_{ch}_mass{int(mass)}_GD.txt"
13867         np.savetxt(outFileLL, (sigVs, ll[2]),
13878                         delimiter='\t', header='sigV\tLL\n')
13889
13890         with open(outPath+f"/results_{dSph}_{ch}_mass{int(mass)}_GD.
1390 txt", "w") as results_file:
13911             results_file.write("mDM [GeV]\tsigV_95\tsigV_B.F.\n")
13922
13933             results_file.write("%i\t%.5E\t%.5E\t%.5E"%(mass, sigv_ll,
13944                                         ts, result.value[0]))

```

```

13955         # End write to file
13956
13957     except FitFailed: # Don't kill all threads if a fit fails
13958         print("Fit failed. Go back and calculate this spectral model
13959             later")
13960
13961         fits.append((ch, mass, -1, -1))
13962
13963     with open(log_file+'.fail', 'w') as f_file:
13964         f_file.write(f'{ch}, {mass}\n')
13965
13966
13967     progress[i_job] += 1
13968
13969     matplotlib.pyplot.close() # Prevent leaky memory
13970
13971
13972     fits.append((ch, mass, result.value[0], ts))
13973
13974     progress[i_job] += 1
13975
13976     matplotlib.pyplot.close()
13977
13978 except KeyboardInterrupt:
13979     progress[i_job] = -1
13980
13981
13982     fits = np.array(fits)
13983
13984     if queue is None:
13985
13986         return fits
13987
13988     else:
13989
13990         queue.put((i_job, fits))
13991
13992
13993 def main(args):
13994
13995     masses = np.loadtxt(MASS_LIST, dtype=int)
13996
13997     chans = np.loadtxt(CHAN_LIST, delimiter=',', dtype=str)
13998
13999     mass_chan = au.ut.permute_lists(chans, masses)
14000
14001
14002     print(f"DM masses for this study are: {masses}")
14003     print(f"SM Channels for this study are XX -> {chans}")
14004     print(mass_chan)
14005
14006
14007     # extract information from input argument

```

```

14287 dSph = args.dSph
14298 data_mngr = au.ut.Data_Selector('P5_NN_2D')
14309 dm_profile = srcts.Spatial_DM(args.catalog, dSph, args.sigma, args.decay)
14310
14321 ##### Extract Source Information #####
14332 if dm_profile.get_dec() < -22.0 or dm_profile.get_dec() > 62.0:
14343     raise ValueError("HAWC can't see this source D: Exitting now...")
14354
14365 print(f'{dSph} information')
14376 print(f'jfac: {dm_profile.get_factor()}\tRA: {dm_profile.get_ra()}\tDec: {dm_profile.get_dec()}\n')
1438
14397
14408 shape = SpatialTemplate_2D(fits_file=dm_profile.get_src_fits())
14419 ##### Finish Extract Source Information #####
14420
14431 ##### LOAD HAWC DATA #####
14442 roi = HealpixConeROI(data_radius=2.0, model_radius=8.0,
14453                         ra=dm_profile.get_ra(), dec=dm_profile.get_dec())
14464 bins = choose_bins.analysis_bins(args, dec=dm_profile.get_dec())
14475
14486 hawc = HAL(dSph, data_mngr.get_datmap(), data_mngr.get_detres(), roi)
14497 hawc.set_active_measurements(bin_list=bins)
14508 datalist = DataList(hawc)
14519 ##### FINISH LOAD HAWC DATA #####
14520
14531 # set up SigV sampling. This sample is somewhat standardized
14542 sigVs = np.logspace(-28,-18, 1001, endpoint=True) # NOTE This will change
1455 with HDM
14563
14574 if args.n_threads == 1:
14585     # No need to start || programming just iterate over the masses
14596     kw_arg = dict(sigVs=sigVs, datalist=datalist, shape=shape, dSph=dSph,
14607                     jfactor=dm_profile.get_factor(), mass_chan=mass_chan,

```

```

14618                 log_file=args.log)
14629             some_mass_fit(**kw_arg)
14630         else:
14641             # I Really want to suppress TQMD output
14652             from tqdm import tqdm
14663             from functools import partialmethod
14674             tqdm.__init__ = partialmethod(tqdm.__init__, disable=True)
14685
14696             x = np.array_split(mass_chan, args.n_threads)
14707             n_jobs = len(x)
14718
14729             print("Thread jobs summary by mass and SM channel")
14730             for xi in x:
14741                 print(f'{xi}')
14752
14763             queue = mp.Queue()
14774             progress = mp.Array('i', np.zeros(n_jobs, dtype=int))
14785
14796             # Define task pool that will be split amongsts threads
14807             kw_args = [dict(sigVs=sigVs, datalist=datalist, shape=shape,
14818                             dSph=dSph, jfactor=dm_profile.get_factor(),
14829                             mass_chan=mass_chan, progress=progress,
14830                             queue=queue, i_job=i, log_file=args.log)
14841                     for i, mass_chan in enumerate(x)]
14852
14863             # Define each process
14874             procs = [mp.Process(target=some_mass_fit, kwargs=kw_args[i]) \
14885                         for i in range(n_jobs)]
14896
14907             ### Start MASTER Thread only code block ###
14918             # Begin running all child threads
14929             for proc in procs: proc.start()
14930

```

```

14941     try:
14952         # In this case, the master does nothing except monitor progress of
1496         # the threads
14973         # In an ideal world, the master thread also does some computation.
14984         n_complete = np.sum(progress)
14995         while_count = 0
15006
15017         while n_complete < len(mass_chan):
15028
15039             if np.any(np.asarray(progress) < 0):
15040                 # This was no threads are stranded when killing the script
15051                 raise KeyboardInterrupt()
15062             if while_count%1000 == 0:
15073                 print(f"{np.sum(progress)} of {len(mass_chan)} finished")
15084
15095             n_complete = np.sum(progress)
15106             time.sleep(.25)
15117             while_count += 1
15128
15139         except KeyboardInterrupt:
15140             # signal to jobs that it's time to stop
15151                 for i in range(n_jobs):
15162                     progress[i] = -2
15173                     print('\nKeyboardInterrupt: terminating early.')
15184             ### End MASTER Thread only code block ###
15195
15206             fitss = [queue.get() for proc in procs]
15217             print(fitss)
15228             print(f'Thread statuses: {progress[:]}')
15239
15240             # putting results in a file
15251
15262             print("QUACK! All Done!")

```

```

15273
15284
15295 if __name__ == '__main__':
15306     import argparse
15317
15328     p = argparse.ArgumentParser(description="Run a DM annihilation analysis on
1533         a dwarf spheroidal for a specific SM channel for DM masses [1 TeV to 10
1534         PeV]")
15359
15360     # Dwarf spatial modeling arguements
15371     p.add_argument("-ds", "--dSph", type=str,
15382             help="dwarf spheroidal galaxy to be studied", required=
1539 True)
15403     p.add_argument("-cat", "--catalog", type=str, choices=['GS15', 'LS20'],
1541             default='LS20', help="source catalog used")
15425     p.add_argument("-sig", "--sigma", type=int, choices=[-1, 0, 1], default=0,
15436             help="Spatial model uncertainty. 0 corresponds to the
1544 median. +/-1 correspond to the +/-1sigma uncertainty respectively.")
15457
15468     # Arguements for the energy estimators
15479     p.add_argument("-e", "--estimator", type=str,
15480             choices=['P5_NHIT', 'P5_NN_2D'],
15491             default="P5_NN_2D", required=False,
15502             help="The energy estimator choice. Options are: P5_NHIT,
1551 P5_NN_2D. GP not supported (yet).")
15523     p.add_argument("--use-bins", default=None, nargs="*",
15534             help="Bins to use for the analysis", dest="use_bins")
15545     p.add_argument('--select_bins_by_energy', default=None, nargs="*",
15556             help="Does nothing. May fill in later once better
1556 understood")
15577     p.add_argument('--select_bins_by_fhit', default=None, nargs="*",
15588             help="Also does nothing see above")
15599     p.add_argument( '-ex', "--exclude", default=None, nargs="*",

```

```

15600         help="Exclude Bins", dest="exclude")

1561

15622 # Computing and logging arguements.

15633 p.add_argument('-nt', '--n_threads', type=int, default=1,
15644                         help='Maximum number of threads spawned by script. Default
1565      is 4')

15665 p.add_argument('-log', '--log', type=str, required=True,
15676                         help='Name for log files. Especially needed for threads')

15687

15698 p.add_argument('--decay', action="store_true",
15709                         help='Set spectral DM hypothesis to decay')

15710

15721 args = p.parse_args()

15732 print(args.decay)

15743 if args.exclude is None: # default exclude bins 0 and 1
15754     args.exclude = ['B0C0Ea', 'B0C0Eb', 'B0C0Ec', 'B0C0Ed', 'B0C0Ee']

15765

15776 if args.decay: OUT_PATH += '_dec'
15787 else: OUT_PATH += '_ann'

15798

15809 OUT_PATH = OUT_PATH + '_' + args.catalog
15810 if args.sigma != 0: OUT_PATH += f'_{args.sigma}sig'

15821

15832 main(args)

```

BIBLIOGRAPHY

- 1585 [1] Anne M. Green. “Dark matter in astrophysics/cosmology”. In: *SciPost Phys. Lect.*
 1586 *Notes* (2022), p. 37. doi: [10.21468/SciPostPhysLectNotes.37](https://doi.org/10.21468/SciPostPhysLectNotes.37). URL: <https://scipost.org/10.21468/SciPostPhysLectNotes.37>.
- 1588 [2] Bing-Lin Young. “A survey of dark matter and related topics in cosmology”. In: *Frontiers*
 1589 *of Physics* 12 (Oct. 2016). doi: <https://doi.org/10.1007/s11467-016-0583-4>.
 1590 URL: <https://doi.org/10.1007/s11467-016-0583-4>.
- 1591 [3] Gianfranco Bertone, Dan Hooper, and Joseph Silk. “Particle dark matter: evidence,
 1592 candidates and constraints”. In: *Physics Reports* 405.5 (2005), pp. 279–390. ISSN:
 1593 0370-1573. doi: <https://doi.org/10.1016/j.physrep.2004.08.031>. URL:
 1594 <https://www.sciencedirect.com/science/article/pii/S0370157304003515>.
- 1595 [4] Gianfranco Bertone and Dan Hooper. “History of dark matter”. In: *Rev. Mod. Phys.*
 1596 90 (4 Aug. 2018), p. 045002. doi: [10.1103/RevModPhys.90.045002](https://doi.org/10.1103/RevModPhys.90.045002). URL: <https://link.aps.org/doi/10.1103/RevModPhys.90.045002>.
- 1598 [5] Fritz Zwicky. “The Redshift of Extragalactic Nebulae”. In: *Helvetica Physica Acta* 6.
 1599 (1933), pp. 110–127. doi: [10.5169/seals-110267](https://doi.org/10.5169/seals-110267).
- 1600 [6] Vera C. Rubin and Jr. Ford W. Kent. “Rotation of the Andromeda Nebula from a
 1601 Spectroscopic Survey of Emission Regions”. In: *ApJ* 159 (Feb. 1970), p. 379. doi:
 1602 [10.1086/150317](https://doi.org/10.1086/150317).
- 1603 [7] K. G. Begeman, A. H. Broeils, and R. H. Sanders. “Extended rotation curves of spiral galax-
 1604 ies: dark haloes and modified dynamics”. In: *Monthly Notices of the Royal Astronomical So-*
 1605 *ciety* 249.3 (Apr. 1991), pp. 523–537. ISSN: 0035-8711. doi: [10.1093/mnras/249.3.523](https://doi.org/10.1093/mnras/249.3.523).
 1606 eprint: <https://academic.oup.com/mnras/article-pdf/249/3/523/18160929/mnras249-0523.pdf>. URL: <https://doi.org/10.1093/mnras/249.3.523>.
- 1608 [8] *Different types of gravitational lenses*. website. Feb. 2004. URL: <https://esahubble.org/images/heic0404b/>.
- 1610 [9] Douglas Clowe et al. “A Direct Empirical Proof of the Existence of Dark Matter”. In: *apjl*
 1611 648.2 (Sept. 2006), pp. L109–L113. doi: [10.1086/508162](https://doi.org/10.1086/508162). arXiv: [astro-ph/0608407](https://arxiv.org/abs/astro-ph/0608407)
 1612 [[astro-ph](https://arxiv.org/abs/astro-ph/0608407)].
- 1613 [10] Planck Collaboration and N. et. al. Aghanim. “Planck 2018 results I. Overview and the
 1614 cosmological legacy of Planck”. In: *A&A* 641 (2020). doi: [10.1051/0004-6361/201833880](https://doi.org/10.1051/0004-6361/201833880). URL: <https://doi.org/10.1051/0004-6361/201833880>.
- 1616 [11] Wayne Hu. *Matter Density Animation*. web. 2024. URL: <http://background.uchicago.edu/~whu/animbut/anim2.html>.

- 1618 [12] Wenlong Yuan et al. “A First Look at Cepheids in a Type Ia Supernova Host with JWST”. in:
1619 *The Astrophysical Journal Letters* 940.1 (Nov. 2022). doi: [10.3847/2041-8213/ac9b27](https://doi.org/10.3847/2041-8213/ac9b27).
1620 URL: <https://dx.doi.org/10.3847/2041-8213/ac9b27>.
- 1621 [13] Wendy L. Freedman. “Measurements of the Hubble Constant: Tensions in Perspective”. In:
1622 *The Astrophysical Journal* 919.1 (Sept. 2021), p. 16. doi: [10.3847/1538-4357/ac0e95](https://doi.org/10.3847/1538-4357/ac0e95).
1623 URL: <https://dx.doi.org/10.3847/1538-4357/ac0e95>.
- 1624 [14] Jodi Cooley. “Dark Matter direct detection of classical WIMPs”. In: *SciPost Phys. Lect.
1625 Notes* (2022), p. 55. doi: [10.21468/SciPostPhysLectNotes.55](https://doi.org/10.21468/SciPostPhysLectNotes.55). URL: <https://scipost.org/10.21468/SciPostPhysLectNotes.55>.
- 1627 [15] “Search for new phenomena in events with an energetic jet and missing transverse momentum
1628 in pp collisions at $\sqrt{s} = 13$ TeV with the ATLAS detector”. In: *Phys. Rev. D* 103
1629 (11 July 2021), p. 112006. doi: [10.1103/PhysRevD.103.112006](https://doi.org/10.1103/PhysRevD.103.112006). URL: <https://link.aps.org/doi/10.1103/PhysRevD.103.112006>.
- 1631 [16] *Jetting into the dark side: a precision search for dark matter*. website. July 2020. URL:
1632 <https://atlas.cern/updates/briefing/precision-search-dark-matter>.
- 1633 [17] Celine Armand et. al. “Combined dark matter searches towards dwarf spheroidal galaxies
1634 with Fermi-LAT, HAWC, H.E.S.S., MAGIC, and VERITAS”. in: *Proceedings of Science*.
1635 Vol. 395. Mar. 2022. doi: <https://doi.org/10.22323/1.395.0528>.
- 1636 [18] Tracy R. Slatyer. “Les Houches Lectures on Indirect Detection of Dark Matter”. In: *SciPost
1637 Phys. Lect. Notes* (2022), p. 53. doi: [10.21468/SciPostPhysLectNotes.53](https://doi.org/10.21468/SciPostPhysLectNotes.53). URL:
1638 <https://scipost.org/10.21468/SciPostPhysLectNotes.53>.
- 1639 [19] Christian W Bauer, Nicholas L. Rodd, and Bryan R. Webber. “Dark matter spectra from
1640 the electroweak to the Planck scale”. In: *Journal of High Energy Physics* 2021.1029-8479
1641 (June 2021). doi: [https://doi.org/10.1007/JHEP06\(2021\)121](https://doi.org/10.1007/JHEP06(2021)121).
- 1642 [20] Riccardo Catena and Piero Ullio. “A novel determination of the local dark matter density”.
1643 In: *Journal of Cosmology and Astroparticle Physics* 2010.08 (Aug. 2010), p. 004. doi:
1644 [10.1088/1475-7516/2010/08/004](https://doi.org/10.1088/1475-7516/2010/08/004). URL: <https://dx.doi.org/10.1088/1475-7516/2010/08/004>.
- 1646 [21] B. P. Abbott et al. “Observation of Gravitational Waves from a Binary Black Hole Merger”.
1647 In: *Phys. Rev. Lett.* 116 (6 Feb. 2016), p. 061102. doi: [10.1103/PhysRevLett.116.061102](https://doi.org/10.1103/PhysRevLett.116.061102). URL: <https://link.aps.org/doi/10.1103/PhysRevLett.116.061102>.
- 1649 [22] R. Abbasi et. al. “Observation of high-energy neutrinos from the Galactic plane”. In: *Science*
1650 380.6652 (June 2023), pp. 1338–1343.
- 1651 [23] NASA Goddard Space Flight Center. *Fermi’s 12-year view of the gamma-ray sky*. website.

- 1652 2022. URL: <https://svs.gsfc.nasa.gov/14090>.
- 1653 [24] Marco Cirelli et al. “PPPC 4 DM ID: a poor particle physicist cookbook for dark matter
1654 indirect detection”. In: *Journal of Cosmology and Astroparticle Physics* 2011.03 (Mar.
1655 2011), p. 051. doi: [10.1088/1475-7516/2011/03/051](https://doi.org/10.1088/1475-7516/2011/03/051). URL: <https://dx.doi.org/10.1088/1475-7516/2011/03/051>.
- 1657 [25] Javier Rico. “Gamma-Ray Dark Matter Searches in Milky Way Satellites—A Comparative
1658 Review of Data Analysis Methods and Current Results”. In: *Galaxies* 8.1 (Mar. 2020), p. 25.
1659 doi: [10.3390/galaxies8010025](https://doi.org/10.3390/galaxies8010025). arXiv: [2003.13482](https://arxiv.org/abs/2003.13482) [astro-ph.HE].
- 1660 [26] W. B. Atwood et al. “The Large Area Telescope on the Fermi Gamma-Ray Space Telescope
1661 Mission”. In: *apj* 697.2 (June 2009), pp. 1071–1102. doi: [10.1088/0004-637X/697/2/1071](https://doi.org/10.1088/0004-637X/697/2/1071). arXiv: [0902.1089](https://arxiv.org/abs/0902.1089) [astro-ph.IM].
- 1663 [27] M. Ackermann et al. “Searching for Dark Matter Annihilation from Milky Way Dwarf
1664 Spheroidal Galaxies with Six Years of Fermi Large Area Telescope Data”. In: *prl* 115.23,
1665 231301 (Dec. 2015), p. 231301. doi: [10.1103/PhysRevLett.115.231301](https://doi.org/10.1103/PhysRevLett.115.231301). arXiv:
1666 [1503.02641](https://arxiv.org/abs/1503.02641) [astro-ph.HE].
- 1667 [28] Mattia Di Mauro, Martin Stref, and Francesca Calore. “Investigating the effect of Milky
1668 Way dwarf spheroidal galaxies extension on dark matter searches with Fermi-LAT data”.
1669 In: *Phys. Rev. D* 106 (12 Dec. 2022), p. 123032. doi: [10.1103/PhysRevD.106.123032](https://doi.org/10.1103/PhysRevD.106.123032).
1670 URL: <https://link.aps.org/doi/10.1103/PhysRevD.106.123032>.
- 1671 [29] F. et al. Aharonian. “Observations of the Crab Nebula with H.E.S.S.”. In: *Astron. Astrophys.*
1672 457 (2006), pp. 899–915. doi: [10.1051/0004-6361:20065351](https://doi.org/10.1051/0004-6361:20065351). arXiv: [astro-ph/0607333](https://arxiv.org/abs/astro-ph/0607333).
- 1674 [30] J. Albert et al. “VHE γ -Ray Observation of the Crab Nebula and its Pulsar with the MAGIC
1675 Telescope”. In: *The Astrophysical Journal* 674.2 (Feb. 2008), p. 1037. doi: [10.1086/525270](https://doi.org/10.1086/525270). URL: <https://dx.doi.org/10.1086/525270>.
- 1677 [31] N. Park. “Performance of the VERITAS experiment”. In: *Proceedings, 34th International
1678 Cosmic Ray Conference (ICRC2015): The Hague, The Netherlands, July, 30th July - 6th
1679 August*. Vol. 34. 2015, p. 771. arXiv: [1508.07070](https://arxiv.org/abs/1508.07070) [astro-ph.IM].
- 1680 [32] A. Abramowski et al. “H.E.S.S. constraints on Dark Matter annihilations towards the Sculptor
1681 and Carina Dwarf Galaxies”. In: *Astropart. Phys.* 34 (2011), pp. 608–616. doi: [10.1016/j.astropartphys.2010.12.006](https://doi.org/10.1016/j.astropartphys.2010.12.006). arXiv: [1012.5602](https://arxiv.org/abs/1012.5602) [astro-ph.HE].
- 1683 [33] A. Abramowski et al. “Search for dark matter annihilation signatures in H.E.S.S. observations
1684 of Dwarf Spheroidal Galaxies”. In: *Phys. Rev. D* 90 (2014), p. 112012. doi: [10.1103/PhysRevD.90.112012](https://doi.org/10.1103/PhysRevD.90.112012). arXiv: [1410.2589](https://arxiv.org/abs/1410.2589) [astro-ph.HE].

- 1686 [34] H. Abdalla et al. “Searches for gamma-ray lines and ‘pure WIMP’ spectra from Dark
1687 Matter annihilations in dwarf galaxies with H.E.S.S”. in: *JCAP* 11 (2018), p. 037. doi:
1688 [10.1088/1475-7516/2018/11/037](https://doi.org/10.1088/1475-7516/2018/11/037). arXiv: [1810.00995 \[astro-ph.HE\]](https://arxiv.org/abs/1810.00995).
- 1689 [35] J. Aleksić et al. “Optimized dark matter searches in deep observations of Segue 1 with
1690 MAGIC”. in: *JCAP* 1402 (2014), p. 008. doi: [10.1088/1475-7516/2014/02/008](https://doi.org/10.1088/1475-7516/2014/02/008).
1691 arXiv: [1312.1535 \[hep-ph\]](https://arxiv.org/abs/1312.1535).
- 1692 [36] V.A. Acciari et al. “Combined searches for dark matter in dwarf spheroidal galaxies observed
1693 with the MAGIC telescopes, including new data from Coma Berenices and Draco”. In: *Physics of the Dark Universe* (2021), p. 100912. issn: 2212-6864. doi: <https://doi.org/10.1016/j.dark.2021.100912>. URL: <https://www.sciencedirect.com/science/article/pii/S2212686421001370>.
- 1697 [37] M. L. Ahnen et al. “Indirect dark matter searches in the dwarf satellite galaxy Ursa Major II
1698 with the MAGIC Telescopes”. In: *JCAP* 1803.03 (2018), p. 009. doi: [10.1088/1475-7516/2018/03/009](https://doi.org/10.1088/1475-7516/2018/03/009). arXiv: [1712.03095 \[astro-ph.HE\]](https://arxiv.org/abs/1712.03095).
- 1700 [38] S. et al. Archambault. “Dark matter constraints from a joint analysis of dwarf Spheroidal
1701 galaxy observations with VERITAS”. in: *prd* 95.8 (Apr. 2017). doi: [10.1103/PhysRevD.95.082001](https://doi.org/10.1103/PhysRevD.95.082001). arXiv: [1703.04937 \[astro-ph.HE\]](https://arxiv.org/abs/1703.04937).
- 1703 [39] Louise Oakes et al. “Combined Dark Matter searches towards dwarf spheroidal galaxies with
1704 Fermi-LAT, HAWC, HESS, MAGIC and VERITAS”. in: *Proceedings of Science*. 2019.
- 1705 [40] Celine Armand et al. on behalf of the Fermi-LAT, HAWC, HESS, MAGIC, VERITAS.
1706 “Combined Dark Matter searches towards dwarf spheroidal galaxies with Fermi-LAT,
1707 HAWC, HESS, MAGIC and VERITAS”. in: *Proceedings of Science*. 2021.
- 1708 [41] Daniel Kerszberg et al. on behalf of the Fermi-LAT, HAWC, HESS, MAGIC, and VER-
1709 TIAS collaborations. “Search for dark matter annihilation with a combined analysis of
1710 dwarf spheroidal galaxies from Fermi-LAT, HAWC, H.E.S.S., MAGIC and VERITAS”. in:
1711 *Proceedings of Science*. 2023.
- 1712 [42] A. U. Abeysekara et al. “Observation of the Crab Nebula with the HAWC Gamma-Ray
1713 Observatory”. In: *The Astrophysical Journal* 843.1 (June 2017), p. 39. doi: [10.3847/1538-4357/aa7555](https://doi.org/10.3847/1538-4357/aa7555). URL: <https://doi.org/10.3847/1538-4357/aa7555>.
- 1715 [43] Giacomo Vianello et al. *The Multi-Mission Maximum Likelihood framework (3ML)*. 2015.
1716 arXiv: [1507.08343 \[astro-ph.HE\]](https://arxiv.org/abs/1507.08343).
- 1717 [44] Marco Cirelli et al. “PPPC 4 DM ID: a poor particle physicist cookbook for dark matter
1718 indirect detection”. In: *Journal of Cosmology and Astroparticle Physics* 2011.03 (Mar.
1719 2011). issn: 1475-7516. doi: [10.1088/1475-7516/2011/03/051](https://doi.org/10.1088/1475-7516/2011/03/051). URL: <http://dx.doi.org/10.1088/1475-7516/2011/03/051>.

- 1721 [45] Alex Geringer-Sameth, Savvas M. Koushiappas, and Matthew Walker. “DWARF GALAXY
1722 ANNIHILATION AND DECAY EMISSION PROFILES FOR DARK MATTER EXPERI-
1723 MENTS”. in: *The Astrophysical Journal* 801.2 (Mar. 2015), p. 74. ISSN: 1538-4357. doi:
1724 [10.1088/0004-637X/801/2/74](https://doi.org/10.1088/0004-637X/801/2/74). URL: <http://dx.doi.org/10.1088/0004-637X/801/2/74>.
- 1726 [46] A. Albert et al. “Dark Matter Limits from Dwarf Spheroidal Galaxies with the HAWC
1727 Gamma-Ray Observatory”. In: *The Astrophysical Journal* 853.2 (Feb. 2018), p. 154. ISSN:
1728 1538-4357. doi: [10.3847/1538-4357/aaa6d8](https://doi.org/10.3847/1538-4357/aaa6d8). URL: <http://dx.doi.org/10.3847/1538-4357/aaa6d8>.
- 1730 [47] V. Bonnivard et al. “Spherical Jeans analysis for dark matter indirect detection in dwarf
1731 spheroidal galaxies - Impact of physical parameters and triaxiality”. In: *Mon. Not. Roy.
1732 Astron. Soc.* 446 (2015), pp. 3002–3021. doi: [10.1093/mnras/stu2296](https://doi.org/10.1093/mnras/stu2296). arXiv:
1733 [1407.7822 \[astro-ph.HE\]](https://arxiv.org/abs/1407.7822).
- 1734 [48] M. Ackermann et al. “Searching for Dark Matter Annihilation from Milky Way Dwarf
1735 Spheroidal Galaxies with Six Years of Fermi Large Area Telescope Data”. In: *prl* 115.23,
1736 231301 (Dec. 2015), p. 231301. doi: [10.1103/PhysRevLett.115.231301](https://doi.org/10.1103/PhysRevLett.115.231301). arXiv:
1737 [1503.02641 \[astro-ph.HE\]](https://arxiv.org/abs/1503.02641).
- 1738 [49] M. L. Ahnen et al. “Limits to Dark Matter Annihilation Cross-Section from a Combined
1739 Analysis of MAGIC and Fermi-LAT Observations of Dwarf Satellite Galaxies”. In: *JCAP*
1740 1602.02 (2016), p. 039. doi: [10.1088/1475-7516/2016/02/039](https://doi.org/10.1088/1475-7516/2016/02/039). arXiv: [1601.06590](https://arxiv.org/abs/1601.06590)
1741 [astro-ph.HE].
- 1742 [50] Javier Rico et al. *gLike: numerical maximization of heterogeneous joint
1743 likelihood functions of a common free parameter plus nuisance parameters*.
1744 <https://doi.org/10.5281/zenodo.4601451>. Version v0.09.03. Mar. 2021. doi: [10.5281/zenodo.4601451](https://doi.org/10.5281/zenodo.4601451). URL: <https://doi.org/10.5281/zenodo.4601451>.
- 1746 [51] Tjark Miener and Daniel Nieto. *LklCom: Combining likelihoods from different experiments*.
1747 <https://doi.org/10.5281/zenodo.4597500>. Version v0.5.3. Mar. 2021. doi: [10.5281/zenodo.4597500](https://doi.org/10.5281/zenodo.4597500). URL: <https://doi.org/10.5281/zenodo.4597500>.
- 1749 [52] T. Miener et al. “Open-source Analysis Tools for Multi-instrument Dark Matter Searches”.
1750 In: *arXiv e-prints*, arXiv:2112.01818 (Dec. 2021), arXiv:2112.01818. arXiv: [2112.01818](https://arxiv.org/abs/2112.01818)
1751 [astro-ph.IM].
- 1752 [53] Alex Geringer-Sameth and Matthew Koushiappas Savvas M. and Walker. “Dwarf galaxy
1753 annihilation and decay emission profiles for dark matter experiments”. In: *Astrophys.
1754 J.* 801.2 (2015), p. 74. doi: [10.1088/0004-637X/801/2/74](https://doi.org/10.1088/0004-637X/801/2/74). arXiv: [1408.0002](https://arxiv.org/abs/1408.0002)
1755 [astro-ph.CO].
- 1756 [54] Gianfranco Bertone, Dan Hooper, and Joseph Silk. “Particle dark matter: evidence, can-

- 1757 didates and constraints”. In: *Physics Reports* 405.5-6 (Jan. 2005), pp. 279–390. ISSN:
1758 0370-1573. doi: [10.1016/j.physrep.2004.08.031](https://doi.org/10.1016/j.physrep.2004.08.031). URL: <http://dx.doi.org/10.1016/j.physrep.2004.08.031>.
- 1760 [55] V. Bonnivard et al. “Dark matter annihilation and decay in dwarf spheroidal galaxies: The
1761 classical and ultrafaint dSphs”. In: *Mon. Not. Roy. Astron. Soc.* 453.1 (2015), pp. 849–867.
1762 doi: [10.1093/mnras/stv1601](https://doi.org/10.1093/mnras/stv1601). arXiv: [1504.02048 \[astro-ph.HE\]](https://arxiv.org/abs/1504.02048).
- 1763 [56] A. et al. Albert. “Searching for Dark Matter Annihilation in Recently Discovered Milky Way
1764 Satellites with Fermi-LAT”. in: *Astrophys. J.* 834.2 (2017), p. 110. doi: [10.3847/1538-4357/834/2/110](https://doi.org/10.3847/1538-4357/834/2/110). arXiv: [1611.03184 \[astro-ph.HE\]](https://arxiv.org/abs/1611.03184).
- 1766 [57] Mattia Di Mauro and Martin Wolfgang Winkler. “Multimessenger constraints on the dark
1767 matter interpretation of the Fermi-LAT Galactic Center excess”. In: *prd* 103.12, 123005
1768 (June 2021), p. 123005. doi: [10.1103/PhysRevD.103.123005](https://doi.org/10.1103/PhysRevD.103.123005). arXiv: [2101.11027 \[astro-ph.HE\]](https://arxiv.org/abs/2101.11027).
- 1770 [58] HongSheng Zhao. “Analytical models for galactic nuclei”. In: *Mon. Not. Roy. Astron. Soc.*
1771 278 (1996), pp. 488–496. doi: [10.1093/mnras/278.2.488](https://doi.org/10.1093/mnras/278.2.488). arXiv: [astro-ph/9509122 \[astro-ph\]](https://arxiv.org/abs/astro-ph/9509122).
- 1773 [59] H. C. Plummer. “On the Problem of Distribution in Globular Star Clusters: (Plate 8.)”
1774 In: *Monthly Notices of the Royal Astronomical Society* 71.5 (Mar. 1911), pp. 460–470.
1775 ISSN: 0035-8711. doi: [10.1093/mnras/71.5.460](https://doi.org/10.1093/mnras/71.5.460). eprint: <https://academic.oup.com/mnras/article-pdf/71/5/460/2937497/mnras71-0460.pdf>. URL:
1777 <https://doi.org/10.1093/mnras/71.5.460>.
- 1778 [60] Daniel R. Hunter. “Derivation of the anisotropy profile, constraints on the local velocity
1779 dispersion, and implications for direct detection”. In: *JCAP* 02 (2014), p. 023. doi:
1780 [10.1088/1475-7516/2014/02/023](https://doi.org/10.1088/1475-7516/2014/02/023). arXiv: [1311.0256 \[astro-ph.CO\]](https://arxiv.org/abs/1311.0256).
- 1781 [61] Barun Kumar Dhar and Liliya L. R. Williams. “Surface mass density of the Einasto family
1782 of dark matter haloes: are they Sersic-like?” In: *Mon. Not. Roy. Astron. Soc.* (2010). doi:
1783 [10.1111/j.1365-2966.2010.16446.x](https://doi.org/10.1111/j.1365-2966.2010.16446.x).
- 1784 [62] M. Baes and E. Van Hese. “Dynamical models with a general anisotropy profile”. In:
1785 *Astron. Astrophys.* 471 (2007), p. 419. doi: [10.1051/0004-6361:20077672](https://doi.org/10.1051/0004-6361:20077672). arXiv:
1786 [0705.4109 \[astro-ph\]](https://arxiv.org/abs/0705.4109).
- 1787 [63] Matthew G. Walker, Edward W. Olszewski, and Mario Mateo. “Bayesian analysis of re-
1788 solved stellar spectra: application to MMT/Hectochelle observations of the Draco dwarf
1789 spheroidal”. In: *mnras* 448.3 (Apr. 2015), pp. 2717–2732. doi: [10.1093/mnras/stv099](https://doi.org/10.1093/mnras/stv099).
1790 arXiv: [1503.02589 \[astro-ph.GA\]](https://arxiv.org/abs/1503.02589).
- 1791 [64] Nicholas L. Rodd et al. “Dark matter spectra from the electroweak to the Planck scale”. In:

- 1792 *J. High Energy Physics* 121.10.1007 (June 2021).
- 1793 [65] Pace, Andrew B and Strigari, Louis E. “Scaling relations for dark matter annihilation and
1794 decay profiles in dwarf spheroidal galaxies”. In: *Monthly Notices of the Royal Astronomical
1795 Society* 482.3 (Oct. 2018), pp. 3480–3496. ISSN: 0035-8711. doi: [10.1093/mnras/sty2839](https://doi.org/10.1093/mnras/sty2839).
- 1797 [66] Albert, A. et al. “Search for gamma-ray spectral lines from dark matter annihilation in
1798 dwarf galaxies with the High-Altitude Water Cherenkov observatory”. In: *Phys. Rev. D* 101 (10 May 2020), p. 103001. doi: [10.1103/PhysRevD.101.103001](https://doi.org/10.1103/PhysRevD.101.103001). URL:
1799 <https://link.aps.org/doi/10.1103/PhysRevD.101.103001>.
- 1800
- 1801 [67] Victor Eijkhout and Edmund Show and Robert van de Geijn. *The Science of Computing.
1802 The Art of High Performance Computing*. Vol. 3. Open Copy published under CC-BY 4.0
1803 license, 2023, pp. 63–66.